Nonlinear disturbance evolution in boundary layers using the one-way Navier-Stokes equations

Thesis by
Michael Kenneth Elliott Sleeman

In Partial Fulfillment of the Requirements for the
Degree of
Doctor of Philosophy in Mechanical Engineering

CALIFORNIA INSTITUTE OF TECHNOLOGY
Pasadena, California

2026
Defended August 1, 2025

Michael Kenneth Elliott Sleeman
ORCID: 0000-0001-5949-9289

ACKNOWLEDGEMENTS

First and foremost, I would like to thank my advisor Professor Tim Colonius for his thoughtful guidance, feedback, and encouragement throughout my time at Caltech. Professor Colonius is deeply knowledgeable about fluid mechanics and scientific computing, and I appreciate the time and effort he spent deepening my knowledge and understanding of these subject areas.

I would also like to thank my committee members, Professors Guillaume Blanquart, Jane Bae, and Melany Hunt, for their valuable feedback on my thesis.

My academic journey began at the University of British Columbia, where I had the privilege of working in Professor Gwynn Elfring's research group. His courses in fluid mechanics and scientific computing inspired my interest in academic research and his encouragement was critical to the start of my academic journey.

I began my graduate studies in Professor Masayuki Yano's research group at the University of Toronto. I would like to thank Professor Yano for his patient mentorship, and for introducing me to finite element methods, model reduction, and other foundational methods in scientific computing. The skills I developed during my Master's studies were instrumental to my success at Caltech.

During my time at Caltech, I have been fortunate to form lasting friendships with many fellow students who have enriched both my academic and personal life. I am especially grateful to Alex Mori Carroll, with whom I studied fluid mechanics in first year; Ethan Epperly, who deepened my understanding of mathematics and shared many thoughtful research discussions and lunches; Liam Heidt, whose feedback on my research and technical presentations was always insightful; Ethan Eichberger, who has built social connections within the Colonius group and the Mechanical and Civil Engineering department; and Kasper Petersen, who reminded me to enjoy life outside of the academic setting.

I also wish to acknowledge previous researchers who developed and extended the One-Way Navier-Stokes (OWNS) approach and generously shared their expertise and time. This includes Omar Kamal, Aaron Towne, Georgios Rigas, Matthew Lakebrink, and Vishal Anantharaman.

I would like to thank all members, past and present, of the Colonius group, whose camaraderie and collaboration made my time at Caltech all the more rewarding.

I am also thankful for my friendships with Eugene, Sohini, and Nick at the University of Toronto, and with Charles, Sun Jun, and Ben at the University of British Columbia.

Beyond academia, I am deeply grateful to my lifelong friends, including Marcus, Michael, Aaron, Jonathan, Thomas, Chris, Lan, and Kyra, who have known me since high school or earlier. Your continued friendship, whether through shared meals, walks in the park, hikes in the mountains, or bike rides through the city, has brought me joy whenever I have returned home.

I owe immense thanks to my family for their unwavering love and support. I would like to thank my mother for encouraging me to pursue mechanical engineering, both during my undergraduate and graduate studies. Her empathy and emotional support throughout my research journey have been invaluable. I am grateful to my father for cultivating my interest in computing and helping to develop my programming skills. I thank both my parents for instilling in me the values of resilience and a growth mindset, qualities that have shaped my academic and personal life. I am also thankful to my brother, Matthew, whose perspective and strength have taught me many valuable lessons, and whose presence I deeply appreciate. I owe a special thanks to my grandmother, Margaret, and my Uncle Barry, whose curiosity and thoughtful questions about my research and education have always made me feel supported and understood.

Finally, I would like to thank Luna for her steadfast love and support. Your patience, understanding, and unwavering belief in me have been critical to both my success at Caltech and my growth beyond it. I am so grateful to have you in my life, and I am proud that we have supported each other in achieving our goals.

ABSTRACT

Laminar-turbulent transition prediction for boundary-layer flows is a pacing item in engineering design. This work extends the one-way Navier Stokes (OWNS) equations to support nonlinear interactions between waves of different frequencies which enables nonlinear disturbance evolution in spatially-developing shear flows, with the goal of predicting transition for a reduced computational cost relative to direct numerical simulation (DNS). The OWNS approach linearizes the Navier-Stokes equations about a user-specified equilibrium solution, and then evolves disturbances to the equilibrium solution by solving a spatial initial-value problem in the frequency domain. OWNS yields a reduced computational cost compared to global linear stability analysis, while also conferring numerous advantages over the parabolized stability equations (PSE) that we seek to extend to nonlinear OWNS (NOWNS). We validate NOWNS for two- and three-dimensional disturbances to a low-speed Blasius boundary layer by comparing to DNS results from the literature. We further demonstrate that NOWNS can be used to for transition prediction since it accurately predicts the onset of laminar-turbulent transition in low-speed boundary-layer flows, relative to DNS. Subsequently, we extend the approach to high-speed boundary-layer flows, where we apply it to study oblique-wave breakdown of Mack's first and second modes. Finally, we formulate a greedy algorithm for choosing optimal OWNS recursion parameters, which achieves rapid error convergence and a net decrease in computational cost compared to previous approaches to recursion parameter selection.

PUBLISHED CONTENT AND CONTRIBUTIONS

M. Sleeman and T. Colonius. (2025). "Greedy recursion parameter selection for the One-Way Navier–Stokes (OWNS) equations." Submitted in 2025.

M. Sleeman, M. Lakebrink, and T. Colonius. (2025). "Simulation of K-type and H-type Transition Using the Nonlinear One-Way Navier-Stokes Approach." In: *Tenth IUTAM Symposium on Laminar-Turbulent Transition*.

M. Sleeman, M. Lakebrink, and T. Colonius. (2025). "Boundary layer stability analysis using the nonlinear One-Way Navier-Stokes approach". In: *AIAA Journal 2025 63:8, 3145-3159*. DOI: 10.48550/arXiv.2409.17274.

M. Sleeman, M. Lakebrink and T. Colonius. (2024) "The Nonlinear One-Way Navier-Stokes (NOWNS) Approach for Boundary-Layer Transition". In: *AIAA AVIATION 2024 Forum*. DOI: 10.2514/6.2024-3530.

M. Sleeman, M. Lakebrink and T. Colonius. (2023) "Nonlinear stability of wall-bounded flows using the One-Way Navier-Stokes (OWNS) Equations". In: *AIAA AVIATION 2023 Forum*. DOI: 10.2514/6.2023-3273.

The second, fourth, and fifth contributions are conference proceedings: the fifth contribution presents the development and validation of the methodology, while the fourth contribution showcases the advantages of the methodology relative to existing methods. The first contribution is a journal article that develops a greedy algorithm for recursion parameter selection, which must be carefully chosen to ensure the One-Way Navier-Stokes (OWNS) approximation converges. We show that the greedy algorithm achieves faster convergence and yields a reduced computational cost relative to existing recursion parameter selection methods. The second contribution demonstrates that the method can be used to predict laminar-turbulent transition in low-speed boundary-layer flows, while the third contribution is a journal article that combines the fourth and fifth contributions into a single paper.

The first contribution appears in Chapter 2 where it develops criteria for the numerical method to converge, and Chapter 4 where it develops and demonstrates the greedy algorithm. The third, fourth, and fifth contributions appear in Chapter 3 where the numerical method is developed and demonstrate, while the second contribution appears in Chapter 5 where we demonstrate that the method can be used to predict transition in low-speed boundary-layer flows.

TABLE OF CONTENTS

LIST OF ILLUSTRATIONS

LIST OF TABLES

NOMENCLATURE

(x, y, z)	=	streamwise, wall-normal, and spanwise coordinates
v	=	specific volume
(u, v, w)	=	velocity (streamwise, wall-normal, and spanwise)
p	=	pressure
ρ	=	density, where $\rho = 1/v$
T	=	temperature
μ	=	dynamic viscosity
a	=	sound speed
Ma	=	Mach number
c_p	=	specific heat capacity at constant pressure
γ	=	heat capacity ratio
k	=	thermal conductivity
δ_0^*	=	inlet Blasius length scale, defined as $\delta_0^* = \sqrt{\frac{x_0^* \mu_\infty^*}{\rho_\infty^* U_\infty^*}}$
Re	=	Reynolds number in terms of δ_0^*, defined as $Re = \frac{\rho_\infty^* a_\infty^* \delta_0^*}{\mu_\infty^*}$
Pr	=	Prandtl number, defined as $Pr = \frac{\mu^* c_p^*}{k^*}$
ω	=	temporal frequency
F	=	dimensionless temporal frequency, defined as $F = \frac{\omega^* \mu_\infty^*}{\rho_\infty^* U_\infty^{*2}}$
β	=	spanwise wavenumber
b	=	dimensionless spanwise wavenumber, defined as $b = \frac{\beta^* \mu_\infty^*}{\rho_\infty^* U_\infty^*}$
α	=	streamwise wavenumber (complex-valued)
Re_x	=	Reynolds number in terms of x, defined as $Re_x = \frac{\rho_\infty^* U_\infty^* x^*}{\mu_\infty^*}$
M	=	denotes the number of temporal Fourier modes
N	=	denotes the number of spanwise Fourier modes
(m, n)	=	denotes Fourier mode with frequency $m\omega$ and wavenumber $n\beta$
Subscripts		
∞	=	free-stream value
mn	=	a quantity associated with frequency $m\omega$ and wavenumber $n\beta$
$+ - 0$	=	plus, minus, and zero characteristics
Superscripts		
$*$	=	dimensional quantity
$\prime$	=	a disturbance to the equilibrium solution
$\ddagger$	=	a matrix or a vector containing the OWNS auxiliary values

Other symbols

$\bar{(\cdot)}$	=	a quantity associated with the equilibrium solution
$\overline{(\cdot)}$	=	a complex conjugate value
$\hat{(\cdot)}$	=	a quantity in Fourier space

Abbreviations

MFD	=	mean flow distortion
BC	=	boundary condition
PSE	=	Parabolized Stability Equations
NPSE	=	Nonlinear Parabolized Stability Equations
NRBC	=	non-reflecting boundary condition
OWNS	=	One-Way Navier-Stokes
NOWNS	=	Nonlinear One-Way Navier-Stokes
LST	=	Locally-parallel linear stability theory
GSA	=	linear global stability analysis
TS	=	Tollmien-Schlichting, referring to the Tollmien-Schlichting wave
MM	=	referrings to Mack's second mode

Chapter 1

INTRODUCTION

1.1 Boundary-layer flows

In fluid flows, the *boundary layer* is a thin region near a solid surface, such as an airplane wing, where viscous effects dominate.A flow is *laminar* if it flows in parallel layers with no disruption between those layers, while it is *turbulent* if it is characterized by abrupt changes to the flow. In aerospace design, delaying or preventing laminar-turbulent transition is desirable, as turbulence increases skin friction and heating. Despite extensive theoretical, experimental, and numerical studies, controlling transition remains a challenge.

1.2 Governing equations

For low-speed boundary-layer flows, we formulate the governing equations in terms of the specific volume, v, the velocity, $\boldsymbol{u}$, and the pressure, p. Then, the non-dimensional, compressible Navier-Stokes equations for an ideal gas can be written as

$$\frac{Dv}{Dt} - v(\nabla \cdot \boldsymbol{u}) = 0, \tag{1.1a}$$

$$\frac{D\boldsymbol{u}}{Dt} + v\nabla p = \frac{1}{Re} v\nabla \cdot \tau, \tag{1.1b}$$

$$\frac{Dp}{Dt} + \gamma p(\nabla \cdot \boldsymbol{u}) = \frac{1}{Re}(\gamma - 1)[(\nabla \boldsymbol{u}) : \tau] \tag{1.1c}$$

$$+ \frac{\gamma}{PrRe}(v\nabla^2 p + 2\nabla v \cdot \nabla p + p\nabla^2 v), \tag{1.1d}$$

for the stress tensor

$$\tau = \mu\Big(\nabla \boldsymbol{u} + (\nabla \boldsymbol{u})^T\Big) - \Big(\frac{2}{3}\mu - \kappa\Big)(\nabla \cdot \boldsymbol{u})I, \tag{1.1e}$$

where μ is the dynamic viscosity and κ is the bulk viscosity. We take the bulk viscosity to be zero ($\kappa = 0$) and we introduce the Reynolds number, the Prandtl number, and the Blasius length scale

$$Re = \frac{\rho^*_\infty \delta^*_0 a^*_\infty}{\mu^*_\infty}, \quad Pr = \frac{c^*_{p,\infty}\mu^*_\infty}{k^*_\infty}, \quad \delta^*_0 = \sqrt{\frac{\mu^*_\infty x^*_0}{\rho^*_\infty U^*_\infty}}.$$

Here v^*_∞ denotes the free-stream specific volume, μ^*_∞ the free-stream dynamic viscosity, k^*_∞ the free-stream thermal diffusivity, $c^*_{p,\infty}$ the free-stream specific heat

capacity at constant pressure, and a^*_∞ the free-stream sound speed, while x, y, z, correspond to the streamwise, transverse and spanwise directions, respectively. To avoid confusion with the kinematic viscosity, we use the free-stream density, ρ^*_∞, in the definition of our dimensionless variables. At low Mach numbers, temperature fluctuations are minimal, so we take the fluid properties (μ, k, and c_p) to be constant. Throughout this work, we also use the following dimensionless quantities:

$$Re_x = \frac{\rho^*_\infty U^*_\infty x^*}{\mu^*_\infty}, \quad y = \frac{y^*}{\delta^*_0}, \quad F = \frac{\omega^* \mu^*_\infty}{\rho^*_\infty U^{*2}_\infty}, \quad b = \frac{\beta^* \mu^*_\infty}{\rho^*_\infty U^*_\infty},$$

where Re_x is the streamwise coordinate, F is the temporal frequency, and b is the spanwise wavenumber.

1.3 Laminar-turbulent transition in boundary-layer flows

We briefly review the developments in boundary-layer transition prediction and introduce key definitions and concepts relevant to the transition process.

1.3.1 A brief history of laminar-turbulent transition

Orr (1907) and Sommerfeld (1908) independently formulated a linear eigenvalue problem, now known as the Orr–Sommerfeld (OS) equation, to study viscous instabilities in two-dimensional (2D) parallel flows. Meanwhile, Prandtl (1904) hypothesized the existence of the boundary layer and employed scaling arguments to simplify the Navier–Stokes equations within this region. Building on Prandtl's theory, Blasius (1908) derived a similarity solution for the steady boundary layer that develops on a semi-infinite flat plate aligned with a constant unidirectional flow. Later, Tollmien (1929) and Schlichting (1933) independently solved the OS equation for the Blasius boundary-layer profile. Their analyses revealed the presence of at most one unstable mode, now known as the Tollmien–Schlichting (TS) wave, and enabled the prediction of the critical Reynolds number at which the TS wave becomes unstable.

Early experiments attributed transition to high levels of freestream turbulence rather than exponential growth of the TS wave, but Schubauer and Skramstad (1947) confirmed the existence of TS waves by using damping screens to ensure low levels of freestream turbulence, showing excellent agreement with theoretical predictions. Schubauer and Skramstad initially investigated naturally occurring disturbances from small freestream fluctuations, later introducing a vibrating ribbon to control their frequency and amplitude. In a similar setup, Klebanoff et al. (1962) placed evenly spaced tape strips along the plate's leading edge to generate oblique waves

at the same frequency as the fundamental TS wave. Although initially weaker, these oblique waves interact with the TS wave, amplifying both themselves and their higher harmonics. This interaction leads to the formation of aligned Λ-vortex structures, characteristic of the transition path now known as the fundamental (or K-type, for Klebanoff) path. Similar experiments by Kachanov and Levchenko (1984) identified the subharmonic path in which the oblique waves have half the temporal frequency of the fundamental TS wave, while the Λ-vortex structure is staggered and transition is delayed relative to the fundamental path. Herbert (1988) developed a secondary stability theory, using Floquet analysis, to study these transition paths, so the subharmonic path is also called the H-type path after Herbert.

For high-speed boundary-layer flows, Mack (1984) identified unstable eigenmodes now known as Mack modes. Mack's first mode is the high-speed analog of the TS wave, as both are viscous in nature. However, the TS wave is most unstable for two-dimensional disturbances ($\beta = 0$), while Mack's first mode is most unstable for oblique disturbances ($\beta \neq 0$). Mack's first mode is the primary disturbance leading to transition for Mach numbers up to 4.5, while the higher Mack modes, which are non-viscous, are the primary instabilities leading to transition for Mach numbers higher than 4.5.

1.3.2 Notions of stability

Disturbances to the flow lead to flow instabilities, which can be classified either as *absolute* or *convective* instabilities according to the definitions of Huerre and Monkewitz (1985):

Definition 1.3.1 (absolute instability) *Consider a disturbance introduced at* $\boldsymbol{x} = 0$ *and* $t = 0$*, then it is an absolute instability if its amplitude grows as* $t \to \infty$ *for all* $\boldsymbol{x}$*.*

Definition 1.3.2 (convective instability) *Consider a disturbance introduced at* $\boldsymbol{x} = 0$ *and* $t = 0$*, then it is a convective instability if it is swept away from* $\boldsymbol{x} = 0$ *such that the system returns to its unperturbed state as* $t \to \infty$*.*

Figure 1.1 compares absolute and convective instabilities in the $x - t$-plane using Figure 7.6 from Schmid and Henningson (2001). Note that the TS wave, and other disturbances to boundary-layer flows, are convective in nature, so this work will focus on these types of instabilities.

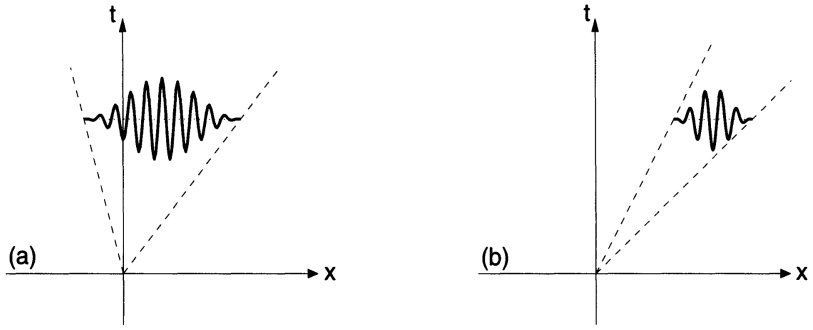

Figure 1.1: Sketch of convective and absolute stability from Figure 7.6 in Schmid and Henningson (2001): (a) $x - t$ plane diagram of an absolutely unstable disturbance; (b) $x - t$ plane diagram of a convectively unstable disturbance.

1.3.3 Types of disturbances

We divide disturbances into the following three categories: (i) modal, (ii) multi-modal, and (iii) non-modal.

Definition 1.3.3 (modal disturbance) *For a specified frequency, a disturbance that propagates in the streamwise direction with a well-defined streamwise wavelength.*

Definition 1.3.4 (multi-modal instabilities) *For a specified frequency, there are multiple modal disturbances, each evolving with different streamwise wavelengths.*

Definition 1.3.5 (non-modal instabilities) *The linearized Navier-Stokes operator is non-normal so that its eigenvectors are not mutually orthogonal. Therefore, the superposition of linearly stable modes can temporarily increase in magnitude, even as each mode decays, leading to transient growth.*

The TS wave is a modal disturbance, as illustrated in Figure 1.2, which shows contours of the streamwise (u) and wall-normal (v) velocity disturbances. These contours demonstrate that the TS wave evolves with a well-defined streamwise wavelength, characteristic of a modal instability. Low-speed boundary-layer flows typically experience only modal disturbances, while multi-modal disturbances are characteristic of high-speed flows (Fedorov, 2011).

Figure 1.3 uses Figure 4.1 from Schmid and Henningson (2001) to illustrate transient growth. Both vectors Φ_1 and Φ_2 are decaying, but their superposition temporarily grows in time due to the mutual non-orthogonality. Appendix J investigates transient growth for low-speed boundary-layer flows.

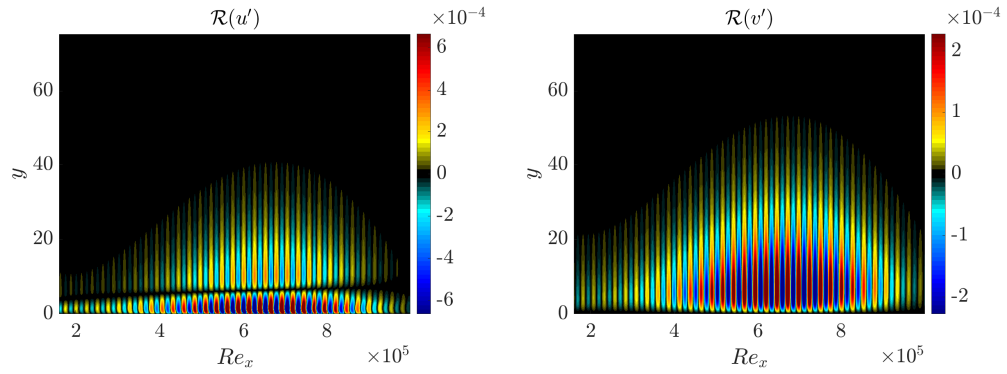

(a) u-velocity contour (b) v-velocity contour

Figure 1.2: Contours of the u- and v-velocity disturbance contours for the 2D TS wave, demonstrating that it evolves with a well-defined wavelength that is constant in the streamwise direction.

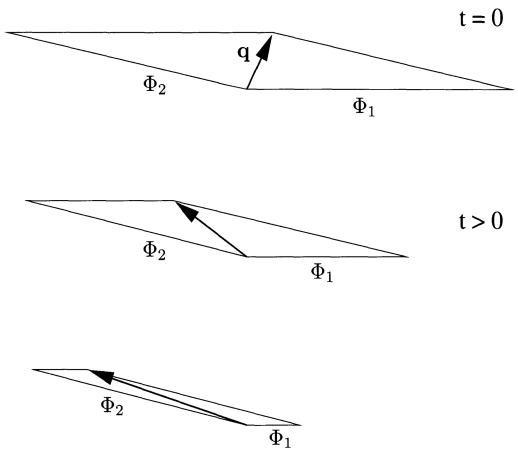

Figure 1.3: Figure 4.1 from Schmid and Henningson (2001) illustrating transient growth due to non-orthogonal superposition of two decaying vectors.

1.3.4 Paths to transition for compressible boundary-layer flows

Initially disturbances enter the boundary-layer flow through a process known as *receptivity*, in which energy from the free stream enters and excites instability waves inside the boundary layer (Morkovin, 1969). Following receptivity, there are multiple paths to transition, as discussed by Morkovin et al. (1994). Figure 1.4 reproduces Figure 1 from Fedorov (2011), adapted from Morkovin et al. (1994), which presents the different transition paths. We summarize them as follows:

- Modal path: if the initial disturbances are sufficiently small, then modal growth is the dominant growth mechanism, and the disturbances grow exponentially before reaching triggering secondary instabilities and reaching the nonlinear

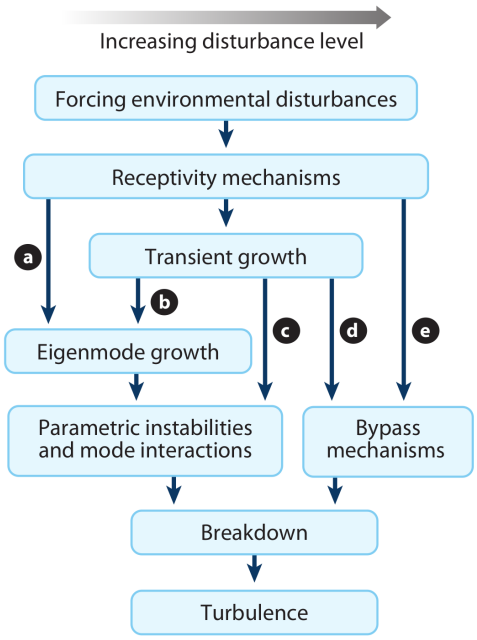

Figure 1.4: Figure 1 from Fedorov (2011), adapted from Morkovin et al. (1994), showing transition paths in boundary-layer flows.

regime.

- Transient path: if the modal disturbances are initially linearly stable, then non-orthogonality can transient growth to increase disturbance amplitude prior to reaching the region of the flow where the modal disturbances are linearly unstable. If the transient growth is sufficiently large, then secondary instabilities can be triggered without exponential growth.

- Bypass path: if the free-stream disturbances are sufficiently large, or if the transient growth is sufficiently large, then bypass transition can be triggered, where the nonlinear regime is reached directly (without exponential growth and secondary instabilities).

This work will focus on the modal path to transition, while future work could investigate transient growth.

1.4 Methods for hydrodynamic stability analysis

In hydrodynamic stabiltiy analysis we study the evolution of a time-varying disturbance, $\boldsymbol{q}'$, to a time-invariant equilibrium solution, $\bar{\boldsymbol{q}}$. Therefore, we decompose the

flow into terms associated with $\bar{\boldsymbol{q}}$ and $\boldsymbol{q}'$, as described in appendix A, yielding the stability equations (A.6), for the vector of primitive variables $\boldsymbol{q} = (v, u, v, w, p)$.

1.4.1 Locally-parallel linear stability theory

The theory developed by Tollmien and Schlichting is now known as locally-parallel linear stability theory (LST). In LST, the flow is assumed locally parallel, meaning the base flow does not vary in the streamwise direction ($\partial_x \bar{\boldsymbol{q}} = \partial_{xx} \bar{\boldsymbol{q}} = 0$), and the wall-normal velocity vanishes ($\bar{v} = 0$), so the boundary-layer thickness remains constant. We consider the spatial stability problem with the following wave-like ansatz for the disturbance:

$$\boldsymbol{q}'(x, y, z, t) = \hat{\boldsymbol{q}}(y) \exp\left(i \int_{x_0}^{x} \alpha(\bar{x})\, d\bar{x} + i(\beta z - \omega t) \right), \tag{1.2}$$

where $\hat{\boldsymbol{q}}$ is the eigenfunction, ω the temporal frequency, α the streamwise wavenumber, β the spanwise wavenumber, and x the streamwise coordinate. While stability studies of low-speed boundary layers often express the streamwise location in terms of $R = \sqrt{Re_x}$, we use Re_x throughout this work.

Tollmien and Schlichting conducted temporal stability analysis, which assumes that disturbances grow in time. However, disturbances to boundary-layer flows grow in the streamwise direction, so later studies instead solved the spatial stability problem. In this approach, the streamwise coordinate x, spanwise wavenumber β, and temporal frequency ω are specified, with β and ω real-valued. The complex streamwise wavenumber α and eigenfunction $\hat{\boldsymbol{q}}(x)$ must then satisfy

$$i\alpha\, \hat{\boldsymbol{q}}(x) = L(\omega, \beta, x)\, \hat{\boldsymbol{q}}(x), \tag{1.3}$$

where $L(\omega, \beta, x)$ is the linear operator governing spatial stability. Disturbances are unstable if $\alpha_i < 0$, stable if $\alpha_i > 0$, and neutrally stable if $\alpha_i = 0$. The TS wave exhibits two neutral stability points, termed branches I and II, and is stable except within $x \in (x_{\mathrm{I}}, x_{\mathrm{II}})$. The growth of the TS wave amplitude is given by

$$\ln\left(\frac{A(x)}{A_0} \right) = -\int_{x_0}^{x} \alpha_i(\bar{x})\, d\bar{x}, \tag{1.4}$$

where $A(x)$ is the disturbance amplitude and A_0 is the disturbance amplitude at branch I. Building on Tollmien and Schlichting's initial work for incompressible flows, Mack (1984) extended the theory to hypersonic boundary layers. We further note that for H- and K-type transition, although LST can be used to predict the growth of the TS and oblique waves separately, the growth of the oblique wave is affected substantially by the TS wave. Therefore, Herbert (1988) introduced a secondary stability theory, using Floquet analysis, to account for this effect.

1.4.2 Linear global stability analysis

LST is computationally efficient, but neglects history and non-parallel effects, which can be included using linear global stability analysis (GSA). In GSA, we specify an inlet disturbance at x_{In} and/or a forcing function for $x \in [x_{\mathrm{In}}, x_{\mathrm{Out}}]$, and solve for the resulting disturbance. However, this approach entails high computational and memory costs because a large linear system of equation, $O(N_x \times N_y \times N_z)$ must be solved. Here N_x, N_y, and N_z denote the resolution in x, y, and z, respectively. Moreover, the disturbances associated with high-speed boundary-layer flows evolve with short wavelength over long streamwise domains, so that global methods are particularly expensive for these flows (Fedorov, 2011).

1.4.3 The Parabolized Stability Equations

The linear parabolized stability equations (PSE) also include history and non-parallel effects, and entail much lower computational and memory costs than GSA (Bertolotti et al., 1992). PSE uses a wavelike ansatz

$$\boldsymbol{q}'(x,y,z,t) = \hat{\boldsymbol{q}}(x,y) e^{i\int_{x_0}^{x}\alpha(\bar{x})d\bar{x}} e^{i(\beta z-\omega t)},$$

so that

$$\begin{aligned}
\frac{\partial \boldsymbol{q}'}{\partial x} &= \left(\frac{\partial \hat{\boldsymbol{q}}}{\partial x} + i\alpha\hat{\boldsymbol{q}}\right) e^{i\int_{x_0}^{x}\alpha(\bar{x})d\bar{x}} e^{i(\beta z-\omega t)}, \\
\frac{\partial^2 \boldsymbol{q}'}{\partial x^2} &= \left(i\frac{\partial \alpha}{\partial x}\hat{\boldsymbol{q}} + 2i\alpha\frac{\partial \hat{\boldsymbol{q}}}{\partial x} - \alpha^2\hat{\boldsymbol{q}}\right) e^{i\int_{x_0}^{x}\alpha(\bar{x})d\bar{x}} e^{i(\beta z-\omega t)},
\end{aligned}$$

where we have assumed that $\partial^2\hat{\boldsymbol{q}}/\partial x^2 = 0$. In addition, nonlinear analyses can be performed using the nonlinear PSE (NPSE).

PSE has proven effective for boundary-layer flows (Bertolotti et al., 1992; Herbert, 1997; Paredes et al., 2015; Chang et al., 1993; Chang and Malik, 1994; Paredes et al., 2016a; Joslin et al., 1993) and mixing layers (Day, 1999; Day et al., 2001). However, to achieve a stable march, PSE relies on *ad hoc* regularization techniques (Li and Malik, 1996; Li and Malik, 1997; Broadhurst and Sherwin, 2008) to suppress (rather than eliminate) upstream-propagating waves. This introduces a minimum step size requirement for numerical stability, which limits the streamwise resolution. Furthermore, Towne et al. (2019) demonstrated that PSE is generally not accurate for multi-modal disturbances because it can track only the most dominant disturbance, and that the other disturbances are neither necessarily damped away, nor properly evolved. While some studies have reported success when applying PSE to *non-modal* disturbances (transient growth) (De Tullio et al., 2013; Paredes et al., 2016a; Hack

and Moin, 2017), others have documented limitations and challenges (Cheung and Lele, 2007; Rodríguez et al., 2018). Although PSE has been applied to hypersonic boundary-layer flows (Pruett et al., 1995; Paredes et al., 2016b; Lakebrink et al., 2017), such flows often feature multiple discrete modes and disturbance branches that can synchronize, which proves challenging for PSE (Towne et al., 2019; Fedorov, 2011).

1.4.4 The One-Way Navier-Stokes equations

Towne and Colonius (2015) developed the linear One-Way Navier–Stokes (OWNS) equations, which use recursive filtering to construct efficient and well-posed one-way approximations to linear hyperbolic systems. This original formulation, now known as OWNS outflow (OWNS-O), is based on non-reflective boundary conditions for outflow boundaries and is limited to homogeneous (unforced) equations. To address this, Towne et al. (2022) introduced OWNS projection (OWNS-P), which extends the method to inhomogeneous (forced) equations. Subsequently, Zhu and Towne (2023) developed OWNS recursive (OWNS-R), offering a more computationally efficient approach for inhomogeneous equations compared to OWNS-P.

OWNS overcomes several limitations of the Parabolized Stability Equations (PSE), particularly by correctly removing all upstream-traveling waves. As a result, it avoids the minimum step-size requirement and accurately captures non-modal and multi-modal instabilities (Towne et al., 2019). The method has been applied to low-speed boundary-layer flows by Rigas et al. (2017a) and extended to high-speed boundary-layer flows by Kamal et al. (2020).

1.4.5 Empirical methods for transition prediction

The linear methods discussed above can be combined with empirical correlations to predict transition. For example, the e^N method (Smith et al., 1956; Van Ingen et al., 1956) computes the N-factor

$$N = \max_x \ln\left(\frac{A(x)}{A_0}\right), \tag{1.5}$$

and predicts transition for $N > 9$. While effective for low-speed flows, the method faces challenges for high-speed flows (Fedorov, 2011).

1.5 Frequency domain analysis

Time-marching, with finite difference discretization in the spanwise direction, allows all frequencies and wavenumbers to be considered simultaneously, as long as they are

resolved properly using a sufficiently refined grid and time step. If the disturbances are periodic, then they can be represented using a Fourier series

$$\boldsymbol{q}'(x,y,z,t) = \sum_{m=-M}^{M} \sum_{n=-N}^{N} \hat{\boldsymbol{q}}_{mn}(x,y,z) e^{i(\beta z - m\omega t)}, \tag{1.6}$$

where ω and β are the fundamental frequency and fundamental wavenumber, respectively. We do not discuss in detail conditions under which Fourier series converge, but note that increasing M and N will generally lead to a better approximation.

In flight and wind tunnel tests, multiple modes and frequencies are excited simultaneously, which broadband forcing can replicate. However, this complicates analysis due to overlapping transition scenarios (e.g., oblique-wave breakdown, fundamental, or subharmonic transition). Although not representative of experiments, selectively forcing dominant instabilities at specific frequencies and spanwise wavenumbers enables focused study of individual transitions. While NOWNS could be applied to study periodic broadband disturbances, this would require many Fourier components to converge. Instead, NOWNS is better suited for selective forcing of dominant frequencies and wavenumbers. We demonstrate throughout this work that NOWNS can rapidly and accurately simulate such transition scenarios. We further note that NOWNS is well-suited to do so, compared to time domain analysis, since time domain analysis must time march through a transient to reach to a periodic state, which require small time-steps and many periods of the fundamental frequency to achieve.

1.6 Outline of thesis

The goal of this work is to develop the nonlinear OWNS (NOWNS) procedure and use it to predict laminar-turbulent transition for boundary-layer flows. Chapter 2 reviews OWNS-P and OWNS-R, while Chapter 3 extends OWNS-P to include nonlinear effects and validates it for low-speed boundary-layer flows. Chapter 5 applies NOWNS to transition prediction for low-speed boundary-layer flows. Chapter 4 develops a greedy algorithm for recursion parameter selection, which is demonstrated for high-speed boundary-layer flows in Chapter 6. We make recommendations for future work and concluding remarks in chapter 7.

Chapter 2

ONE-WAY MARCHING OF LINEAR HYPERBOLIC EQUATIONS

This section reviews the OWNS-P and OWNS-R formulations in preparation for the exposition of NOWNS in Chapter 3, and for the greedy recursion parameter selection algorithm in Chapter 4.

2.1 Introduction

Many physical phenomena, such as wave propagation, can be modeled by (linear) systems of hyperbolic partial differential equations (PDEs), solvable either as time-domain initial boundary value problems or frequency-domain elliptic boundary value problems. When wave propagation is predominantly unidirectional, one-way (parabolic) wave equations can be used to evolve the downstream-going solution. For accuracy and well-posedness, the one-way equation must retain the downstream-going waves, while not supporting any of the upstream-going waves.

One-way wave equations can be obtained by factoring the dispersion relation in Fourier–Laplace space into upstream- and downstream-going factors, and then retaining only the downstream-going branch. Since the resulting equation contains a square root of the Fourier-Laplace variables, the transformation back to physical space results in a nonlocal integro-differential equation, which can be localized using rational approximations of the square root (Lee et al., 2000). Although these methods are accurate, well-posed, and efficient for simple wave equations (Trefethen and Halpern, 1986; Halpern and Trefethen, 1988) such as the equations for geophysical migration of seismic waves (Claerbout, 1976, 1985) and underwater acoustics (Collins, 1989; Jensen et al., 1995), they can only be applied in cases where the eigenvalues can be determined analytically, since the dispersion relation must be factored analytically. Methods for one-way marching that do not depend on this factorization have been developed by Guddati (2006) for acoustic and elastic wave equations, and by Towne and Colonius (2015) for general hyperbolic systems.

To avoid factoring the dispersion relation, the method of Towne and Colonius first discretizes the transverse directions, yielding a semi-discrete ordinary differential equation (ODE) in the marching direction (2.7). An eigendecomposition of the

discretized operator, M in (2.7), then enables classification of its eigenvectors as upstream- or downstream-going via Briggs' criterion (Briggs, 1964), allowing construction of a one-way equation. However, to avoid taking the eigendecomposition, a recursive filter based on work by Givoli and Neta (2003) and Hagstrom and Warburton (2004) for non-reflective boundary conditions (NRBCs) at "outflow" boundaries is used to construct an approximation to the one-way equation. The framework has been extensively refined and generalized for the linearized Navier-Stokes equations (Towne et al., 2022; Kamal et al., 2020, 2021, 2022; Rigas et al., 2017a). For simplicity, we will refer to the general framework as the One-Way Navier-Stokes (OWNS) equations, but note that many of the techniques are broadly applicable to other hyperbolic systems.

The OWNS projection method (OWNS-P) generalizes the approach to handle inhomogeneous (forced) equations (Towne et al., 2022). Both OWNS-O and OWNS-P involve high computational costs compared to PSE, which motivated the development of the more efficient OWNS recursive method (OWNS-R) (Zhu and Towne, 2023). We also note that a similar method, which uses recursive filters to approximate the eigenvectors of M for wave propagation in complex media, has been developed by Rudel et al. (2022).

2.2 OWNS equations

Here we will develop the OWNS approach for a general linear system of hyperbolic equations. First we note that a hyperbolic system is defined as in Definition 2.2.1.

Definition 2.2.1 (Hyperbolic system of first-order equations) *Consider the following system of first-order partial differential equations for N unknown functions $\boldsymbol{q}' = (q'_1, \ldots, q'_N)$, $\boldsymbol{q} = \boldsymbol{q}(x, \boldsymbol{y}, t)$ where $\boldsymbol{y} \in \mathbb{R}^{d-1}$ and $\boldsymbol{\tau}^j \in C^1(\mathbb{R}^N, \mathbb{R}^N)$ are once continuously differentiable (nonlinear) functions:*

$$\frac{\partial \boldsymbol{q}'}{\partial t} + \frac{\partial}{\partial x}\boldsymbol{\tau}^j(\boldsymbol{q}') + \sum_{j=2}^{d} \frac{\partial}{\partial x_j}\boldsymbol{\tau}^j(\boldsymbol{q}') = 0. \tag{2.1}$$

We introduce the Jacobians

$$B_j = \begin{bmatrix} \frac{\partial \tau_1^j}{\partial q'_1} & \cdots & \frac{\partial \tau_1^j}{\partial q'_N} \\ \vdots & \ddots & \vdots \\ \frac{\partial \tau_N^j}{\partial q'_1} & \cdots & \frac{\partial \tau_N^j}{\partial q'_N} \end{bmatrix}, \quad j = 1, \ldots, N, \quad A = B_1, \tag{2.2}$$

and we say that (2.1) *is hyperbolic if for all* $\gamma_1, \ldots, \gamma_d \in \mathbb{R}$ *the matrix*

$$\gamma_1 A + \gamma_2 B_2 + \cdots + \gamma_d B_d$$

has only real eigenvalues and is diagonalizable.

Consider the constant-coefficient hyperbolic system of equations

$$\frac{\partial \boldsymbol{q}'}{\partial t} + A\frac{\partial \boldsymbol{q}'}{\partial x} + \sum_{j=2}^{d} B_j \frac{\partial \boldsymbol{q}'}{\partial y_j} + C\boldsymbol{q}' = \boldsymbol{f}, \tag{2.3}$$

in d spatial-dimensions for $A, B_j, C \in \mathbb{R}^{N\times N}$ with A and B_j defined as in (2.2), with forcing function $\boldsymbol{f} \in \mathbb{R}^N$ where $\boldsymbol{f} = \boldsymbol{f}(x, \boldsymbol{y}, t)$.

Remark 2.2.2 *System* (2.3) *is a general first-order linear hyperbolic system of equations. We delay writing explicit expressions for A,* B_j *and C until Chapter 3 where we specialize the approach to the Navier-Stokes equations, for the operators presented in Appendix A.*

Applying finite differences (or other discretizations) in $(y_2, \ldots, y_d)$ yields

$$\frac{\partial \boldsymbol{q}'}{\partial t} + A\frac{\partial \boldsymbol{q}'}{\partial x} + \sum_{j=2}^{d} B_j D_j \boldsymbol{q}' + C\boldsymbol{q}' = \boldsymbol{f}, \tag{2.4}$$

for the difference operator D_j. Since (2.3) is hyperbolic, we know that A is diagonalizable with real eigenvalues $\tilde{A} = TAT^{-1}$ and eigenvectors T^{-1}, which we use to define the characteristic variables $\boldsymbol{\phi} = T\boldsymbol{q}'$. Next we write

$$\frac{\partial \boldsymbol{\phi}}{\partial t} + \tilde{A}\frac{\partial \boldsymbol{\phi}}{\partial x} + \sum_{j=2}^{d} \tilde{B}_j \frac{\partial \boldsymbol{\phi}}{\partial y_j} + \tilde{C}\boldsymbol{\phi} = \boldsymbol{f}_\phi, \tag{2.5}$$

where $\tilde{B}_j = TB_jT^{-1}$ for $j = 2, \ldots, d$, $\tilde{C} = TCT^{-1}$, and $\boldsymbol{f}_\phi = T\boldsymbol{f}$. We assume that $\tilde{A}$ is non-singular (we treat the singular case in Appendix C) so that

$$\tilde{A} = \begin{bmatrix} A_{++} & 0 \\ 0 & A_{--} \end{bmatrix} \tag{2.6}$$

for $N_+ \times N_+$ diagonal matrix A_{++} with $A_{++} > 0$ and $N_- \times N_-$ diagonal matrix $A_{--} < 0$, where $N_+ + N_- = N$. Taking a Laplace transform in time, and Fourier transforms in space for $j = 2, \ldots, d$, we obtain

$$\frac{d\hat{\boldsymbol{\phi}}}{dx} = -M(s)\hat{\boldsymbol{\phi}} + \hat{\boldsymbol{f}}_\phi, \tag{2.7}$$

where $\hat{\boldsymbol{\phi}}$ and $\boldsymbol{f}$ represent $\boldsymbol{\phi}$ and $\boldsymbol{f}_\phi$, respectively, in the frequency domain, while

$$M(s) = \tilde{A}^{-1}\Big(sI + \sum_{j=2}^{d} i\omega_j \tilde{B}_j + \tilde{C}\Big). \tag{2.8}$$

For the problems considered in this work, the matrix $M(s)$ is diagonalizable, which simplifies the exposition of the OWNS methodology. Therefore, we assume $M(s)$ to be diagonalizable and note that the defective case is handled by Towne and Colonius (2015).

We use Briggs' criterion (Definition 2.2.3) to classify eigen-vectors as upstream- or downstream-going, while Proposition 2.2.4 tells us that $M(s)$ has precisely N_+ and N_- downstream- and upstream-going eigenvalues.

Definition 2.2.3 (Briggs' criterion) *Consider a wave with complex wave-number $i\alpha = i\alpha_r - \alpha_i$ for some $s = i\omega + \eta$ with real ω and η. Take $\eta \to \infty$, then according to Briggs' criterion, this wave is downstream-going if $\alpha_i \to \infty$, while it is upstream-going if $\alpha_i \to -\infty$ (Briggs, 1964).*

Proposition 2.2.4 *For $\mathcal{R}(s) > 0$, the matrix $M(s)$ has precisely N_+ and N_- downstream- and upstream-going eigenvalues, respectively, according on Briggs' criterion (Towne and Colonius, 2015).*

Proof: The eigenvalues are the solutions to the characteristic equation

$$\det(\tilde{A}^{-1})^{-1} \det(M - i\alpha I) = \det(-sI - \sum_{j=2}^{d} i\omega_j \tilde{B}_j - i\alpha\tilde{A} - \tilde{C}).$$

The eigenvalues are continuous functions of s so taking the limit $\mathcal{R}(s) \to \infty$ yields N_+ eigenvalues with $\mathcal{I}(\alpha) > 0$ and N_- eigenvalues with $\mathcal{I}(\alpha) < 0$. □

We then partition M into upstream- and downstream-going blocks as

$$M = \begin{bmatrix} V_+ & V_- \end{bmatrix} \begin{bmatrix} D_{++} & 0 \\ 0 & D_{--} \end{bmatrix} \begin{bmatrix} V_+ & V_- \end{bmatrix}^{-1}, \tag{2.9}$$

where the columns of $V_+ \in \mathbb{C}^{N \times N_+}$ and $V_- \in \mathbb{C}^{N \times N_-}$ the eigenvectors associated with the downstream- and upstream-going eigenvalues of M, and we have dropped the argument s for brevity. Next we introduce the coefficients $\hat{\boldsymbol{\psi}}_+ \in \mathbb{C}^{N_+}$ and $\hat{\boldsymbol{\psi}}_- \in \mathbb{C}^{N_-}$ such that

$$\hat{\boldsymbol{\phi}} = V_+\hat{\boldsymbol{\psi}}_+ + V_-\hat{\boldsymbol{\psi}}_-, \tag{2.10}$$

while for notational convenience, we define

$$i^{(+)} = 1, \ldots, N_+, \quad i^{(-)} = N_+ + 1, \ldots, N, \tag{2.11}$$

to denote indices associated with downstream- and upstream-going modes, respectively.

2.2.1 Exact projection equations

OWNS-O (Towne and Colonius, 2015) has two notable drawbacks: (i) it does not allow a forcing function, and (ii) it couples upstream- and downstream going modes through dV/dx for flows that vary in the marching direction. These limitations can be overcome by OWNS-P (Towne et al., 2022) and OWNS-R (Zhu and Towne, 2023). Here we introduce the exact one-way projection approach, while we subsequently introduce the approximations to this approach using OWNS-P and OWNS-R. Definitions 2.2.5 and 2.2.8 introduce the exact projection matrix and its associated one-way equations, while Proposition 2.2.10 demonstrates that these one-way equations are consistent with the global equations, even for systems varying in the marching direction. This is in contrast to the OWNS-O approach, which is consistent if and only if it is applied to constant coefficient systems (Towne and Colonius, 2015).

Definition 2.2.5 *We define the one-way projection matrix*

$$P = \begin{bmatrix} V_+ & V_- \end{bmatrix} \begin{bmatrix} I_{++} & 0 \\ 0 & 0 \end{bmatrix} \begin{bmatrix} V_+ & V_- \end{bmatrix}^{-1}, \tag{2.12}$$

which partitions the solution into downstream- and upstream-going components as

$$\hat{\boldsymbol{\phi}}' = P\hat{\phi} = PV\hat{\boldsymbol{\psi}} = \begin{bmatrix} V_+ & V_- \end{bmatrix} \begin{bmatrix} I_{++} & 0 \\ 0 & 0 \end{bmatrix} \begin{bmatrix} \hat{\boldsymbol{\psi}}_+ \\ \hat{\boldsymbol{\psi}}_- \end{bmatrix} = V_+\psi_+, \tag{2.13a}$$

$$\hat{\boldsymbol{\phi}}'' = [I - P]\hat{\phi} = [I - P]V\hat{\boldsymbol{\psi}} = \begin{bmatrix} V_+ & V_- \end{bmatrix} \begin{bmatrix} 0 & 0 \\ 0 & I_{--} \end{bmatrix} \begin{bmatrix} \hat{\boldsymbol{\psi}}_+ \\ \hat{\boldsymbol{\psi}}_- \end{bmatrix} = V_-\hat{\boldsymbol{\psi}}_+. \tag{2.13b}$$

For brevity define

$$E = \begin{bmatrix} I_{++} & 0 \\ 0 & 0 \end{bmatrix}, \tag{2.14}$$

so that $P = VEV^{-1}$.

Proposition 2.2.6 *P is a projection matrix (Towne et al., 2022).*

Proof: We see that

$$P^2 = VEV^{-1}VEV^{-1} = VEV^{-1} = P,$$

where $E^2 = E$, so that $P^2 = P$, and (2.12) is a projection matrix by definition since $P = P^2$. □

Proposition 2.2.7 *P commutes with M (Towne et al., 2022).*

Proof: Diagonal matrices commute with each other so that $ED = DE$ and

$$PM = VEDV^{-1} = VDEV^{-1} = MP.$$

□

Definition 2.2.8 (exact one-way projection equations) *The projection matrix, P, can be used to obtain one-way equations*

$$\frac{\partial \hat{\boldsymbol{\phi}}'}{\partial x} = P[M\hat{\boldsymbol{\phi}}' + \hat{\boldsymbol{g}}], \tag{2.15a}$$

$$\frac{\partial \hat{\boldsymbol{\phi}}''}{\partial x} = [I - P][M\hat{\boldsymbol{\phi}}'' + \hat{\boldsymbol{g}}], \tag{2.15b}$$

for the downstream- and upstream-going modes, respectively (Towne et al., 2022).

Proposition 2.2.9 *The exact one-way projection equations are well-posed as spatial initial value problems according to the criterion of Kreiss (1970).*

Proof: See the discussion by Towne and Colonius (2015) and Towne et al. (2022), the criterion developed by Kreiss (1970), and the review by Higdon (1986). □

Proposition 2.2.10 *The exact one-way projection equations are consistent with the global equations.*

Proof: If $\hat{\boldsymbol{\phi}}'$ and $\hat{\boldsymbol{\phi}}''$ are solutions to (2.15a) and (2.15b), respectively, then summing these equations yields

$$\begin{aligned}\frac{\partial(\hat{\boldsymbol{\phi}}' + \hat{\boldsymbol{\phi}}'')}{\partial x} &= P[M\hat{\boldsymbol{\phi}}' + \hat{\boldsymbol{g}}] + [I - P][M\hat{\boldsymbol{\phi}}'' + \hat{\boldsymbol{g}}] \\ &= MP[\hat{\boldsymbol{\phi}}' + \hat{\boldsymbol{\phi}}''] + M[I - P][\hat{\boldsymbol{\phi}}' + \hat{\boldsymbol{\phi}}''] + \hat{\boldsymbol{g}} \\ &= M[\hat{\boldsymbol{\phi}}' + \hat{\boldsymbol{\phi}}''] + \hat{\boldsymbol{g}},\end{aligned}$$

so that $\hat{\boldsymbol{\phi}}' + \hat{\boldsymbol{\phi}}''$ is a solution to (2.7). If $\hat{\boldsymbol{\phi}}$ is a solution to (2.7), then by linearity

$$\begin{aligned}
\frac{\partial \hat{\boldsymbol{\phi}}}{\partial x} &= M\hat{\boldsymbol{\phi}} + \hat{\boldsymbol{g}} \\
\frac{\partial [P\hat{\boldsymbol{\phi}}]}{\partial x} + \frac{\partial [(I-P)\hat{\boldsymbol{\phi}}]}{\partial x} &= MP\hat{\boldsymbol{\phi}} + P\hat{\boldsymbol{g}} + M(I-P)\hat{\boldsymbol{\phi}} + (I-P)\hat{\boldsymbol{g}} \\
\frac{\partial \hat{\boldsymbol{\phi}}'}{\partial x} + \frac{\partial \hat{\boldsymbol{\phi}}''}{\partial x} &= P[M\hat{\boldsymbol{\phi}}' + \hat{\boldsymbol{g}}] + (I-P)[M\hat{\boldsymbol{\phi}}'' + \hat{\boldsymbol{g}}],
\end{aligned}$$

so that $P\hat{\boldsymbol{\phi}}$ and $(I-P)\hat{\boldsymbol{\phi}}$ are solutions to (2.15a) and (2.15b), respectively. □

Remark 2.2.11 *The exact OWNS projection framework can be re-interpreted using a variational formulation, as shown in Appendix E.*

2.2.2 Approximate projection using OWNS-P

To avoid taking the eigendecomposition of M, OWNS-P uses a recursive filter to approximate the projection matrix (2.12). Definition 2.2.12 introduces this recursive filter, while Proposition 2.2.13 recasts it in a matrix form, where the matrix is a projection matrix by Proposition 2.2.14. Proposition 2.2.15 provides a criterion for OWNS-P convergence, while Proposition 2.2.16 provides a necessary condition for convergent recursion parameters to exist. The error introduced by this approximation is bounded in Proposition 2.2.17, while Proposition 2.2.20 shows that the approximate projection matrix does not generally commute with M.

Definition 2.2.12 *The action of P can be applied approximately using the OWNS-P recursive filter*

$$\hat{\boldsymbol{\phi}}_+^{-N_\beta} = 0 \tag{2.16a}$$

$$(M - i\beta_-^j I)\hat{\boldsymbol{\phi}}^{-j} - (M - i\beta_+^j I)\hat{\boldsymbol{\phi}}^{-j-1} = 0, \quad j = 1, \ldots, N_\beta - 1, \tag{2.16b}$$

$$(M - i\beta_-^0 I)\hat{\boldsymbol{\phi}}^{0} - (M - i\beta_+^0 I)\hat{\boldsymbol{\phi}}^{-1} = (M - i\beta_-^0 I)\hat{\boldsymbol{\phi}}, \tag{2.16c}$$

$$(M - i\beta_+^j I)\hat{\boldsymbol{\phi}}^{j} - (M - i\beta_-^j I)\hat{\boldsymbol{\phi}}^{j+1} = 0, \quad j = 0, \ldots, N_\beta - 1, \tag{2.16d}$$

$$\hat{\boldsymbol{\phi}}_-^{N_\beta} = 0, \tag{2.16e}$$

where (β_+^j, β_-^j) are the recursion parameters and $\hat{\boldsymbol{\phi}}^j$ the auxiliary variables for $j = 0, \ldots, N_\beta - 1$ (Towne et al., 2022).

Proposition 2.2.13 *The recursive filter* (2.16) *can be recast in matrix form*

$$P_{N_\beta} = V R_{N_\beta} E R_{N_\beta}^{-1} V^{-1}, \tag{2.17a}$$

for

$$R_{N_\beta} = \begin{bmatrix} I_{++} & F_{++}V_{++}^{-1}V_{+-}F_{--}^{-1} \\ F_{--}^{-1}V_{--}^{-1}V_{-+}F_{++} & I_{--} \end{bmatrix}^{-1}, \tag{2.17b}$$

where F, which is a diagonal matrix

$$F = \begin{bmatrix} F_{++} & 0 \\ 0 & F_{--} \end{bmatrix}, \quad F_k = \prod_{j=0}^{N_\beta - 1} \frac{\alpha_k - \beta_+^j}{\alpha_k - \beta_-^j}, \quad k = 1, \ldots, N, \tag{2.17c}$$

as shown by Towne et al. (2022).

Proof: See Appendix D.1. □

Proposition 2.2.14 *P_{N_β} is a projection matrix (Towne, 2016).*

Proof: Note that

$$P_{N_\beta}^2 = VR_{N_\beta}ER_{N_\beta}^{-1}V^{-1}VR_{N_\beta}ER_{N_\beta}^{-1}V^{-1} = VR_{N_\beta}ER_{N_\beta}^{-1}V^{-1} = P_{N_\beta},$$

so that it is a projection matrix by definition. □

Proposition 2.2.15 *P_{N_β} converges to P if and only if*

$$\lim_{N_\beta \to \infty} \prod_{j=0}^{N_\beta - 1} \frac{|\alpha_m - \beta_+^j|}{|\alpha_m - \beta_-^j|} \frac{|\alpha_n - \beta_-^j|}{|\alpha_n - \beta_+^j|} = 0, \tag{2.18}$$

for all pairs (α_m, α_n) such that $m = i^{(+)}$ and $n = i^{(-)}$ (Towne et al., 2022).

Proof: See Appendix D.1. □

Proposition 2.2.16 *Recursion parameters such that P_{N_β} converges to P exist if and only if $\alpha_m \neq \alpha_n$ for all $m = i^{(+)}$ and $n = i^{(-)}$. In particular, if $N_+ \leq N_-$, then choose $N_\beta = N_+$ with*

$$\beta_+^{n-1} = \alpha_n, \quad \beta_-^{j-1} \neq \alpha_n, \quad n = 1, \ldots, N_+, \quad j = 1, \ldots, N_+,$$

while if $N_- < N_+$, then choose $N_\beta = N_-$ with

$$\beta_-^{n-1} = \alpha_n, \quad \beta_+^{j-1} \neq \alpha_n, \quad n = N_+ + 1, \ldots, N, \quad j = 1, \ldots, N_-.$$

Proof: See Appendix D.1. □

Proposition 2.2.17 (OWNS-P error bound) *The error introduced by the OWNS-P approximation is bounded by*

$$\|P_{N_\beta} - P\| \leq \|V\|\|F_{++}\|\|F_{--}^{-1}\|\left(\|V_{++}^{-1}V_{+-}\| + \|V_{--}^{-1}V_{-+}\|\right)\|V^{-1}\| + O(\epsilon^2), \quad (2.19a)$$

for $\|F_{++}\|\|F_{--}^{-1}\| < \epsilon$ *where*

$$\epsilon = \min\{\hat{\epsilon}, \|V_{++}^{-1}V_{+-}\|^{-1/2}\|V_{--}^{-1}V_{-+}\|^{-1/2}\}, \quad (2.19b)$$

for some small $\hat{\epsilon} > 0$ *such that* $\hat{\epsilon} \ll 1$. *Here we have used the Euclidean vector norm*

$$\|\boldsymbol{v}\|_2 = \sqrt{|v_1|^2 + \cdots + |v_N|^2}, \quad \boldsymbol{v} \in \mathbb{C}^N, \quad (2.19c)$$

and its induced matrix norm.

$$\|A\|_2 = \sup_{\boldsymbol{v}\neq 0} \frac{\|A\boldsymbol{v}\|_2}{\|\boldsymbol{v}\|_2}, \quad A \in \mathbb{C}^{N\times N}, \quad (2.19d)$$

where we have dropped the subscript for brevity, so that $\|\cdot\| = \|\cdot\|_2$.

Proof: See Appendix D.1. □

Proposition 2.2.18 *If* $\beta_+^j = \alpha_m$ *for any downstream-going mode, it will be retained accurately by the OWNS-P filter; if* $\beta_-^j = \alpha_n$ *for any upstream-going mode, it will be removed.*

Proof: See Appendix D.1. □

Remark 2.2.19 *Proposition 2.2.17 shows that the error* $\|P_{N_\beta} - P\|$ *scales with* $\|F_{++}\|\|F_{--}\|$ *for sufficiently small* $\|F_{++}\|\|F_{--}\|$, *while Proposition 2.2.18 shows it is always possible to achieve zero error for any upstream- or downstream-going mode.*

Proposition 2.2.20 P_{N_β} *commutes with* M *if and only if* $R_{N_\beta}^{-1} = I$.

Proof: If $R_{N_\beta}^{-1} = I$, then

$$P_{N_\beta} M = V R_{N_\beta} E R_{N_\beta}^{-1} V^{-1} M = PM = MP = M P_{N_\beta}.$$

If $R_{N_\beta}^{-1} \neq I$, then $R_{N_\beta}^{-1}$ is not diagonal and does not commute with D, so that $R_{N_\beta}^{-1} D \neq D R_{N_\beta}$, and P_{N_β} does not commute with M. □

Remark 2.2.21 *Proposition 2.2.14 establishes that P_{N_β} is a projection operator for any choice of recursion parameters, while Proposition 2.2.20, in conjunction with Proposition 2.2.15, establishes that P_{N_β} commutes with M if and only if the recursion parameters are chosen such that $P_{N_\beta} = P$.*

Proposition 2.2.22 *The error in treating P_{N_β} and M as if they commute is bounded by*

$$\begin{aligned} \|P_{N_\beta} M - M P_{N_\beta}\| \leq 2\|V\|\|F_{++}\|\|F_{--}^{-1}\|\big(\|V_{++}^{-1} V_{+-}\| \\ + \|V_{--}^{-1} V_{--}\|\big)\|V^{-1}\|\|M\| + O(\epsilon^2), \end{aligned} \tag{2.20}$$

for $\|F_{++}\|\|F_{--}^{-1}\| < \epsilon$ and ϵ as in Proposition 2.2.17.

Proof: See Appendix D.1. □

Remark 2.2.23 *Although P_{N_β} and M do not generally commute, the introduced by treating them as if they commute is small if $\|P - P_{N_\beta}\|$ is small.*

2.2.3 Approximate projection using OWNS-R

OWNS-R constructs approximations to (2.12), but with a reduced computational cost relative to OWNS-P. Definition 2.2.24 presents the OWNS-R recursive filter. Unlike OWNS-P, Proposition 2.2.27 shows that the resulting matrix is not generally a projection, while Proposition 2.2.28 shows that it always commutes with M. Proposition 2.2.30 provides a criterion for convergence, while Proposition 2.2.31 provides a necessary condition for convergent parameters to exist. While Zhu and Towne (2023) suggested that the OWNS-P recursion parameters would also work for OWNS-R, we show in Proposition 2.2.32 that this is not always true. In addition, Proposition 2.2.38 shows that repeated applications of the OWNS-R matrix leads to unbounded growth or decay unless the approximation is fully converged. We then conclude by discussing the practical implementation of OWNS-R in Definition 2.2.40 and Proposition 2.2.41.

Definition 2.2.24 *The action of P can be applied approximately using the matrix*

$$P_{N_\beta}^{(R)} = (I + cZ)^{-1}, \tag{2.21}$$

for

$$Z = \prod_{j=1}^{N_\beta} (M - i\beta_j^+ I)(M - i\beta_j^- I)^{-1}, \tag{2.22}$$

where c is a freely chosen parameter (Zhu and Towne, 2023).

Proposition 2.2.25 *If we define the approximate eigenvalues*

$$E_{N_\beta} = (I + cF)^{-1}, \tag{2.23}$$

then $P_{N_\beta}^{(R)} = VE_{N_\beta}V^{-1}$ (Zhu and Towne, 2023).

Proof: See Appendix D.2 □

Remark 2.2.26 *Zhu and Towne (2023) showed that setting $c = 0$ gives $E_{N_\beta}^{(k)} = 1$, so that the march is unstable since all upstream-going modes are retained. Similarly, taking $c \to \infty$ gives $E_{N_\beta}^{(k)} = 0$, so that the march is stable but inaccurate. Therefore, they recommend taking $c \approx 1$, and so we take $c = 1$ for the rest of this paper.*

Proposition 2.2.27 *The matrix $P_{N_\beta}^{(R)}$ is a projection matrix if and only if $E_{N_\beta}^{(k)} = 1$ or $E_{N_\beta}^{(k)} = 0$ for $k = 1, \ldots, N$.*

Proof: See Appendix D.2. □

Proposition 2.2.28 *The matrix $P_{N_\beta}^{(R)}$ commutes with M for any choice of recursion parameters.*

Proof: Note that

$$P_{N_\beta}^{(R)} M = VE_{N_\beta}DV^{-1} = VDE_{N_\beta}V^{-1} = MP_{N_\beta}^{(R)},$$

since E_{N_β} and D are both diagonal matrices. □

Remark 2.2.29 *OWNS-P always produces a projection matrix (Proposition 2.2.14) but it does not always commute with M (Proposition 2.2.20). Conversely, OWNS-R may not yield a projection matrix (Proposition 2.2.27) but it always commutes with M (Proposition 2.2.28).*

Proposition 2.2.30 *$P_{N_\beta}^{(R)}$ converges to P if and only if $E_{N_\beta}^{(k)} \to 1$ for $k = i^{(+)}$ and $E_{N_\beta}^{(k)} \to 0$ for $k = i^{(-)}$ (Zhu and Towne, 2023).*

Proof: Clearly $P_{N_\beta}^{(R)} \to P$ if and only if $E_{N_\beta} \to E$, while by definition, $E^{(k)} = 1$ for $k = i^{(+)}$ and $E^{(k)} = 0$ for $k = i^{(-)}$, so that $E_{N_\beta} \to E$ if and only if $E_{N_\beta}^{(k)} \to 1$ for $k = i^{(+)}$ and $E_{N_\beta}^{(k)} \to 0$ for $k = i^{(-)}$. □

Proposition 2.2.31 *Recursion parameters such that $P_{N_\beta}^{(R)}$ converges to P exist if and only if $\alpha_m \neq \alpha_n$ for all pairs of $m = i^{(+)}$ and $n = i^{(-)}$. In particular, choose*

$$\beta_+^{m-1} = \alpha_m, \quad \beta_-^{m-1} \neq \alpha_n, \quad m, n = i^{(+)}, \tag{2.24a}$$

$$\beta_-^{n-1} = \alpha_n, \quad \beta_+^{n-1} \neq \alpha_m, \quad m, n = i^{(-)}. \tag{2.24b}$$

Proof: See Appendix D.2. □

Proposition 2.2.32 *The minimal parameter set such that $P_{N_\beta} = P$ for OWNS-P (Proposition 2.2.16) yields $P_{N_\beta}^{(R)} \neq P$ for OWNS-R.*

Proof: If $N_+ < N_-$, then $N_\beta = N_+$, with $\beta_+^{n-1} = \alpha_n$ and $\beta_-^{n-1} \neq \alpha_n$ for $n = i^{(+)}$, and for the upstream-going modes

$$E_{N_\beta}^{(k)} = \frac{\prod_{j=1}^{N_+}(\alpha_k - \beta_-^j)}{\prod_{j=1}^{N_+}(\alpha_k - \beta_-^j) + c\prod_{j=1}^{N_+}(\alpha_k - \beta_+^j)} \neq 0, \quad k = i^{(-)},$$

since $\alpha_k \neq \beta_-^j$ for $k = i^{(-)}$ and $j = i^{(+)}$. Then $P_{N_\beta}^{(R)} \neq P$ since $E_{N_\beta}^{(k)} \neq 0$ for $k = i^{(-)}$. □

Remark 2.2.33 *Zhu and Towne (2023) claimed that the minimal parameter set ensuring OWNS-P convergence also apply to OWNS-R, but Proposition 2.2.32 disproves this, while Proposition 2.2.31 identifies a different minimal set for OWNS-R.*

Proposition 2.2.34 *The error introduced by OWNS-R is bounded by*

$$\|P - P_{N_\beta}^{(R)}\| \leq \max\left\{|c|\|F_{++}\|, \|F_{--}^{-1}\|\right\}\|V\|\|V^{-1}\| + \mathcal{O}(\epsilon^2), \tag{2.25}$$

where $\|F_{++}\|, \|F_{--}\| < \epsilon$ for small $\epsilon > 0$ such that $\epsilon \ll 1$ (Zhu and Towne, 2023).

Proof: See Appendix D.2. □

Proposition 2.2.35 *If $\beta_+^j = \alpha_m$ for any downstream-going mode, it will be retained accurately by the OWNS-R filter; if $\beta_-^j = \alpha_n$ for any upstream-going mode, it will be removed.*

Remark 2.2.36 *Proposition 2.2.34 establishes that the error in introduced by OWNS-R scales with* $\max\{|\|F_{++}\|, \|F_{--}^{-1}\|\}$ *for sufficiently small $\|F_{++}\|$ and $\|F_{--}\|$, while Proposition 2.2.18 shows it is always possible to achieve zero error for any upstream- or downstream-going mode, while Proposition 2.2.18 shows it is always possible to achieve zero error for any upstream- or downstream-going mode.*

Remark 2.2.37 *The OWNS-P error converges with $\|F_{++}\|\|F_{--}^{-1}\|$, so that we have convergence with either $\|F_{--}^{-1}\| = 0$ or $\|F_{++}\| = 0$, while the OWNS-R error scales with* $\max\{|\|F_{++}\|, \|F_{--}^{-1}\|\}$ *so that we must have $\|F_{--}^{-1}\| = \|F_{++}\| = 0$. Thus, OWNS-R generally requires a larger and more carefully chosen parameter set.*

Proposition 2.2.38 *Repeated application of $P_{N_\beta}^{(R)}$ causes unbounded growth if $|E_{N_\beta}^{(k)}| > 1$ and decay to zero if $|E_{N_\beta}^{(k)}| < 1$ for any $k = 1, \ldots, N$. Therefore, repeated applications introduce additional error unless $|E_{N_\beta}^{(n)}| < 1$ for all $n = i^{(-)}$, and $E_{N_\beta}^{(m)} = 1$ for all $m = i^{(+)}$.*

Proof: See Appendix D.2. □

Remark 2.2.39 *By Proposition 2.2.38, $P_{N_\beta}^{(R)}$ should be applied only once for OWNS-R to avoid solution blow-up or decay.*

Definition 2.2.40 *The action of $P_{N_\beta}^{(R)}$ is applied to $\hat{\boldsymbol{\phi}}$ by solving for $\hat{\boldsymbol{\phi}}'_{N_\beta}$ as*

$$\hat{\boldsymbol{\phi}}^0 = \frac{1}{2}\hat{\boldsymbol{\phi}}, \tag{2.26a}$$

$$(M - i\beta_*^j)\hat{\boldsymbol{\phi}}^j = (M - i\beta_-^j)\hat{\boldsymbol{\phi}}^{j-1}, \quad j = 1, \ldots, N_\beta, \tag{2.26b}$$

$$\hat{\boldsymbol{\phi}}'_{N_\beta} = \hat{\boldsymbol{\phi}}_{N_\beta}, \tag{2.26c}$$

where β_*^j are defined such that

$$2\prod_{j=1}^{N_\beta}(\alpha - \beta_*^j) = \prod_{j=1}^{N_\beta}(\alpha - \beta_-^j) + \prod_{j=1}^{N_\beta}(\alpha - \beta_+^j). \tag{2.26d}$$

Proposition 2.2.41 *The action of $P^{(R)}_{N_\beta}$ can be applied using* (2.26)*.*

Proof: See Appendix D.2. □

Remark 2.2.42 *In theory, the OWNS-R error decreases with increasing N_β if both $\|F_{++}\|$ and $\|F_{--}^{-1}\|$ decrease. In practice, computing β_j^* numerically (e.g., via* `roots` *in MATLAB) introduces rounding errors that can prevent convergence.*

2.3 Recursion parameter selection

All three OWNS formulations, as well as the method by Rudel et al., require selecting a set of *recursion parameters* that govern the convergence, stability, and accuracy of the approximation. These parameters are, loosely speaking, estimates of key eigenvalues (or their branches) representing upstream and downstream modes. Previous work has selected them heuristically, based on the Euler equations linearized about a uniform flow Towne and Colonius (2015). We refer to this as the *heuristic* approach, and note that it avoids computing the eigenvalues of M, but requires flow-specific tuning (e.g., different parameters for low- and high-speed boundary layers) and often results in slow error convergence. We delay a more detailed discussion of recursion parmaeter selection until Chapter 4, where we develop a greedy algorithm that automates parameter selection, while also ensuring rapid convergence and stability.

2.4 Summary

We have presented the OWNS-P and OWNS-R formulations for hyperbolic equations. Whereas OWNS-P yields a projection matrix that generally does not commute with M, OWNS-R yields a matrix that commutes with M but is not generally a projection. Although they can use similar recursion parameters, Proposition 2.2.32 shows that there exists parameter sets for which OWNS-P is converged while OWNS-R is not. In general, OWNS-R requires more careful parameter selection for stability and accuracy. Finally, Proposition 2.2.18 and 2.2.35 show that it is always possible to choose recursion parameters such that zero error is achieved for any upstream- or downstream-going mode. We will show in Chapter 3 how the procedure can be applied to the Navier-Stokes equations, and extended to include nonlinear effects.

Chapter 3

NONLINEAR OWNS METHODOLOGY

This chapter has been adapted from Sleeman et al. (2023), Sleeman et al. (2024b), and Sleeman et al. (2025). Here we develop the NOWNS methodology and validate it by comparing to direct numerical simulation (DNS) data for low-speed Blasius boundary-layer flows. The OWNS-P approach presented in Chapter 2 was applied to hyperbolic equations, but the Navier-Stokes equations are not hyperbolic, so we will first demonstrate how to apply one-way marching to the Navier-Stokes equations, as done by Towne et al. (2022).

3.1 Linear OWNS

In Appendix A, we rewrite the Navier-Stokes equations (1.1) in operator form (A.6) for the vector of primitive variables $\boldsymbol{q} = (\nu, u, v, w, p)$, where the nonlinear terms, $F(\boldsymbol{q}')$, are defined as in (A.4), while the linear operator, $\mathcal{L}(\bar{\boldsymbol{q}})$, is defined as in (A.5). To simplify the exposition, we temporarily neglect the streamwise diffusion terms by introducing the exogeneous forcing function $\boldsymbol{f} = \boldsymbol{f}_{\text{forcing}} + \boldsymbol{f}_{\text{viscous}}$ where

$$\boldsymbol{f}_{\text{viscous}} = -B_x(\bar{\boldsymbol{q}})\frac{\partial \boldsymbol{q}'}{\partial x} - B_{xx}(\bar{\boldsymbol{q}})\frac{\partial^2 \boldsymbol{q}'}{\partial x^2} - B_{xy}(\bar{\boldsymbol{q}})\frac{\partial^2 \boldsymbol{q}'}{\partial x \partial y} - B_{xz}(\bar{\boldsymbol{q}})\frac{\partial^2 \boldsymbol{q}'}{\partial x \partial z},$$

represents streamwise diffusion terms associated with the disturbance variable, while $\boldsymbol{f}_{\text{forcing}}$ is an arbitrary forcing function. We then neglect the nonlinear term and re-write equation (A.6) to obtain the linear stability equation

$$A_x(\bar{\boldsymbol{q}})\frac{\partial \boldsymbol{q}'}{\partial x} = \mathcal{L}(\bar{\boldsymbol{q}})\boldsymbol{q}' + \boldsymbol{f}. \tag{3.1}$$

Previous work OWNS has often neglected $\boldsymbol{f}_{\text{viscous}}$ because this simplifies the procedure without significantly impacting its accuracy (Towne and Colonius, 2015; Rigas et al., 2017a; Kamal et al., 2020), but we have found that this term impacts more significantly the nonlinear calculation, as discussed in Appendix G.1, so we re-introduce it (approximately) in Section 3.1.5.

In NOWNS, we consider a system of linear OWNS equations coupled together through the nonlinear term, which acts as an inhomogeneous forcing function taking the place of $\boldsymbol{f}$ in (3.1). The OWNS-O approach (Towne and Colonius, 2015) supports only homogeneous equations, so we must instead consider either the OWNS-P

(Towne et al., 2022) or the OWNS-R (Zhu and Towne, 2023) approaches. OWNS-R entails a reduced computational cost compared to OWNS-P, but we have found OWNS-P to be more robust, so we use it to develop the NOWNS approach.

3.1.1 Semi-discrete equations

Throughout this work, we assume that our disturbances are periodic in the spanwise direction with wavenumber β and in time with frequency ω so that we can expand our disturbances as Fourier series

$$\boldsymbol{q}'(x,y,z,t) = \sum_{m,n=-\infty}^{\infty} \hat{\boldsymbol{q}}_{mn}(x,y) e^{i(n\beta z - m\omega t)}. \tag{3.2}$$

In the linear case, all Fourier modes evolve independently, and we consider a single disturbance of the form $\boldsymbol{q}'(x,y,z,t) = \hat{\boldsymbol{q}}(x,y)e^{i(n\beta z - m\omega t)}$, while we discretize in the wall-normal direction using a 4th-order central finite differences which we represent using $D \approx \partial/\partial y$. Our semi-discrete linear operator is then

$$L(\bar{\boldsymbol{q}}) = i\omega I - [A_y(\bar{\boldsymbol{q}}) + B_y(\bar{\boldsymbol{q}})]D - i\beta[A_z(\bar{\boldsymbol{q}}) + B_z(\bar{\boldsymbol{q}})] \tag{3.3}$$

$$- C(\bar{\boldsymbol{q}}) - B_{yy}(\bar{\boldsymbol{q}})D^2 + \beta^2 B_{zz}(\bar{\boldsymbol{q}}) - i\beta B_{yz}(\bar{\boldsymbol{q}}) = 0, \tag{3.4}$$

and we obtain

$$A_x(\bar{\boldsymbol{q}})\frac{\partial \boldsymbol{q}'}{\partial x} = L(\bar{\boldsymbol{q}})\boldsymbol{q}' + \boldsymbol{f}, \tag{3.5}$$

a system of ODEs in x comprising N_v variables, where $N_v = 5N_y$ ($N_v = 4N_y$) in 3D (2D), for the N_y grid points in y.

3.1.2 Parabolization using the OWNS projection procedure

The above ODEs in x contain components that propagate both upstream and downstream, and cannot be stably integrated without further intervention. Therefore, we remove upstream effects using a projection operator that we apply in the characteristic variables, $\boldsymbol{\phi} = T\boldsymbol{q}'$, where T are the eigenvectors of A_x, while $\tilde{A}_x = TA_xT^{-1}$ are the eigenvalues. Here we have dropped the argument $\bar{\boldsymbol{q}}$ for brevity. We transform our equations to characteristic variables as

$$\tilde{A}_x\frac{\partial \hat{\boldsymbol{\phi}}}{\partial x} = \tilde{L}\hat{\boldsymbol{\phi}} + \hat{\boldsymbol{f}}_\phi. \tag{3.6a}$$

with

$$\tilde{L} = TLT^{-1} - TA_x\frac{\partial T^{-1}}{\partial x} \tag{3.6b}$$

$$\hat{\boldsymbol{f}}_\phi = T\hat{\boldsymbol{f}} \tag{3.6c}$$

where $\tilde{L}$ and $\hat{f_\phi}$ denote the linear operator and forcing function in characteristic variables, respectively. We then re-organize the diagonal matrix $\tilde{A}_x$

$$\tilde{A}_x = \begin{bmatrix} \tilde{A}_{++} & 0 & 0 \\ 0 & \tilde{A}_{--} & 0 \\ 0 & 0 & \tilde{A}_{00} \end{bmatrix}, \tag{3.7}$$

for the N_+ positive eigenvalues $\tilde{A}_{++} > 0$, the N_- negative eigenvalues $\tilde{A}_{--} < 0$, and the N_0 zero eigenvalues $\tilde{A}_{00} = 0$, where $N_0 + N_- + N_+ = N_v$. For a boundary-layer flow, $\tilde{A} = 0$ at the wall ($\bar{u} = 0$) or at a sonic point ($\bar{u} - \bar{c} = 0$). We further define

$$\tilde{A}_{\pm\pm} = \begin{bmatrix} \tilde{A}_{++} & 0 \\ 0 & \tilde{A}_{--} \end{bmatrix}, \qquad \tilde{L}_{\pm 0} = \begin{bmatrix} \tilde{L}_{+0} \\ \tilde{L}_{-0} \end{bmatrix}, \qquad \hat{\boldsymbol{\phi}} = \begin{bmatrix} \hat{\boldsymbol{\phi}}_\pm \\ \hat{\boldsymbol{\phi}}_0 \end{bmatrix},$$
$$\tilde{L}_{\pm\pm} = \begin{bmatrix} \tilde{L}_{++} & \tilde{L}_{+-} \\ \tilde{L}_{-+} & \tilde{L}_{--} \end{bmatrix}, \qquad \tilde{L}_{0\pm} = \begin{bmatrix} \tilde{L}_{0+} & \tilde{L}_{0-} \end{bmatrix}, \qquad \hat{\boldsymbol{f}}_\phi = \begin{bmatrix} \hat{\boldsymbol{f}}_{\phi,\pm} \\ \hat{\boldsymbol{f}}_{\phi,0} \end{bmatrix},$$

and so that our equations become

$$\tilde{A}_{\pm\pm} \frac{\partial \hat{\boldsymbol{\phi}}_\pm}{\partial x} = \tilde{L}_{\pm\pm} \hat{\boldsymbol{\phi}}_\pm + \tilde{L}_{\pm 0} \hat{\boldsymbol{\phi}}_0 + \hat{\boldsymbol{f}}_{\phi,\pm}, \tag{3.8a}$$
$$0 = \tilde{L}_{0\pm} \hat{\boldsymbol{\phi}}_\pm + \tilde{L}_{00} \hat{\boldsymbol{\phi}}_0 + \hat{\boldsymbol{f}}_{\phi,0}, \tag{3.8b}$$

which is a differential algebraic equation (DAE) of index 1. We can use the algebraic constraint (3.8b) to obtain $\hat{\boldsymbol{\phi}}_0 = -\tilde{L}_{00}^{-1}[\tilde{L}_{0\pm}\hat{\boldsymbol{\phi}}_\pm + \hat{\boldsymbol{f}}_{\phi,0}]$ so that we can re-write our DAE as an ODE

$$\frac{\partial \hat{\boldsymbol{\phi}}_\pm}{\partial x} = M \hat{\boldsymbol{\phi}}_\pm + \hat{\boldsymbol{g}}, \tag{3.9}$$

for $M = \tilde{A}_{\pm\pm}^{-1}[\tilde{L}_{\pm\pm} - \tilde{L}_{\pm 0}\tilde{L}_{00}^{-1}\tilde{L}_{0\pm}]$, and $\hat{\boldsymbol{g}} = \tilde{A}_{\pm\pm}^{-1}[\hat{\boldsymbol{f}}_{\phi,\pm} - \tilde{L}_{\pm 0}L_{00}^{-1}\hat{\boldsymbol{f}}_{\phi,0}]$.

The upstream- and downstream-going modes of (3.9) can be determined based on the eigenvalues of M, according to Brigg's criterion from definition 2.2.3 (Briggs, 1964) to introduce the projection operator from definition 2.2.5, as described in (Towne and Colonius, 2015; Towne et al., 2022). Then we obtain the linear OWNS equation from definition 2.2.8, yielding the equation for the downstream-going solution

$$\frac{\partial \hat{\boldsymbol{\phi}}'_\pm}{\partial x} = P[M \hat{\boldsymbol{\phi}}'_\pm + \hat{\boldsymbol{g}}], \tag{3.10}$$

where we used that P and M commute, as shown by Towne et al. (2022).

3.1.3 Approximate projection operator

Exact OWNS is prone to numerical error and entails a high computational cost to compute the eigenvalues and eigenvectors of the linear operator. Therefore, instead apply the projection operator approximately using a recursive filter (Towne and Colonius, 2015; Towne et al., 2022). Whereas in definition 2.2.12 we apply the filter to the variable $\hat{\phi}$, here we instead apply the filter to the residual. We define the residuals $\hat{\boldsymbol{r}}_\pm(\boldsymbol{\phi}) = \tilde{A}_{x,\pm\pm}^{-1}[\tilde{L}_{\pm\pm}\hat{\boldsymbol{\phi}}_\pm + \tilde{L}_{\pm 0}\hat{\boldsymbol{\phi}}_0 + \hat{\boldsymbol{f}}_{\phi,\pm}]$, and $\hat{\boldsymbol{r}}_0(\boldsymbol{\phi}) = \tilde{L}_{0\pm}\hat{\boldsymbol{\phi}}_\pm + \tilde{L}_{00}\hat{\boldsymbol{\phi}}_0 + \hat{\boldsymbol{f}}_{\phi,0}$ based on (3.8), and following the approach of Towne et al. (Towne et al., 2022), we can apply P approximately to the residual using the recursive filter

$$\hat{\boldsymbol{r}}_+^{(-N_b)} = 0 \tag{3.11a}$$

$$(\tilde{L} - i\beta_-^{(j)}\tilde{A})\hat{\boldsymbol{r}}^{(-j)} - (\tilde{L} - i\beta_+^{(j)}\tilde{A})\hat{\boldsymbol{r}}^{(-j-1)} = 0, \quad j = 1, \ldots, N_b - 1 \tag{3.11b}$$

$$(\tilde{L} - i\beta_-^{(0)}\tilde{A})\hat{\boldsymbol{r}}^{(0)} - (\tilde{L} - i\beta_+^{(0)}\tilde{A})\hat{\boldsymbol{r}}^{(-1)} = (\tilde{L} - i\beta_-^{(0)}\tilde{A})\hat{\boldsymbol{r}} \tag{3.11c}$$

$$\hat{\boldsymbol{r}}_0^{(0)} = \hat{\boldsymbol{r}}_0, \tag{3.11d}$$

$$(\tilde{L} - i\beta_+^{(j)}\tilde{A})\hat{\boldsymbol{r}}^{(j)} - (\tilde{L} - i\beta_-^{(j)}\tilde{A})\hat{\boldsymbol{r}}^{(j+1)} = 0, \quad j = 0, \ldots, N_b - 1 \tag{3.11e}$$

$$\hat{\boldsymbol{r}}_-^{(N_b)} = 0, \tag{3.11f}$$

where $\hat{\boldsymbol{r}}_0 = 0$ when the algebraic constraint (3.8b) is satisfied. We introduce the vector auxiliary variables $\hat{\boldsymbol{r}}_{\text{aux}} \in C^{N_{\text{aux}}}$, and the approximate projection operators $P_1 \in \mathbb{C}^{N_{\text{aux}} \times N_v}$, $P_2 \in \mathbb{C}^{N_{\text{aux}} \times N_{\text{aux}}}$, $P_3 \in \mathbb{R}^{N_\pm \times N_{\text{aux}}}$, where $P_1\hat{\boldsymbol{r}}$ and $P_2\hat{\boldsymbol{r}}_{\text{aux}}$ give the right- and left-hand sides of (3.11), respectively, while P_3 extracts $\hat{\boldsymbol{r}}_\pm^{(0)}$ from $\hat{\boldsymbol{r}}_{\text{aux}}$ as $\hat{\boldsymbol{r}}_\pm^{(0)} = P_3\hat{\boldsymbol{r}}_{\text{aux}}$. The action of the approximate projection operator on the DAE (3.8) can expressed compactly as

$$\frac{\partial \hat{\boldsymbol{\phi}}'_\pm}{\partial x} = P_3\hat{\boldsymbol{r}}_{\text{aux}}, \tag{3.12a}$$

$$P_2\hat{\boldsymbol{r}}_{\text{aux}} = P_1 \begin{bmatrix} \tilde{A}_{\pm\pm}^{-1}[\tilde{L}_{\pm\pm}\hat{\boldsymbol{\phi}}'_\pm + \tilde{L}_{\pm 0}\hat{\boldsymbol{\phi}}'_0 + \hat{\boldsymbol{f}}_{\phi,\pm}] \\ \tilde{L}_{0\pm}\hat{\boldsymbol{\phi}}'_\pm + \tilde{L}_{00}\hat{\boldsymbol{\phi}}'_0 + \hat{\boldsymbol{f}}_{\phi,0} \end{bmatrix}, \tag{3.12b}$$

$$0 = \tilde{L}_{0\pm}\hat{\boldsymbol{\phi}}'_\pm + \tilde{L}_{00}\hat{\boldsymbol{\phi}}'_0 + \hat{\boldsymbol{f}}_{\phi,0}. \tag{3.12c}$$

3.1.4 Fully-discrete equations

We define $A^\ddagger, L^\ddagger \in \mathbb{R}^{(N_v+N_{\text{aux}})\times(N_v+N_{\text{aux}})}$ and $\hat{\boldsymbol{\phi}}^\ddagger, \hat{\boldsymbol{f}}_\phi^\ddagger \in \mathbb{C}^{N_v+N_{\text{aux}}}$ such that

$$A^\ddagger = \begin{bmatrix} I_{\pm\pm} & 0 & 0 \\ 0 & 0 & 0 \\ 0 & 0 & 0 \end{bmatrix}, \quad L^\ddagger = \begin{bmatrix} 0 & 0 & \Delta x P_3 \\ P_1 \begin{bmatrix} \tilde{A}_{\pm\pm}^{-1}L_{\pm\pm} \\ L_{0\pm} \end{bmatrix} & P_1 \begin{bmatrix} \tilde{A}_{\pm\pm}^{-1}L_{\pm 0} \\ L_{00} \end{bmatrix} & -P_2 \\ L_{0\pm} & L_{00} & 0 \end{bmatrix},$$

and

$$\hat{\boldsymbol{\phi}}^{\ddagger} = \begin{bmatrix} \boldsymbol{\phi}'_{\pm} \\ \boldsymbol{\phi}_0 \\ \boldsymbol{r}_{\text{aux}} \end{bmatrix}, \quad \hat{\boldsymbol{f}}_{\phi}^{\ddagger} = \begin{bmatrix} 0 \\ P_1 \begin{bmatrix} \tilde{A}_{\pm\pm}^{-1} \hat{\boldsymbol{f}}_{\phi,\pm} \\ \hat{\boldsymbol{f}}_{\phi,0} \end{bmatrix} \\ \hat{\boldsymbol{f}}_{\phi,0} \end{bmatrix}.$$

Then, following the previous work on linear OWNS (Rigas et al., 2017a; Kamal et al., 2020), we apply an s-order BDF scheme to obtain the linear OWNS equation

$$[c^{(0)} A^{\ddagger} - L^{\ddagger(k_x+1)}] \hat{\boldsymbol{\phi}}^{\ddagger(k_x+1)} = -\sum_{l_x=1}^{s-1} c^{(l_x)} A^{\ddagger} \hat{\boldsymbol{\phi}}^{\ddagger(k_x+1-l_x)} + \hat{\boldsymbol{f}}_{\phi}^{\ddagger(k_x+1)}, \tag{3.13}$$

for $k_x = 1, \ldots, N_x$, where N_x denotes the number of streamwise stations, while s denotes the order of the BDF scheme and $c^{(l_x)}$ for $l_x = 0, \ldots, s-1$ denotes the marching coefficients.

3.1.5 Streamwise diffusion terms

Following discretization in the wall-normal direction and trasnformation to characteristic variables, our streamwise diffusion terms become

$$\hat{\boldsymbol{f}}_{\phi,\text{viscous}} = -\tilde{B}_{xx} \frac{\partial^2 \hat{\boldsymbol{\phi}}}{\partial x^2} - \tilde{B}_x \frac{\partial \hat{\boldsymbol{\phi}}}{\partial x} - \tilde{B} \hat{\boldsymbol{\phi}},$$

for $\tilde{B}_{xx} = T B_{xx} T^{-1}$, $\tilde{B}_x = 2T B_{xx} \frac{\partial T^{-1}}{\partial x} + T[B_x + B_{xy} D + i\beta B_{xz}] T^{-1}$, and $\tilde{B} = T B_{xx} \frac{\partial^2 T^{-1}}{\partial x^2} + T[B_x + B_{xy} D + i\beta B_{xz}] \frac{\partial T^{-1}}{\partial x}$. We discretize the second-derivative using a second-order backward difference, while we discretize the first-derivative using the BDF scheme to obtain

$$\hat{\boldsymbol{f}}_{\phi,\text{viscous}}^{(k+1)} = -\tilde{B}_{xx} \frac{\hat{\boldsymbol{\phi}}^{(k+1)} - 2\hat{\boldsymbol{\phi}}^{(k)} + \hat{\boldsymbol{\phi}}^{(k-1)}}{(\Delta x)^2} - \Big(\sum_{l=0}^{s-1} c^{(l)} \tilde{B}_x \hat{\boldsymbol{\phi}}^{(k+1-l)} \Big) - \tilde{B} \hat{\boldsymbol{\phi}}^{(k+1)},$$

and we add this term back into the fully-discrete OWNS equations (3.13).

3.2 Nonlinear OWNS

Whereas infinitesimal disturbances (in the linear case) evolve independently from each other so that each Fourier mode can be considered separately, finite amplitude disturbances (in the nonlinear case) are coupled through the nonlinear term. Since it is not feasible to consider an infinite number of Fourier modes, we truncate the Fourier (3.2) series

$$\boldsymbol{q}'(x, y, z, t) = \sum_{m=-M}^{M} \sum_{n=-N}^{N} \hat{\boldsymbol{q}}_{mn} e^{i(n\beta z - m\omega t)}, \tag{3.14}$$

resulting in $(2M+1)\times(2N+1)$ Fourier modes. However, we require that $\boldsymbol{q}'$ be real-valued, which yields the constraint $\hat{q}_{mn} = \overline{\hat{q}_{-mn}}$, so that we need only track $(M+1)\times(2N+1)$ Fourier modes. We can additionally introduce a spanwise symmetry condition, as described in Section 3.2.5, which further reduces the number of modes to $(M+1)\times(N+1)$.

The nonlinear terms in primitive variables, $F(\boldsymbol{q}')$, are defined in (A.4), and we transform them to primitive variables in a way that mimics the transformation of the linear terms, to obtain the nonlinear terms in characteristic variables, $\tilde{F}(\boldsymbol{\phi})$. We use our assumption of periodicity to obtain the Fourier series

$$\tilde{L}(\bar{\boldsymbol{q}})\boldsymbol{\phi} = \sum_{m=-M}^{M}\sum_{n=-N}^{N} \hat{L}_{mn}\hat{\boldsymbol{\phi}}_{mn}e^{i(n\beta z - m\omega t)}, \tag{3.15}$$

$$\tilde{\boldsymbol{F}}(\boldsymbol{\phi}) = \sum_{m=-M}^{M}\sum_{n=-N}^{N} \hat{\boldsymbol{F}}_{mn}(\boldsymbol{\phi})e^{i(n\beta z - m\omega t)} \tag{3.16}$$

$$\tilde{\boldsymbol{f}}_{\phi} = \sum_{m=-M}^{M}\sum_{n=-N}^{N} \hat{\boldsymbol{f}}_{\phi,mn}e^{i(n\beta z - m\omega t)}. \tag{3.17}$$

Note that $\tilde{f}_{\phi}$ is the forcing function in characteristic variables defined in (3.6c). The Fourier modes are mutually orthogonal, yielding the following system of equations:

$$\tilde{A}\frac{\partial\hat{\boldsymbol{\phi}}_{mn}}{\partial x} = \hat{L}_{mn}\hat{\boldsymbol{\phi}}_{mn} + \hat{\boldsymbol{F}}_{mn}(\boldsymbol{\phi}) + \hat{\boldsymbol{f}}_{\phi,mn}, \quad \forall m \in \mathbb{Z}_M, \quad \forall n \in \mathbb{Z}_N, \tag{3.18}$$

for $\mathbb{Z}_M \equiv \{x \in \mathbb{Z} | -M \le x \le M\}$ and $\mathbb{Z}_N \equiv \{x \in \mathbb{Z} | -N \le x \le N\}$, where $\mathbb{Z}$ is the set of all integers. We follow a procedure that mimics the linear OWNS approach to obtain

$$\frac{\partial\boldsymbol{\phi}'_{\pm,mn}}{\partial x} = \hat{P}_{mn}[\hat{M}_{mn}\hat{\boldsymbol{\phi}}'_{\pm,mn} + \hat{\boldsymbol{g}}_{mn}(P\boldsymbol{\phi}'_{\pm})], \quad \forall m \in \mathbb{Z}_M, \quad \forall n \in \mathbb{Z}_N. \tag{3.19}$$

In the linear case, P and M commute so that two one-way parabolic equations can be solved to recover the full elliptic solution (Towne et al., 2022). However, this property does not apply in the nonlinear case because the P does not commute with the nonlinear term ($P\boldsymbol{g}(\boldsymbol{\phi}_{\pm}) \neq P\boldsymbol{g}(P\boldsymbol{\phi}_{\pm})$ in general), so that (3.19) removes the upstream effect, $\boldsymbol{\phi}''$, from the nonlinear term, and when we sum the upstream- and downstream-going equations together, we do not recover the elliptic equation. This is a reasonable choice for convective instabilities, where the disturbances travel primarily in one direction, and we verify *a posteriori* that we match closely DNS results in the literature.

3.2.1 Fully-discrete equations

We define $L^{\ddagger}_{mn} \in \mathbb{R}^{(N_v+N_{\text{aux}})\times(N_v+N_{\text{aux}})}$ and $\hat{\boldsymbol{\phi}}^{\ddagger}_{mn}, \hat{\boldsymbol{f}}^{\ddagger}_{mn,\phi} \in \mathbb{C}^{N_v+N_{\text{aux}}}$, as in the linear case, for all $m \in \mathbb{Z}_M$ and $n \in \mathbb{Z}_N$, and further introduce the nonlinear term $\hat{\boldsymbol{F}}^{\ddagger}_{mn} \in \mathbb{C}^{N_v+N_{\text{aux}}}$ such that it mimics the definition of the forcing function $\hat{\boldsymbol{f}}^{\ddagger}_{mn,\phi}$. Then we discretize the first-derivatives in both the linear and nonlinear terms using the BDF scheme yielding the fully-discrete nonlinear system of equations

$$\sum_{l_x=0}^{s-1} c^{(l_x)} A^{\ddagger} \hat{\boldsymbol{\phi}}^{\ddagger(k_x+1-l)}_{mn} = \hat{L}^{\ddagger(k_x+1)}_{mn} \hat{\boldsymbol{\phi}}^{\ddagger(k_x+1)}_{mn} + \hat{\boldsymbol{F}}^{\ddagger(k_x+1)}_{mn} + \hat{\boldsymbol{f}}^{\ddagger(k_x+1)}_{\phi,mn}, \tag{3.20}$$

for $m \in \mathbb{Z}_M$, $n \in \mathbb{Z}_N$, and $k_x = 1, \ldots, N_x$.

3.2.2 Pseudo-spectral method

We employ a pseudo-spectral method whereby we solve our equations in Fourier space, while we evaluate the nonlinear terms in physical space. Given the Fourier coefficients $\hat{\boldsymbol{\phi}}_{mn}$ for $m = 0, \ldots, 2M$ and $n = 0, \ldots, N$, we can use the inverse discrete Fourier transform (iDFT) to compute the solution in physical space as

$$\boldsymbol{\phi}_{kl} = \frac{1}{2M+1} \frac{1}{2N+1} \sum_{m=0}^{2M} \sum_{n=0}^{2N} \hat{\boldsymbol{\phi}}_{mn} e^{i2\pi km/(2M+1)} e^{i2\pi ln/(2N+1)}. \tag{3.21}$$

for discrete times and spanwise locations associated with indices $k = 0, \ldots, 2M$ and $l = 0, \ldots, 2N$, respectively. Then, we can evaluate the nonlinear terms in physical space, $\tilde{\boldsymbol{F}}_{mn} = \tilde{\boldsymbol{F}}(\boldsymbol{\phi}_{mn})$, and employ the discrete Fourier transform (DFT) to compute the Fourier components of the nonlinear terms as

$$\hat{\boldsymbol{F}}_{kl} = \sum_{m=0}^{2M} \sum_{n=0}^{2N} \tilde{\boldsymbol{F}}_{mn} e^{-i2\pi mk/(2M+1)} e^{-i2\pi nl/(2N+1)}, \tag{3.22}$$

for $k = 0, \ldots, 2M$ and $l = 0, \ldots, 2N$. In practice, the DFT and iDFT are performed using fast Fourier transform (FFT) libraries.

3.2.3 Nonlinear solution procedure and computational cost

We must ensure that the residual

$$\hat{\boldsymbol{r}}^{\ddagger(k_x+1)}_{mn} = \sum_{l_x=0}^{s-1} c^{(l_x)} A^{\ddagger} \hat{\boldsymbol{\phi}}^{\ddagger(k_x+1-l)}_{mn} - \hat{L}^{\ddagger(k_x+1)}_{mn} \hat{\boldsymbol{\phi}}^{\ddagger(k_x+1)}_{mn} - \hat{\boldsymbol{F}}^{\ddagger(k_x+1)}_{mn} - \hat{\boldsymbol{f}}^{\ddagger(k_x+1)}_{\phi,mn} \tag{3.23}$$

is converged for every Fourier mode ($m \in \mathbb{Z}_M$ and $n \in \mathbb{Z}_N$) at every step of the march ($k_x = 1, \ldots, N_x$). We will use Newton's method to iteratively force the norm

of the residual to zero in both an absolute and relative sense to a tolerance of 10^{-10}:

$$\|\hat{\boldsymbol{r}}_{mn}^{\ddagger(k_x+1)}\| < 10^{-10}, \quad \frac{\|\hat{\boldsymbol{r}}_{mn}^{\ddagger(k_x+1)}\|}{\sqrt{\sum_{m=-M}^{M}\sum_{n=-N}^{N}\|\hat{\boldsymbol{\phi}}_{mn}^{(k_x+1)}\|^2}} < 10^{-10}.$$

We concatenate the residual and solution vectors as

$$R_m^{(k_x+1)} = \begin{bmatrix} \hat{\boldsymbol{r}}_{m,-(N-1)}^{\ddagger(k_x+1)} \\ \vdots \\ \hat{\boldsymbol{r}}_{m,N-1}^{\ddagger(k_x+1)} \end{bmatrix}, \quad \Phi_m^{(k_x+1)} = \begin{bmatrix} \hat{\boldsymbol{\phi}}_{m,-(N-1)}^{\ddagger(k_x+1)} \\ \vdots \\ \hat{\boldsymbol{\phi}}_{m,N-1}^{\ddagger(k_x+1)} \end{bmatrix}, \quad m = 0, \ldots, 2M, \tag{3.24}$$

and

$$R^{(k_x+1)} = \begin{bmatrix} R_0^{(k_x+1)} \\ \vdots \\ R_{2M}^{(k_x+1)} \end{bmatrix}, \quad \Phi^{(k_x+1)} = \begin{bmatrix} \Phi_0^{(k_x+1)} \\ \vdots \\ \Phi_{2M}^{(k_x+1)} \end{bmatrix}. \tag{3.25}$$

In 2D with $M = 1$ we obtain

$$R^{(k+1)} = \begin{bmatrix} \hat{\boldsymbol{r}}_0^{\ddagger(k+1)} \\ \hat{\boldsymbol{r}}_1^{\ddagger(k+1)} \\ \hat{\boldsymbol{r}}_2^{\ddagger(k+1)} \end{bmatrix} = \begin{bmatrix} \hat{\boldsymbol{r}}_0^{\ddagger(k+1)} \\ \hat{\boldsymbol{r}}_1^{\ddagger(k+1)} \\ \hline \hat{\boldsymbol{r}}_1^{\ddagger(k+1)} \end{bmatrix}, \quad \Phi^{(k+1)} = \begin{bmatrix} \hat{\boldsymbol{\phi}}_0^{\ddagger(k+1)} \\ \hat{\boldsymbol{\phi}}_1^{\ddagger(k+1)} \\ \hat{\boldsymbol{\phi}}_2^{\ddagger(k+1)} \end{bmatrix} = \begin{bmatrix} \hat{\boldsymbol{\phi}}_0^{\ddagger(k+1)} \\ \hat{\boldsymbol{\phi}}_1^{\ddagger(k+1)} \\ \hline \hat{\boldsymbol{\phi}}_1^{\ddagger(k+1)} \end{bmatrix}, \tag{3.26}$$

where we have used that

$$\hat{\boldsymbol{r}}_m^{\ddagger(k+1)} = \overline{\hat{\boldsymbol{r}}_{2M+1-m}^{\ddagger(k+1)}}, \quad \hat{\boldsymbol{\phi}}_m^{\ddagger(k+1)} = \overline{\hat{\boldsymbol{\phi}}_{2M+1-m}^{\ddagger(k+1)}}, \quad m > M.$$

Using Newton's method, we obtain the Newton iterations

$$\frac{\partial R^{(k+1),\sigma}}{\partial \Phi^{(k+1),\sigma}} \Delta\Phi^{(k+1),\sigma+1} = -R^{(k+1),\sigma}, \quad \sigma = 0, 1, \ldots, \sigma_{(k+1)}, \tag{3.27}$$

where we take $\Phi^{(k+1),0} = \Phi^{(k),\sigma_{(k)}}$ for $\sigma_{(k)}$ denoting the number of Newton iterations at streamwise station k, while the Jacobian $\partial R^{(k+1),\sigma}/\partial\Phi^{(k+1),\sigma}$ is as defined in (F.6). Neglecting matrix blocks that are not on the diagonal, and writing the expression for 3D disturbances, we obtain the Newton iterations

$$[c^{(0)}A^{\ddagger} - \hat{L}_{mn}^{\ddagger(k+1),\sigma} + \hat{J}_{00}^{\ddagger(k+1),\sigma}]\Delta\hat{\boldsymbol{\phi}}_{mn}^{\ddagger(k+1),\sigma+1} = -\hat{\boldsymbol{r}}_{mn}^{\ddagger(k+1),\sigma}, \tag{3.28}$$

for $m = -M, \ldots, M$, $n = -N, \ldots, N$, and $\sigma = 0, 1, \ldots, \sigma_{(k+1)}$. If we neglect $J_{00}^{\ddagger(k+1),\sigma}$, then we obtain

$$[c^{(0)}A^{\ddagger} - \hat{L}_{mn}^{\ddagger(k+1),\sigma}]\Delta\hat{\boldsymbol{\phi}}_{mn}^{\ddagger(k+1),\sigma+1} = -\hat{\boldsymbol{r}}_{mn}^{\ddagger(k+1),\sigma}, \tag{3.29}$$

for $m = -M, \ldots, M$, $n = -N, \ldots, N$, and $\sigma = 0, 1, \ldots, \sigma_{(k+1)}$. To solve (3.28) or (3.29), we mimic the NPSE solution procedure (Bertolotti, 1991; Chang et al.,

1993; Day, 1999): we take the lower-upper (LU) decomposition of $[c^{(0)}A^{\ddagger} - \hat{L}_{mn}^{\ddagger(k+1)}]$ to solve for $\Delta\hat{\boldsymbol{\phi}}_{mn}^{\ddagger(k+1),\sigma+1}$, then we update the nonlinear term, and repeat until the residual is converged. We typically prefer solving (3.28) over (3.29) because it reduces the number of iterations to convergence, without increasing the computational cost. Alternatively, if we accept a larger computational cost, then we can further reduce the number of iterations by solving (3.27).

The linear OWNS system (3.13) comprises $N_v + N_{\text{aux}} = N_v + (2N_v + 1)N_b$ equations, where N_v scales with N_y, so that the computational cost to solve this system using a direct multifrontal solver (LU decomposition) scales as $O(N_y^a N_b^a)$, where a is a problem dependent coefficient that depends on the sparsity pattern. Theoretically, $1 < a \leq 3$ and we typically observe $a \approx 1.5$ for 2D problems and $a \approx 2$ for 3D ones, see (Towne et al., 2022) for further details. The cost to integrate over N_x stations is then $O(N_x N_y^a N_b^a)$, while a global method entails a cost of $O(N_x^a N_y^a)$, so that OWNS is more efficient for $N_b \ll N_x$. The nonlinear OWNS system (3.20) comprises $(M + 1) \times (2N + 1) \times (N_v + N_{\text{aux}})$ equations, and can be solved using Newton's method (3.27), which entails a cost of $O(M^a N^a N_y^a N_b^a)$. However, this cost can be reduced by instead solving (3.28) or (3.29), since we can perform the LU decomposition of $[c^{(0)}A^{\ddagger} - \hat{L}_{mn}^{\ddagger(k+1)}]$ separately for each Fourier mode, yielding a cost of $O(MNN_y^a N_b^a)$. Therefore, the cost to integrate the NOWNS equations is $O(N_x MNN_y^a N_b^3)$ using (3.28) or (3.29), while it increases to $O(N_x M^a N^a N_y^a N_b^3)$ for Newton's method (3.27), as compared to the cost $O(N_x^a M^a N^a N_y^a)$ for nonlinear global methods.

Although (3.28) and (3.29) entail a lower computational cost, these methods fail for strong nonlinearities and we must instead employ Newton's method (3.27). In practice we implement a hybrid approach whereby we first solve (3.28) to harness its reduced computational cost, and then if more than $O(100)$ iterations have elapsed, we switch to Newton's method to harness its better convergence properties. We compare the performance of these three methods in Appendix G.3.

To reduce the computational cost of Newton's method, we re-use the LU factors from the first iteration as a pre-conditioner for the Generalized Minimal Residual Method (GMRES), and we note that a similar procedure was performed for linear OWNS in (Araya et al., 2022). We also tested the block-Jacobi relaxation method, which entails a cost of $O(MNN_y^a N_b^a)$, and although we found this approach converged quickly in the early stages of the march, it failed as the nonlinearity grew stronger and we did not pursue relaxation methods further.

3.2.4 Special treatment of the zero-frequency modes

We have three options for obtaining a stable march for the zero-frequency modes, as depicted in table 3.1. In the first approach, which mimics how the zero-frequency modes are handled by NPSE (Chang et al., 1993; Day, 1999), we neglect the streamwise pressure gradient, $\partial p_{0n}/\partial x$, and the streamwise diffusion terms, $\partial^2 q_{0n}/\partial x^2$, associated with the zero-frequency modes. However, in general we would prefer to avoid neglecting terms, and to instead parabolize these equations using the OWNS approach. In the second approach, we include the streamwise diffusion terms (but exclude the streamwise pressure gradient) associated with the zero-frequency modes, and parabolize the equations for all modes using OWNS. This approach yields a stable spatial march that agrees well with DNS, but offers no advantages over the first approach: for all of the cases examined in this paper, neglecting the streamwise diffusion terms associated with the zero-frequency modes does not change substantially the results of the NOWNS calculation. In the third approach, we include both the streamwise diffusion terms and the streamwise pressure gradient associated with the zero-frequency modes. Although the OWNS approach yields a stable spatial march, we have found that this approach produces inferior comparisons to DNS solutions from the literature, as discussed in Appendix G.2.

We are applying NOWNS to boundary-layer flows where we wish to maintain zero mean streamwise pressure gradient. The base flow has zero streamwise pressure gradient, while the corrected mean flow will have zero streamwise pressure gradient if $\partial p_{0n}/\partial x = 0$. In general, we will have $\partial p_{0n}/\partial x \neq 0$, but as long as it is small, the streamwise pressure gradient of the corrected mean flow will be nearly zero. It is possible that neglecting $\partial p_{0n}/\partial x$ leads to better agreement with the zero mean streamwise pressure gradient condition, which is why we observe better agreement with DNS. We further note that for flows with non-zero streamwise pressure gradients, we will likely also wish to neglect $\partial p_{0n}/\partial x = 0$ since the base flow will have the desired streamwise pressure gradient.

In summary, including the streamwise pressure gradient for the zero-frequency modes worsens agreement with DNS, while including the streamwise diffusion terms for the zero-frequency modes has nearly no impact on the solution. Since neglecting these terms is more computationally efficient while still providing excellent agreement with DNS, we recommend that these terms be neglected.

	Include $\partial p_{0n}/\partial x$?	Include $\partial^2 q_{0n}/\partial x^2$?	Parabolized using OWNS?	Agreement with DNS?
1	No	No	No	Yes
2	No	Yes	Yes	Yes
3	Yes	Yes	Yes	No

Table 3.1: Three approaches to parabolizing the zero-frequency modes

3.2.5 Spanwise symmetry

If the disturbances are symmetric, then we can enforce a symmetry condition to reduce the number of equations from $(M+1)\times(2N+1)$ to $(M+1)\times(N+1)$. All variables have even-symmetry ($\hat{v}'_{m,-n} = \hat{v}'_{m,n}$, $\hat{u}'_{m,-n} = \hat{u}'_{m,n}$, $\hat{v}'_{m,-n} = \hat{v}'_{m,n}$, $\hat{p}'_{m,-n} = \hat{p}'_{m,n}$), with the exception of the w-velocity which has odd-symmetry ($\hat{w}'_{m,-n} = -\hat{w}'_{m,n}$).

3.2.6 Boundary conditions

At the wall, we impose no-slip isothermal boundary conditions ($u' = v' = w' = T' = 0$) and solve for the specific volume, v', using the (nonlinear) continuity equation. At the far-field boundary, we impose 1D (in y) inviscid Thompson characteristic boundary conditions to minimize spurious numerical reflections (Thompson, 1987), which we implement using the linearized boundary-layer flow equations.

Some previous work on NPSE has used similar characteristic far-field boundary conditions (Day, 1999). Chang et al. (1993) used the far-field boundary condition $\hat{\boldsymbol{q}}'_{mn}(y_{\max}) = 0$ for $m, n \neq 0$. As the boundary layer must be allowed to grow in the wall-normal direction (due to nonlinear interactions), they used $\partial \hat{v}'_{00}/\partial y = 0$ at $y_{\max}$ for the mean-flow distortion (MFD). The characteristic far-field boundary conditions are advantageous because they allow us to use the same boundary conditions for all Fouriers modes, instead of handling the MFD as a separate case.

3.2.7 Effects of the mean-flow distortion

In NOWNS, the disturbances interact to excite the MFD, so that the corrected mean flow, $\bar{\boldsymbol{q}} + \hat{\boldsymbol{q}}_{00}$, differs from the baseflow, $\bar{\boldsymbol{q}}$. We have experimented with linearizing about both the baseflow and the corrected mean flow and found that it does not have a large impact on the NOWNS calculation, as discussed in Appendix G.4. Linearizing about the corrected mean flow increases the computational cost of NOWNS because the projection operators change between iterations, since the MFD changes, so the LU factorization must be updated. On the other hand, linearizing about the baseflow allows us to use the same LU factorization at each iteration because the baseflow is not affected by changes in the MFD. Since it is more computationally efficient to

linearize only about the baseflow, we choose this approach moving forward.

3.2.8 Recursion parameters

The choice of recursion parameters is described in Sleeman et al. (2024b), and matches the recursion parameters used by Rigas et al. (2017a), which are based on the recursion parameters originally developed by Towne and Colonius (2015). We briefly discuss our strategy for selecting the recursion parameters when $\omega = 0$ in Appendix H.

3.2.9 Modeling errors

NOWNS removes upstream effects, which introduces a modeling error, since the real flow does allow waves to propagate in the upstream direction. We discuss this modeling error and its effect on the NOWNS methodology in more detail in Section 5.4.2.

3.3 Validation

We validate NOWNS by applying it to 2D and 3D Blasius boundary layer flows, where the base flows are generated following the procedure outlined in Appendix B, for which there are existing DNS and NPSE results in the literature. We choose a Mach number of $\mathrm{Ma}_\infty = 0.1$ to study flows near the incompressible limit. We refer to modes according to their temporal frequency and their spanwise wave number as (m, n), where m refers to the frequency $\omega_m = m\omega$ and n refers to the spanwise wave number $\beta_n = n\beta$. To be consistent with previous literature, we measure the amplitude of disturbances as

$$u'^{(m,n)}_{\max}(x) = c_{m,n} \max_y |u'_{m,n}(x, y)|, \tag{3.30a}$$

for

$$c_{m,n} = \begin{cases} 1 & m = n = 0, \\ \sqrt{2} & m = 0, n \neq 0;\ n = 0, m \neq 0, \\ 2 & \text{otherwise.} \end{cases} \tag{3.30b}$$

3.3.1 2D evolution of a Tollmien-Schlichting wave

We consider the test case developed by Bertolotti et al. (1992) which has been widely used in the literature as a validation case for NPSE (Joslin et al., 1991; Joslin et al., 1993; Paredes et al., 2015). This case examines the evolution of a Tollmien-Schlichting (TS) wave excited at the inlet at a frequency $F = 86\times10^{-6}$ and amplitude

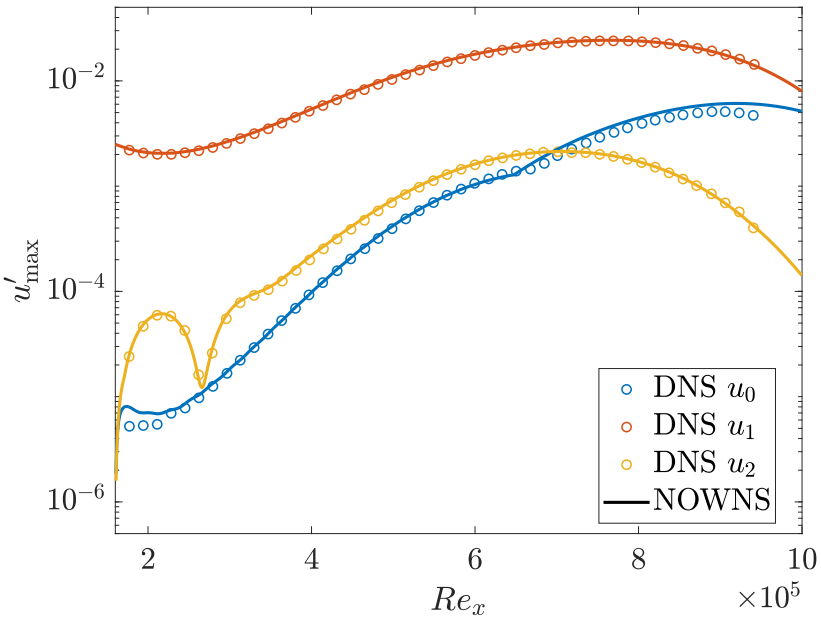

Figure 3.1: Amplitude of u' v.s. streamwise coordinate, Re_x, for 2D evolution of TS wave.

$u'^{(1)}_{\max}(x_0) = 0.25\%$. All other Fourier components initially have zero-amplitude and are generated through nonlinear interactions with the TS wave. The grid extends over the domain $Re_x \in [1.6 \times 10^5, 10^6]$ and $y \in [0, 75]$ with 4000 stations evenly spaced in x and 150 grid points in y, with the majority of the grid points clustered towards the wall, while the Fourier series is truncated at $M = 5$ temporal modes.

Figure 3.1 compares NOWNS to DNS and NPSE for $u'^{(m,n)}_{\max}(x)$, while the u- and v-velocity profiles for the MFD and TS waves are shown in Figure 3.2. Excellent agreement is obtained; the discrepancy for the MFD of v can be attributed to the Dirichlet boundary conditions used in the DNS.

3.3.2 3D oblique-wave breakdown

Next we consider the oblique-wave breakdown case studied by Joslin et al. (1993), where transition is initiated by two oblique waves with opposite wave angle. They defined two cases–with small and large initial amplitude. In this section, for validation purposes, we consider the small amplitude case for which NPSE was previously successful.

Oblique-wave breakdown has also been studied using both experiment and spatial DNS by Berlin et al. (1999), while it was studied using NPSE for compressible flows by Chang and Malik (1994). We further note that whereas fundamental and

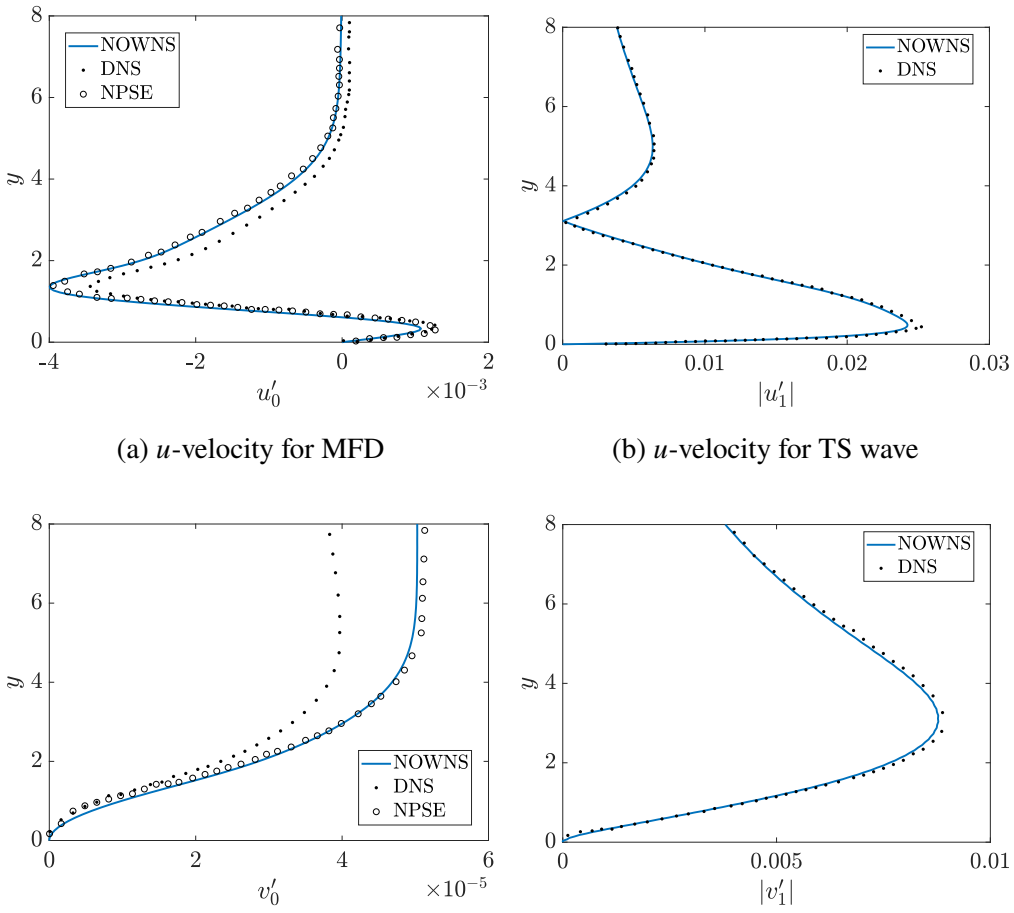

(a) u-velocity for MFD

(b) u-velocity for TS wave

(c) v-velocity for MFD

(d) v-velocity for TS wave

Figure 3.2: u-and v-velocity profiles at streamwise coordinate $Re_x = 7.80 \times 10^5$ for 2D evolution of TS wave.

subharmonic transition can be studied using Herbert's secondary stability theory (Herbert, 1988), no such theory exists for oblique-wave breakdown, so that either experiment or numerical simulation is necessary to study this transition scenario (Joslin et al., 1993; Berlin et al., 1999).

The oblique waves have amplitude $u'^{(1,1)}_{\max}(x_0) = \sqrt{2} \times 10^{-3}$ at the inlet at a frequency $F = 86 \times 10^{-6}$ and spanwise wavenumber $b = 2/9 \times 10^{-3}$, while the grid extends over the domain $Re_x \in [2.74 \times 10^5, 6.08 \times 10^5]$ and $y \in [0, 75]$ with 2,000 stations evenly spaced in x and 150 grid points in y, while the Fourier series is truncated at $M = 3$ and $N = 4$. Figure 3.3 compares NOWNS to DNS and NPSE for $u'^{(m,n)}_{\max}(x)$, while Figure 3.4 compares the u-velocity profiles at $Re_x = 4.69 \times 10^5$; we see that we have excellent agreement between the DNS and NOWNS results for all modes.

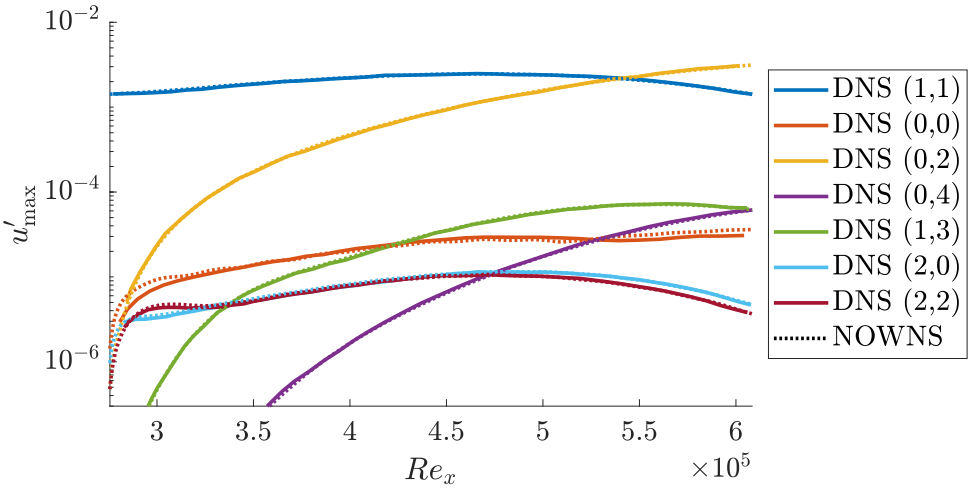

Figure 3.3: Amplitude of u' v.s. streamwise coordinate, Re_x, for the small-amplitude oblique-wave breakdown case at frequency $F = 86 \times 10^{-6}$, spanwise wavenumber $b = 2/9 \times 10^{-3}$, with initial amplitude of $u'^{(1,1)}_{\max}(x_0) = \sqrt{2} \times 10^{-3}$.

3.4 Advantages of the NOWNS procedure

In this section, we apply NOWNS in three scenarios where NPSE is known to break down, to demonstrate that NOWNS can succeed where NPSE fails.

3.4.1 High amplitude evolution of TS wave

It is well-known that NPSE can fail for sufficiently strong nonlinearities (Day, 1999; Towne et al., 2019). Here we consider a 2D test case from Scholten et al. (2024), where we modify the validation case discussed in Section 3.3.1, such that we march over the domain $Re_x \in [1.6 \times 10^5, 8.59 \times 10^5]$ with 2663 stations evenly spaced in x, while the wall-normal domain remains the same as before, and the Fourier series truncate at $M = 10$ temporal modes. Scholten et al. (2024) compute a high-fidelity solution using a harmonic Navier-Stokes equation (HNSE) solver, and demonstrate that NPSE agrees with HNSE with an inlet amplitude of $u'^{(1)}_{\max}(x_0) = 0.4\%$, but that the NPSE march fails. In Figure Scholten et al. (2024), we plot the NOWNS amplitudes against those from HNSE and demonstrate that NOWNS marches farther than NPSE, while still being accurate, but that it too fails (by fail, we mean that the Newton solver fails to converge). This highlights that NOWNS can march farther than NPSE, while still being accurate, and that the failure of NPSE may not be related to its minimum step-size requirement or the regularization techniques it uses to suppress the upstream-going waves. As discussed in 3.2.3, the quasi-Newton method is more computationally efficient than the full Newton's method, but takes

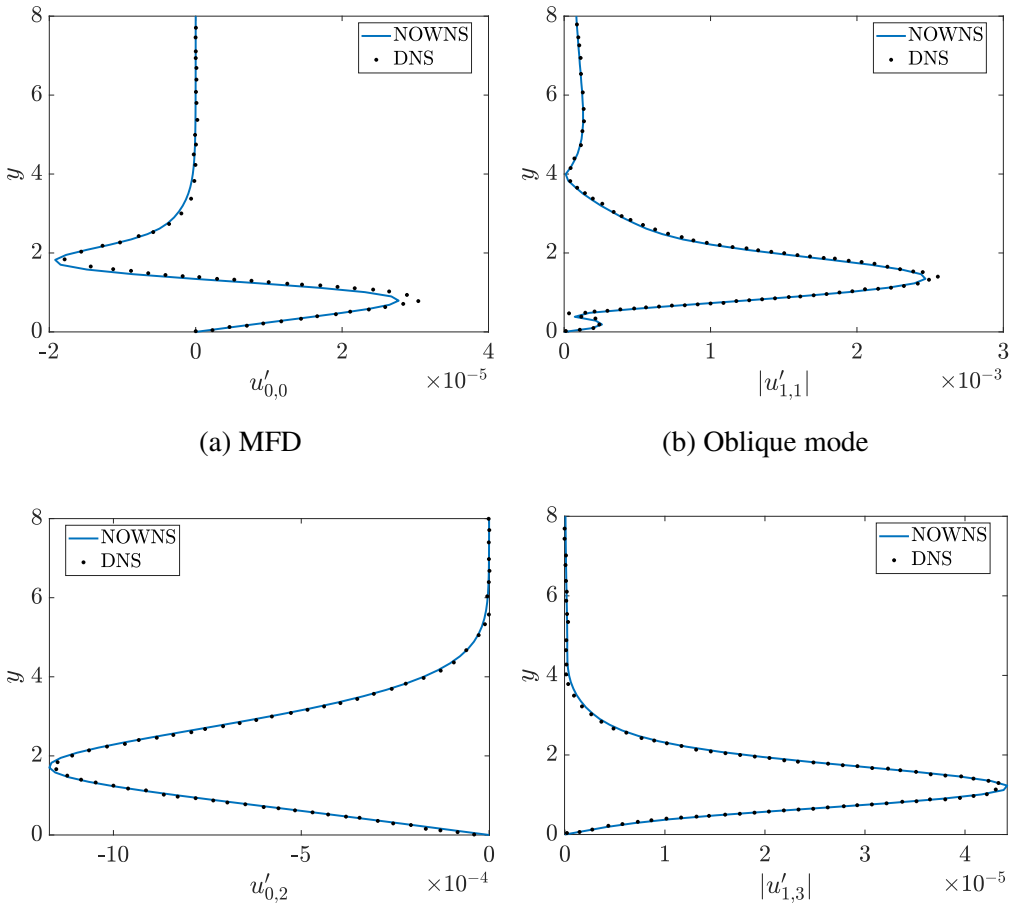

(a) MFD

(b) Oblique mode

(c) Vortex mode

(d) First harmonic in z

Figure 3.4: u-velocity profiles at streamwise coordinate $Re_x = 4.69 \times 10^5$ for small-amplitude oblique-wave breakdown.

more iterations to converge. In addition, the full Newton's method is more likely to converge for stronger nonlinearities. In Figure 3.5, we indicate where each of the the quasi-Newton and full Newton methods fail. Even without employing the full Newton's method, NOWNS is able to march farther downstream than NPSE.

3.4.2 High amplitude oblique-wave breakdown

Here we apply NOWNS the high amplitude oblique-wave breakdown case studied by Joslin et al. (1993). We modify the setup of Section 3.3.2 by increasing the amplitude of the oblique wave at the inlet by a factor of 10 to $u'^{(1,1)}_{\max}(x_0) = \sqrt{(2)} \times 10^{-2}$, while we change the streamwise domain so that it comprises 2,000 grid points over the domain $Re_x \in [2.73529 \times 10^5, 4.9 \times 10^5]$, and the Fourier series are truncated at $M = N = 7$. We plot the amplitudes of the u-velocity as a function of streamwise station in Figure 3.6. First we note that we have excellent agreement between the

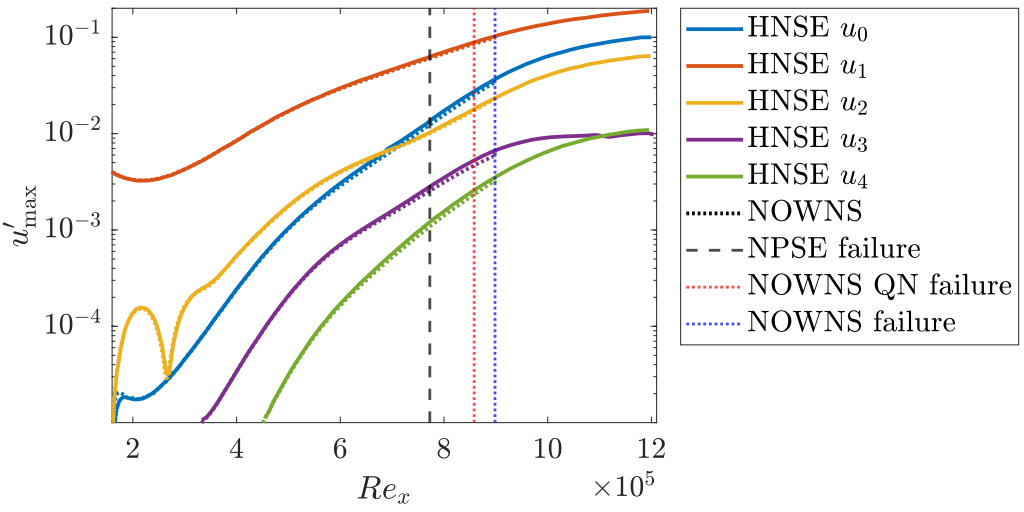

Figure 3.5: Amplitude of u' v.s. streamwise coordinate, Re_x, for 2D evolution of TS wave with $u'^{(1)}_{\max}(x_0) = 0.4\%$.

amplitudes predicted by NOWNS, NPSE, and DNS for the early stages of transition. However, NPSE begins to fail towards the end of the domain, while NOWNS is able to march all the way to the end of the DNS calculation. The DNS calculation is under-resolved near the end of the domain (Joslin et al., 1993), which may explain the discrepancy between the DNS and NOWNS calculations. We further note that although the oblique-wave, $(1, 1)$, is initially the dominant instability, it is rapidly overtaken by the vortex mode, $(0, 2)$, leading to streaks, which we observe in the contour plots of the u-velocity ($u = \bar{u} + u'$), shown Figure 3.7. The maximum amplitude of the oblique-wave occurs at $y = 2.55$ (Figure 3.7a), while the maximum amplitude of the vortex mode occurs at $y = 1.31$ (Figure 3.7b). We also note that the QN solver fails before the NPSE solver. However, the NPSE calculation becomes inaccurate earlier than the QN solver fails.

3.4.3 Low amplitude oblique-wave breakdown with random noise

Here we demonstrate for the low amplitude oblique wave breakdown case of Section 3.3.2 that NOWNS is robust to random noise applied to the inlet boundary condition. Given the eigenfunction from the locally parallel linear stability theory, $\boldsymbol{q}_{\text{LST}}$, we add random noise, $\boldsymbol{q}_{\text{noise}}$, to obtain the inlet condition $\boldsymbol{q}_{\text{LST}} + \varepsilon\tilde{\boldsymbol{q}}_{\text{noise}}$. We choose complex random noise such that

$$\tilde{\boldsymbol{q}}_{\text{noise}} = \tilde{\boldsymbol{q}}_{\text{noise},r} + i\tilde{\boldsymbol{q}}_{\text{noise},i}, \quad \tilde{\boldsymbol{q}}_{\text{noise},r}, \tilde{\boldsymbol{q}}_{\text{noise},i} \sim \mathcal{U}_{[0,1]},$$

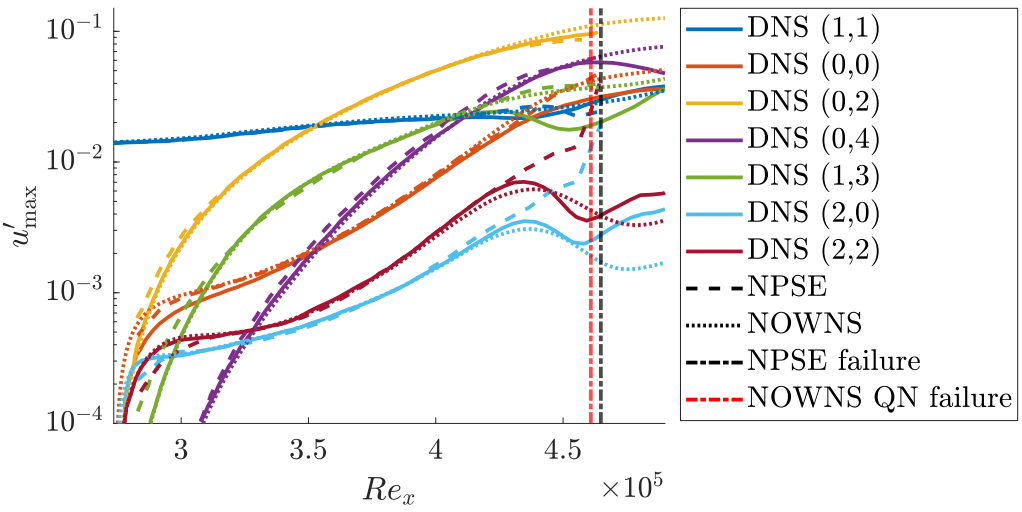

Figure 3.6: Amplitude of u' v.s. streamwise coordinate, Re_x, for high amplitude oblique-wave breakdown.

where $\mathcal{U}_{[a,b]}$ represents the uniform distribution over the interval $[a, b]$. We then normalize the noise to obtain q_{noise}, such that the maximum amplitude of the u-velocity noise is equal to the free-stream u-velocity, U_∞. We recall that the amplitude of $\boldsymbol{q}_{\text{LST}}$ is $\sqrt{2} \times 10^{-3}$, and we choose $\varepsilon = \sqrt{2} \times 10^{-5}$. In Figure 3.8, we plot the profile of the u- and v-velocities, as well as the thermodynamic variables. We see that the random noise has a relatively small effect on the u-velocity, and a slightly more pronounced effect on the v-velocity, while it has a larger impact on the thermodynamic variables. Like the u-velocity profile, the random noise has a relatively small effect on the w-velocity profile, so we omit this plot.

The NOWNS march succeeds even if we introduce large disturbances to the velocity fields, but the u' amplitudes differ substantially from the noise-less case due to the large perturbations. Therefore, we instead introduce relatively large random disturbances to the thermodynamic variables, and relatively small ones to the velocity field. In Figure 3.9, we see that the amplitudes predicted by NOWNS for the noisy inlet condition agree closely with those without noise. We also see that although NPSE initially is able to accurately predict the evolution of the u-velocity amplitudes, it eventually becomes inaccurate (especially for $u'_{(0,0)}$ and $u'_{(1,1)}$) before failing. We also plot the contours of the real part of the u- and v-velocities of the oblique wave, with and without noise in Figure 3.10. We see that despite the noisy inlet condition, NOWNS evolves the u-velocity of the oblique wave such that it matches closely the case without noise. On the other hand, the v-velocity is more

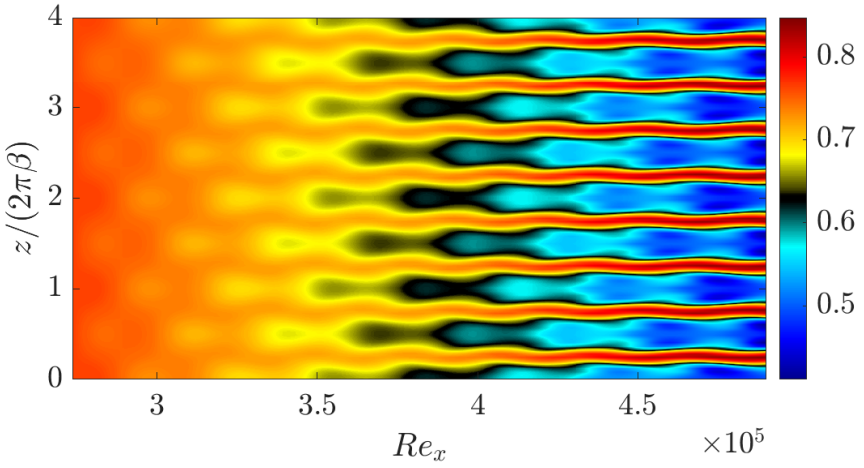

(a) y = 2.55

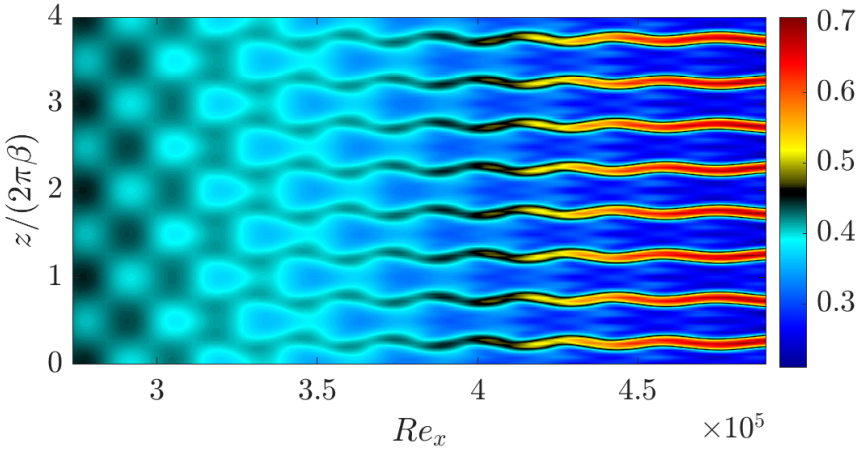

(b) y = 1.31

Figure 3.7: Contours of the instantaneous u-velocity for high amplitude oblique-wave breakdown.

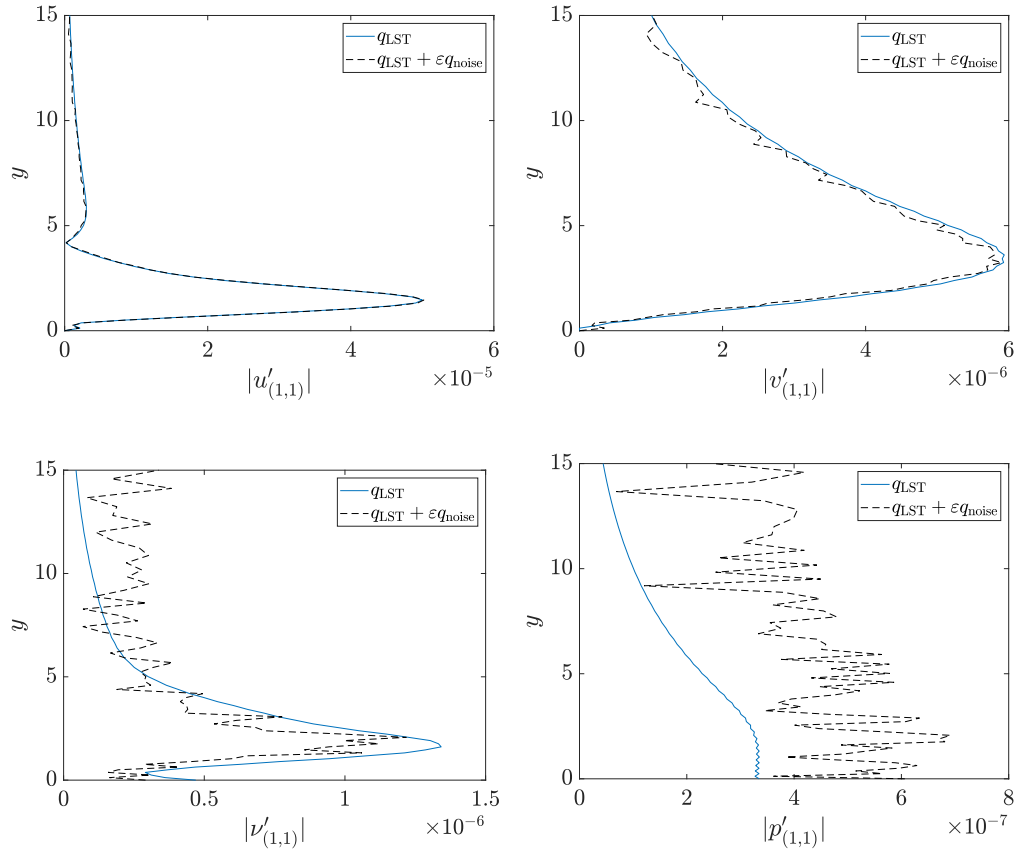

Figure 3.8: Oblique-wave inlet boundary condition with and without random noise.

affected by the numerical noise, yet we still obtain good qualitative agreement. The other modes (e.g., the vortex mode) are evolved accurately by the NOWNS calculation with noisy inlet condition, and the contour plots with and without the numerical noise are indistinguishable from each other, and so are not plotted here.

3.4.4 Blowing/suction strip

Blowing/suction strips are frequently used to study laminar-turbulent boundary layer transition in low-speed boundary layer flows (Fasel et al., 1990; Rist and Fasel, 1995; Sayadi et al., 2013; Huai et al., 1997; Rigas et al., 2021). Here, we introduce disturbances by specifying a non-zero wall-normal velocity such that $v(y = 0) = f(x, z, t)$, for some function $f(x, z, t)$ that is periodic in t and z. NPSE does not support blowing/suction strips because they introduce non-modal disturbances, demonstrating an advantage of NOWNS. However, we note that Herbert's second stability theory yields an inlet boundary condition so that NPSE (and NOWNS)

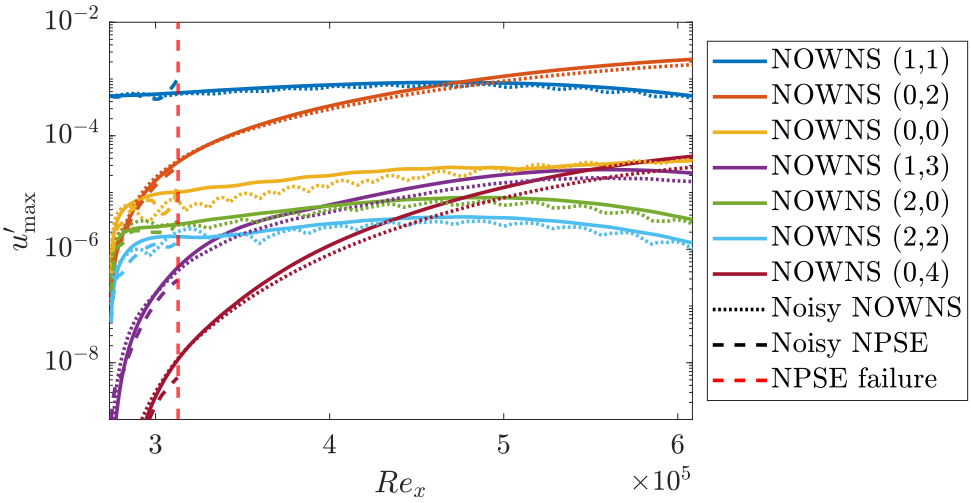

Figure 3.9: Amplitude of u' v.s. streamwise coordinate, Re_x, for low amplitude oblique-wave breakdown with and without random noise.

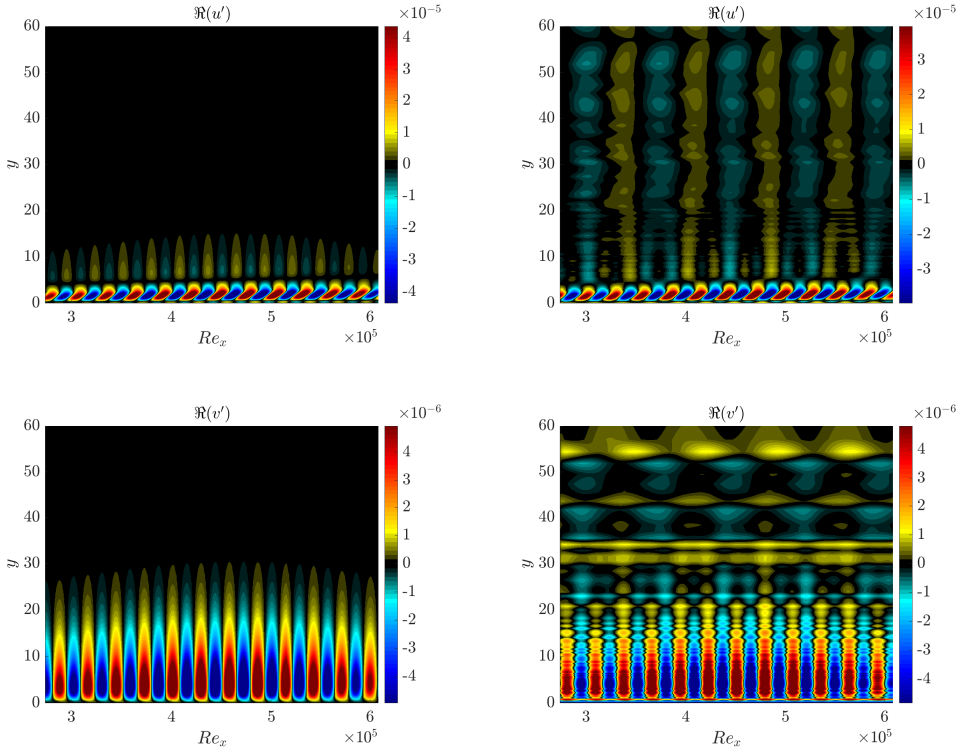

Figure 3.10: Contour plots of the u- and v velocities of the oblique wave, with and without random noise.

can be used to study fundamental (K-type) and subharmonic (H-type) transition (Herbert, 1988, 1997).

Rist and Fasel (1995) used DNS with a blowing/suction strip to study K-type transition (Rist and Fasel, 1995), while similar studies were performed by Sayadi et al. (2013) using DNS (Sayadi et al., 2013), and by Rigas et al. (2021) using a harmonic balance method (HBM) (Rigas et al., 2021). The blowing/suction strip is given by

$$f(x,z,t) = 5\times10^{-3}\sin(\omega t)v_a(x) + 1.3\times10^{-4}\cos(\beta z)v_s(x), \tag{3.31a}$$

where

$$v_a(Re_x) = \begin{cases} 0, & Re_x \le Re_x(x_1) \\ 15.1875\xi^5 - 35.4375\xi^4 + 20.25\xi^3, & Re_x(x_1) < Re_x \le Re_x(x_m) \\ -v_a\big(2Re_x(x_m) - Re_x\big), & Re_x(x_m) < Re_x \le Re_x(x_2) \\ 0, & Re_x(x_2) < Re_x \end{cases} \tag{3.31b}$$

$$v_s(Re_x) = \begin{cases} 0, & Re_x \le Re_x(x_1) \\ -3\xi^4 + 4\xi^3, & Re_x(x_1) < Re_x \le Re_x(x_m) \\ v_s\big(2Re_x(x_m) - Re_x\big), & Re_x(x_m) < Re_x \le Re_x(x_2) \\ 0, & Re_x(x_2) < Re_x \end{cases} \tag{3.31c}$$

for $Re_x(x_1) = 1.3438\times10^5$, $Re_x(x_2) = 1.5532\times10^5$, $x_m = (x_1+x_2)/2$, and $\xi = (Re_x - Re_x(x_1))/(Re_x(x_m) - Re_x(x_1))$. We choose $F = 110\times10^{-6}$ and $b = 0.423\times10^{-3}$ with $M = N = 4$, while the grid extends over $Re_x \in [1.33956\times10^5, 2.72\times10^5]$ and $y \in [0, 60]$, with 1,300 stations in x and 100 grid points in y.

Figure 3.11 shows excellent agreement between the u' amplitudes of NOWNS and the DNS of Rist and Fasel (1995) (Rist and Fasel, 1995). We note that in the early stages of the march there is disagreement between the DNS and NOWNS calculations because the blowing/suction strip causes upstream effects that NOWNS neglects by construction. However, these disturbances are convective in nature, and the amplitudes predicted by NOWNS rapidly converge to those predicted by DNS as the march progresses downstream.

3.5 Summary

In this chapter we developed the NOWNS approach and validated for low-speed flat-plate boundary-layer flows by comparing to DNS data in the literature for the 2D evolution of a TS, 3D oblique-wave breakdown, and a fundamental (K-type) transition case. In addition, we demonstrated that NOWNS supports stronger nonlinearities than NPSE. For the 2D high amplitude evolution of a TS wave, we find

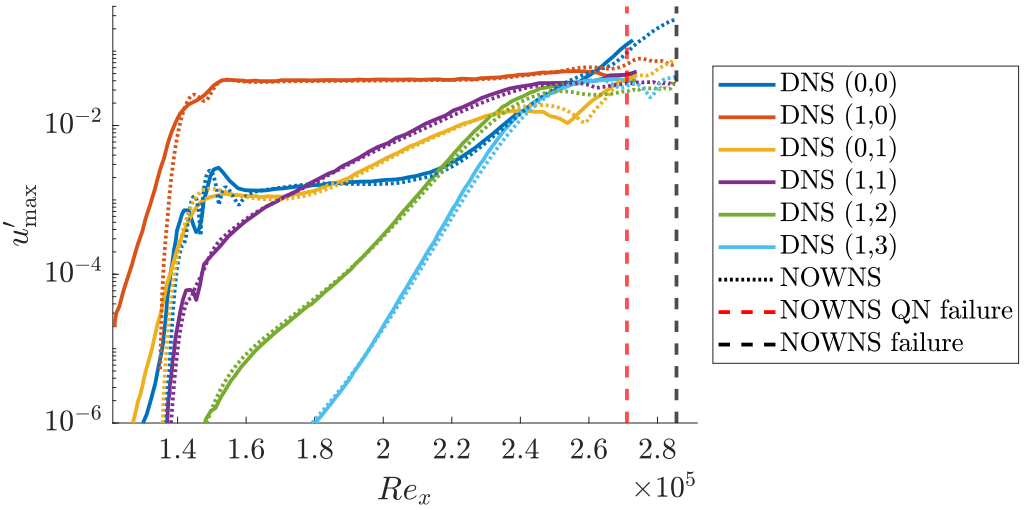

Figure 3.11: Amplitude of u' v.s. streamwise coordinate, Re_x, for K-type transition

that the NOWNS march remains accurate until the point where the Newton solver fails to converge, while for the 3D high amplitude oblique-wave breakdown case, NOWNS marches all the way to the end of the DNS calculation. We also show that NOWNS is robust to numerical noise in the inlet boundary-condition, and that a blowing/suction strip can be used to introduce disturbances, which is advantageous because blowing/suction strips are frequently used in DNS studies but cannot be used in NPSE calculations.

Chapter 4

A GREEDY APPROACH TO RECURSION PARAMETER SELECTION

As discussed in Chapters 2 and 3, previous work on OWNS has chosen recursion parameters *heuristically*, based on the Euler equations, linearized about a uniform flow. This section proposes a *greedy* algorithm for recursion parameter selection, and we demonstrate that it achieves rapid error convergence relative to the heuristic approach for low-speed boundary-layer flows. This section is adapted from Sleeman and Colonius (2025).

4.1 Greedy algorithm for recursion parameter selection

Assuming $\alpha_m \neq \alpha_n$ for all $m = i^{(+)}$ and $n = i^{(-)}$, propositions 2.2.16 and 2.2.31 define recursion parameter sets that ensure convergence. However, these sets are large and require the eigenvalues of M, so previous work has used heuristic parameter selection to avoid this eigendecomposition while maintaining stability and accuracy with $N_\beta \ll N$. Although it has been used successfully, heuristic selection converges slowly, so we propose a greedy algorithm to accelerate convergence.

4.1.1 Objective function

We define $\beta_\pm^j = \{\beta_+^j, \beta_-^j\}$ and the recursion parameter set $\Xi_{N_\beta} \equiv \{\beta_\pm^j\}_{j=0}^{N_\beta}$, as well as the functions

$$\hat{\mathcal{J}}_+(\alpha;\Xi_{N_\beta}) \equiv \prod_{j=0}^{N_\beta-1} \frac{|\alpha-\beta_+^j|}{|\alpha-\beta_-^j|}, \quad \hat{\mathcal{J}}_-(\alpha;\Xi_{N_\beta}) \equiv \prod_{j=0}^{N_\beta-1} \frac{|\alpha-\beta_-^j|}{|\alpha-\beta_+^j|}, \tag{4.1a}$$

and

$$\hat{\mathcal{J}}(\alpha_m,\alpha_n;\Xi_{N_\beta}) \equiv \prod_{j=0}^{N_\beta-1} \frac{|\alpha_m-\beta_+^j|}{|\alpha_m-\beta_-^j|}\frac{|\alpha_n-\beta_-^j|}{|\alpha_n-\beta_+^j|}. \tag{4.1b}$$

Then, by proposition 2.2.17 the OWNS-P error scales as

$$\mathcal{J}(\Xi_{N_\beta}) \equiv \max_{m=i^{(+)},n=i^{(-)}} \hat{\mathcal{J}}(\alpha_m,\alpha_n;\Xi_{N_\beta}) = \|F_{++}\|\|F_{--}^{-1}\|, \tag{4.1c}$$

while by proposition 2.2.34 the OWNS-R error scales as

$$\begin{aligned}\mathcal{J}^{(R)}(\Xi_{N_\beta}) &\equiv \max\Big\{\max_{m=i^{(+)}} \hat{\mathcal{J}}_+(\alpha_m;\Xi_{N_\beta}), \max_{n=i^{(-)}} \hat{\mathcal{J}}_-(\alpha_m;\Xi_{N_\beta})\Big\} \\ &= \max\big\{\|F_{++}\|, \|F_{--}^{-1}\|\big\}.\end{aligned} \tag{4.1d}$$

4.1.2 A summary of the greedy algorithm

By Propositions 2.2.17 and 2.2.34, the OWNS-P and OWNS-R errors scale linearly with $\mathcal{J}(\Xi_{N_\beta})$ and $\mathcal{J}^{(R)}(\Xi_{N_\beta})$ for small values, respectively. Thus, for two recursion parameter sets $\Xi^{(1)}_{N_\beta}$ and $\Xi^{(2)}_{N_\beta}$, we expect $\Xi^{(1)}_{N_\beta}$ to introduce less error if $\mathcal{J}(\Xi^{(1)}_{N_\beta}) < \mathcal{J}(\Xi^{(2)}_{N_\beta})$. We seek Ξ_{N_β} such that $\mathcal{J}$ is minimized for $N_\beta \ll N$, which is well-posed as an optimization problem due to the continuity of the objective function (a quotient of polynomials with a non-zero denominator). However, identifying the optimal set is computationally intractable because we must consider

$$\frac{N_+!}{N_\beta!(N_+ - N_\beta)!}\frac{N_-!}{N_\beta!(N_- - N_\beta)!}$$

combinations of recursion parameters, since we must choose N_β recursion parameters from the N_+ downstream-going and the N_- upstream-going eigenvalues. Therefore, we use the greedy algorithm outlined in algorithm 1, which we briefly summarize below, to choose quasi-optimal parameter sets.

Given a recursion parameter set $\Xi_{N_{\text{greedy}}}$ with $N_{\text{greedy}} < N_\beta$, we can add two new recursion parameters, $(\beta_+^{N_{\text{greedy}}}, \beta_-^{N_{\text{greedy}}})$, to reduce the error. We compute

$$\tilde{m} = \arg\max_{i=i^{(+)}} \hat{\mathcal{J}}_+(\alpha_m; \Xi_{N_{\text{greedy}}}), \quad \tilde{n} = \arg\max_{i=i^{(-)}} \hat{\mathcal{J}}_-(\alpha_n; \Xi_{N_{\text{greedy}}}),$$

and choose $\beta_+^{N_{\text{greedy}}} = \alpha_{\tilde{m}}$ and $\beta_-^{N_{\text{greedy}}} = \alpha_{\tilde{n}}$. This choice does not necessarily lead to the optimal error decrease, but it locally eliminates the largest source.

Remark 4.1.1 *Previous work on OWNS combined heuristic parameter selection with mode-tracking, where important discrete modes (e.g., Kelvin-Helmholtz in free-shear flows or Mack's second mode in high-speed boundary layers) were added to the recursion parameter set to improve approximation accuracy (Towne and Colonius, 2015; Towne et al., 2022; Zhu and Towne, 2023). While previous methods manually identified eigenvalues to track, the present work proposes an automatic approach with minimal user intervention.*

Remark 4.1.2 *The greedy algorithm can be modified so that it is initialized with user-specified recursion parameters instead of randomly chosen recursion parameters. For example, choose β_+^0 corresponding to Mack's second mode, and β_-^0 as the upstream-going mode closest to the real axis.*

Algorithm 1 Greedy recursion parameter selection

$\beta_+^0 \leftarrow \alpha_m$ for randomly chosen $m = i^{(+)}$
$\beta_-^0 \leftarrow \alpha_n$ for randomly chosen $n = i^{(-)}$
$\Xi_{N_{\text{greedy}}} \leftarrow \{\beta_\pm^0\}$ where $\beta_\pm^0 = \{\beta_+^0, \beta_-^0\}$
$N_{\text{greedy}} \leftarrow 1$
while $N_{\text{greedy}} < N_\beta$ **do**
  $\tilde{m} \leftarrow \arg\max_{m=i^{(+)}} \hat{\mathcal{J}}_+(\alpha_m; \Xi_{N_{\text{greedy}}})$
  $\tilde{n} \leftarrow \arg\max_{n=i^{(-)}} \hat{\mathcal{J}}_-(\alpha_n; \Xi_{N_{\text{greedy}}})$
  $\beta_\pm^{N_{\text{greedy}}} \leftarrow \{\alpha_{\tilde{m}}, \alpha_{\tilde{n}}\}$
  $\Xi_{N_{\text{greedy}}+1} \leftarrow \{\beta_\pm^j\}_{j=0}^{N_{\text{greedy}}}$
  $N_{\text{greedy}} \leftarrow N_{\text{greedy}} + 1$
end while

4.1.3 Numerical stability of the recursive filter

OWNS solves equations of the form

$$(M - i\beta_-^j)\hat{\boldsymbol{\phi}}^{j+1} = (M - i\beta_+^j)\hat{\boldsymbol{\phi}}^j, \quad j = 0, \ldots, N_\beta - 1.$$

If the exact solution is given by $\hat{\boldsymbol{\varphi}}^{j+1}$, then the rounding error introduced by solving the linear system is bounded by

$$\begin{aligned}\frac{\|\hat{\boldsymbol{\phi}}^{j+1} - \hat{\boldsymbol{\varphi}}^{j+1}\|}{\|\hat{\boldsymbol{\varphi}}^{j+1}\|} &\leq \kappa(M - i\beta_-^j I)\frac{\|(M - i\beta_-^j I)\hat{\boldsymbol{\phi}}^{j+1} - (M - i\beta_+ I)\hat{\boldsymbol{\phi}}^j\|}{\|(M - i\beta_+ I)\hat{\boldsymbol{\varphi}}^j\|} \\ &\leq \kappa(M - i\beta_-^j I)\frac{\|M - i\beta_-^j I\|\|\hat{\boldsymbol{\phi}}^{j+1} - \hat{\boldsymbol{\phi}}^j\| + |\beta_+^j - \beta_-^j|\|\hat{\boldsymbol{\phi}}^j\|}{\|(M - i\beta_+ I)\hat{\boldsymbol{\varphi}}^j\|}.\end{aligned}$$

If $\beta_+^j = \beta_-^j$, then $\|\hat{\boldsymbol{\phi}}^{j+1} - \hat{\boldsymbol{\phi}}^j\| = O(\epsilon_{\text{mach}})$, where ϵ_{mach} is machine epsilon, and the error is $O(\epsilon_{\text{mach}}\kappa(M - i\beta_-^j I))$. However, this error grows as $|\beta_+^j - \beta_-^j|$ grows, and accumulates for $j = 0, \ldots, N_\beta - 1$. Therefore, it is preferable for $|\beta_-^j - \beta_+^j|$ to be small, so we re-order the recursion parameters such that $|\beta_+^{j-1}| < |\beta_+^j|$ and $|\beta_-^{j-1}| < |\beta_-^j|$ for $j = 1, \ldots, N_\beta - 1$. We further note that the error bounds and objective functions do not depend on the order of the recursion parameters, so we are free to re-order them, which is necessary when using greedy selection.

Remark 4.1.3 *Heuristic parameter selection does not explicitly sort the recursion parameters, but in practice they are chosen such that each pair has the same magnitude ($|\beta_+^j| \approx |\beta_-^j|$).*

4.1.4 Greedy algorithm and spatial marching

For systems where M varies slowly in x, the recursion parameters computed at the inlet can be reused downstream. However, they generally need to be updated to

keep the error low, which can be done by *tracking* them as they evolve downstream, as shown in algorithm 2. When the number of upstream- and downstream-going characteristics changes, such as supersonic boundary-layer flows when the number of subsonic and supersonic grid points changes, it can be advantageous (although not necessary) to perform the greedy algorithm again to keep the error low.

Consider the recursion parameters, $\Xi_{N_\beta}^{(i-1)}$, at station $i-1$, which are eigenvalues of $M^{(i-1)}$. If the number of upstream- and downstream-going characteristics is the same at stations $i-1$ and i, then given $M^{(i)}$, the recursion parameters from $\Xi_{N_\beta}^{(i-1)}$ can be used with, for example, MATLAB's `eigs` function to update to $\Xi_{N_\beta}^{(i)}$. For large, sparse M, this is much less costly than solving for the complete eigenspectrum. If the number of characteristics changes, the greedy algorithm is performed again, as shown in algorithm 2.

Algorithm 2 Recursion parameter tracking

Compute $N_+^{(1)}$ and $N_-^{(1)}$
Compute $\Xi_{N_\beta}^{(1)}$ using algorithm 1 with the eigenvalues of $M^{(1)}$
for $i = 2, \ldots, N_x$ **do**
  Compute $N_+^{(i)}$ and $N_-^{(i)}$
  if $N_+^{(i)} = N_+^{(i-1)}$ **then**
    for $j = 0, \ldots, N_\beta$ **do**
      $\tilde{\beta}_\pm \leftarrow \beta_\pm^j$ from $\Xi_{N_\beta}^{(i-1)}$
      Compute β_+^j by finding eigenvalue of $M^{(i)}$ closest to $\tilde{\beta}_+$
      Compute β_-^j by finding eigenvalue of $M^{(i)}$ closest to $\tilde{\beta}_-$
      $\beta_\pm^j \leftarrow \{\beta_+^j, \beta_-^j\}$
    end for
    $\Xi_{N_\beta}^{(i)} \leftarrow \{\beta_\pm^j\}_{j=0}^{N_\beta - 1}$
  else
    Compute $\Xi_{N_\beta}^{(i)}$ using algorithm 1 with the eigenvalues of $M^{(i)}$
  end if
end for

4.1.5 Cost trade-off

OWNS avoids computing the eigendecomposition of M by using a recursive filter, whereas the greedy algorithm selects recursion parameters based on these eigenvalues. While this may seem contradictory, the greedy approach can reduce the overall computational cost by requiring fewer recursion parameters, thereby lowering the cost of solving the OWNS system. Moreover, the full eigenspectrum is needed only at a small number of stations, potentially just at the inlet, and the selected eigenval-

ues can be efficiently updated by *tracking* them downstream. Moreover, as noted in remark 4.1.1, this approach has previously been employed for eigenvalues chosen manually by the user.

For linear calculations, OWNS-R can reduce computational cost relative to OWNS-P, though selecting appropriate recursion parameters is more challenging. We show that OWNS-P with greedy selection outperforms OWNS-P with heuristic selection, and that OWNS-R with greedy selection is more efficient than both. In optimization tasks, such as the resolvent analysis by Towne et al. (2022), the initial cost of computing recursion parameters can be amortized over many optimization iterations. For nonlinear calculations, we demonstrate that NOWNS with greedy selection is more efficient than with heuristic selection.

Remark 4.1.4 *This work focuses on flows with a single inhomogeneous direction (normal). Computing the eigenvalues of M for flows with two inhomogeneous directions (normal and spanwise) may not be feasible, making heuristic selection the preferred method for these flows.*

4.2 Demonstration of the greedy algorithm for a single station

Here we demonstrate the greedy algorithm for a two-dimensional (2D) subsonic boundary-layer flow, where the disturbance frequency is $F = 86 \times 10^{-6}$, while the wall-normal extent is $y \in [0, 75]$ with $N_y = 150$ grid points, which matches the parameters used by Bertolotti et al. (1992). For now, we focus only on comparing the greedy and heuristic parameters at $Re_x = 1.6 \times 10^6$. We show the following:

1. Greedy parameter selection yields a much more rapid convergence of the objective functions for both OWNS-P and OWNS-R.
2. Heuristic parameter selection yields a stable march for OWNS-P, while the same recursion parameters yield an unstable march for OWNS-R.
3. Rounding errors when computing β_*^j for OWNS-R lead to increasing error with increasing N_β, while the OWNS-P error is zero to machine zero-precision.

4.2.1 Convergence of the objective function

Figure 4.1a shows that although the $\mathcal{J}$ decreases with increasing N_β for both greedy and heuristic parameter selection, it decreases far more rapidly for greedy selection (although greedy selection leads to larger values of $\mathcal{J}$ for small N_β). In contrast, for

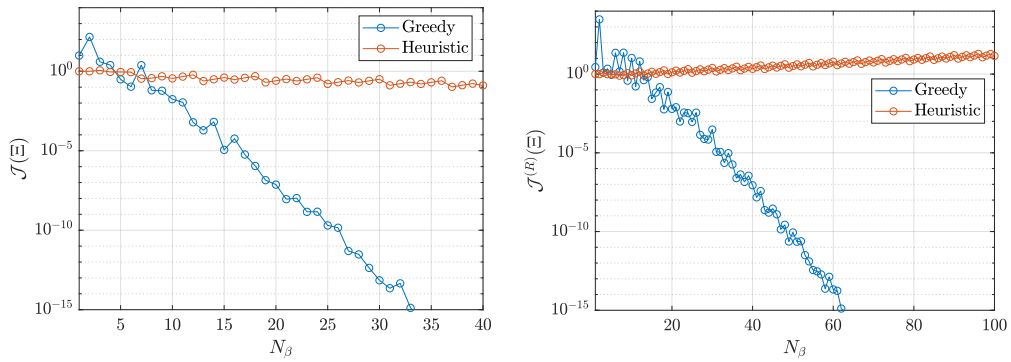

(a) OWNS-P (b) OWNS-R

Figure 4.1: Convergence of the objective function for greedy and heuristic parameter selection.

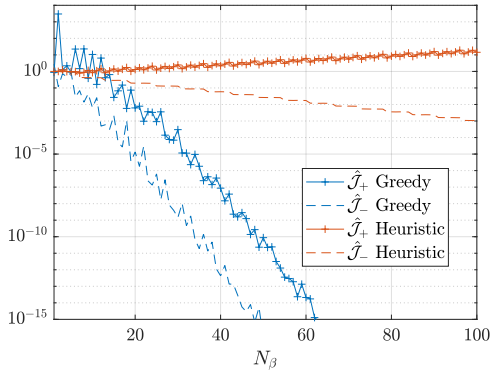

Figure 4.2: Convergence of the objective function, split into upstream- and downstream-going components, for greedy and heuristic parameter selection.

OWNS-R, heuristic selection leads to an increase in $\mathcal{J}^{(R)}$, while greedy selection leads to a rapid decrease. Figure 4.2 plots both $\hat{\mathcal{J}}_+$ and $\hat{\mathcal{J}}_-$, showing that although $\hat{\mathcal{J}}_-$ is decreasing for heuristic selection, $\hat{\mathcal{J}}_+$ is increasing, which causes $\mathcal{J}^{(R)}$ to increase. This highlights that OWNS-P will always have a lower error than OWNS-R small $\|F_{++}\|$ and $\|F_{--}^{-1}\|$, since

$$\|F_{++}\|\|F_{--}^{-1}\| < \max\{\|F_{++}\|, \|F_{--}^{-1}\|\}, \quad \|F_{++}\|, \|F_{--}^{-1}\| < 1.$$

Figure 4.3 shows the greedy and heuristic recursion parameter sets for $N_\beta = 20$. The greedy algorithm places parameters along the branches of acoustic and vortical waves, focusing near the origin where the eigenvalues are closest, and uses the discrete Tollmien-Schlichting (TS) wave as a recursion parameter. The heuristic approach targets the same eigenvalues but is less efficient, with many parameters far from their targets, which explains its slower convergence.

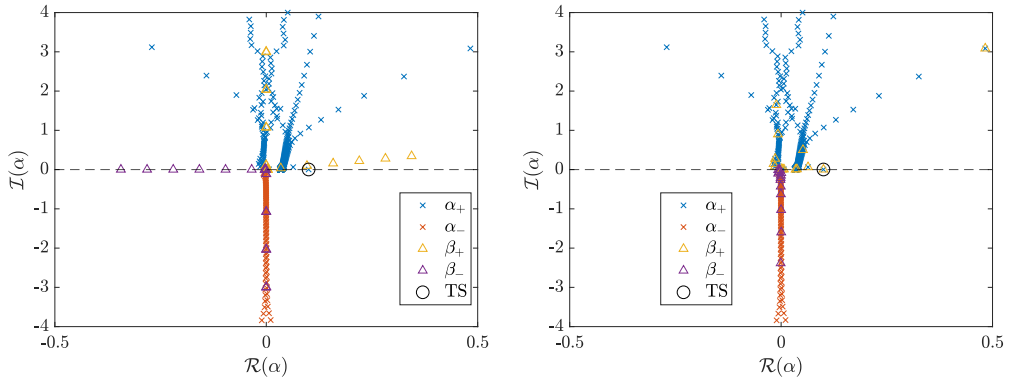

(a) Heuristic (b) Greedy

Figure 4.3: Recursion parameters plotted against spectrum for heuristic and greedy recursion parameter selection with $N_\beta = 20$.

4.2.2 Stability of the march

All upstream-going modes must be removed for the march to be stable. Figure 4.4a demonstrates for heuristic parameter selection that P_{N_β} removes all upstream-going waves from M, while Figure 4.4b demonstrates that $P^{(R)}_{N_\beta}$ does not. For $\eta = 0$, we observe that the OWNS-R spectrum has many eigenvalues with $\mathcal{I}(\alpha) < 0$, and taking $\eta = 1000$ allows us to verify that these are upstream-going modes according to Briggs' criterion. Therefore, the exist parameter sets where the march is stable for OWNS-P, but unstable for OWNS-R. Repeating this analysis with greedy selection yields stable marches for both OWNS-P and OWNS-R.

Remark 4.2.1 *Zhu and Towne (2023) noted that OWNS-P and OWNS-R approximate the V and E, respectively. Therefore, we expect OWNS-P to better remove upstream-going modes since it makes no approximations to E, which is consistent with the above observations.*

Remark 4.2.2 *Figures 3 and 6 from Zhu and Towne (2023) show that the OWNS-R operator removes all upstream-going modes for the dipole and jet test cases, while Figure 10 suggests it still supports upstream-going modes for their supersonic boundary-layer case. Thus, our observations in Figure 4.4b for the low-speed boundary-layer flow align with those of Zhu and Towne (2023) for their supersonic case.*

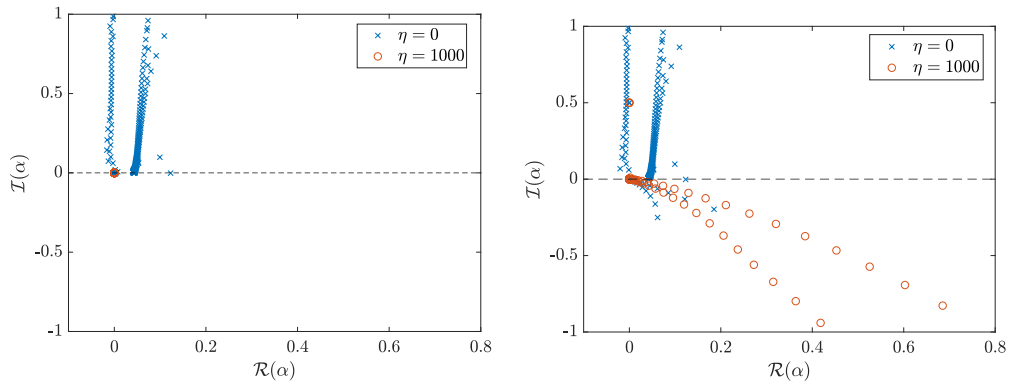

(a) OWNS-P, $N_\beta = 20$ (b) OWNS-R, $N_\beta = 55$

Figure 4.4: Comparison of OWNS spectrum with heuristic parameter selection for $\eta = 0$ and $\eta = 1000$. According to Briggs' criterion, $\mathcal{I}(\alpha) < 0$ for large values of η indicates a downstream-going mode. For $\eta = 0$, we wish to have $\mathcal{I}(\alpha) \geq 0$ for the march to be stable. We achieve a stable march using OWNS-P, but not for OWNS-R.

4.2.3 Accuracy of the projection operator

Consider a solution $\hat{\boldsymbol{\phi}} = V_+\hat{\boldsymbol{\psi}}_+ + V_-\hat{\boldsymbol{\psi}}_-$, where $P\hat{\boldsymbol{\phi}} = V_+\hat{\boldsymbol{\psi}}_+$ by definition. We choose random coefficients $\hat{\boldsymbol{\psi}}$ and compute the relative errors

$$\frac{\|P_{N_\beta}[V_+\boldsymbol{\psi}_+ + V_-\boldsymbol{\psi}_-] - V_+\boldsymbol{\psi}_+\|}{\|V_+\boldsymbol{\psi}_+\|}, \quad \frac{\|P^{(R)}_{N_\beta}[V_+\boldsymbol{\psi}_+ + V_-\boldsymbol{\psi}_-] - V_+\boldsymbol{\psi}_+\|}{\|V_+\boldsymbol{\psi}_+\|}, \tag{4.2}$$

for OWNS-P and OWNS-R, respectively. Similarly, we consider specifically the ability to retain only the TS wave and compute the relative errors

$$\frac{\|P_{N_\beta}\boldsymbol{\phi}_{\mathrm{TS}} - \boldsymbol{\phi}_{\mathrm{TS}}\|}{\|\boldsymbol{\phi}_{\mathrm{TS}}\|}, \quad \frac{\|P^{(R)}_{N_\beta}\boldsymbol{\phi}_{\mathrm{TS}} - \boldsymbol{\phi}_{\mathrm{TS}}\|}{\|\boldsymbol{\phi}_{\mathrm{TS}}\|}. \tag{4.3}$$

Figure 4.5a shows for OWNS-P that greedy selection yields rapid error convergence, and that machine zero precision is achieved at $N_\beta = 29$, while heuristic selection yields slow convergence. For OWNS-R, we observe that the error is large compared to OWNS-P, and that although the error initially decreases with increasing N_β, it begins to grow again around $N_\beta = 45$ for greedy selection and $N_\beta = 55$ for heuristic.

Figures 4.5a and 4.5b show that whereas the OWNS-P projection error is (nearly) a monotonically decreasing function of N_β, the OWNS-R projection error is an increasing function of N_β for sufficiently large values of N_β ($N_\beta \approx 45$ and $N_\beta \approx 55$ for greedy and heuristic parameter selection, respectively). Figure 4.5b shows that although $\mathcal{J}^{(R)}$ is decreasing rapidly for greedy selection, the projection error is

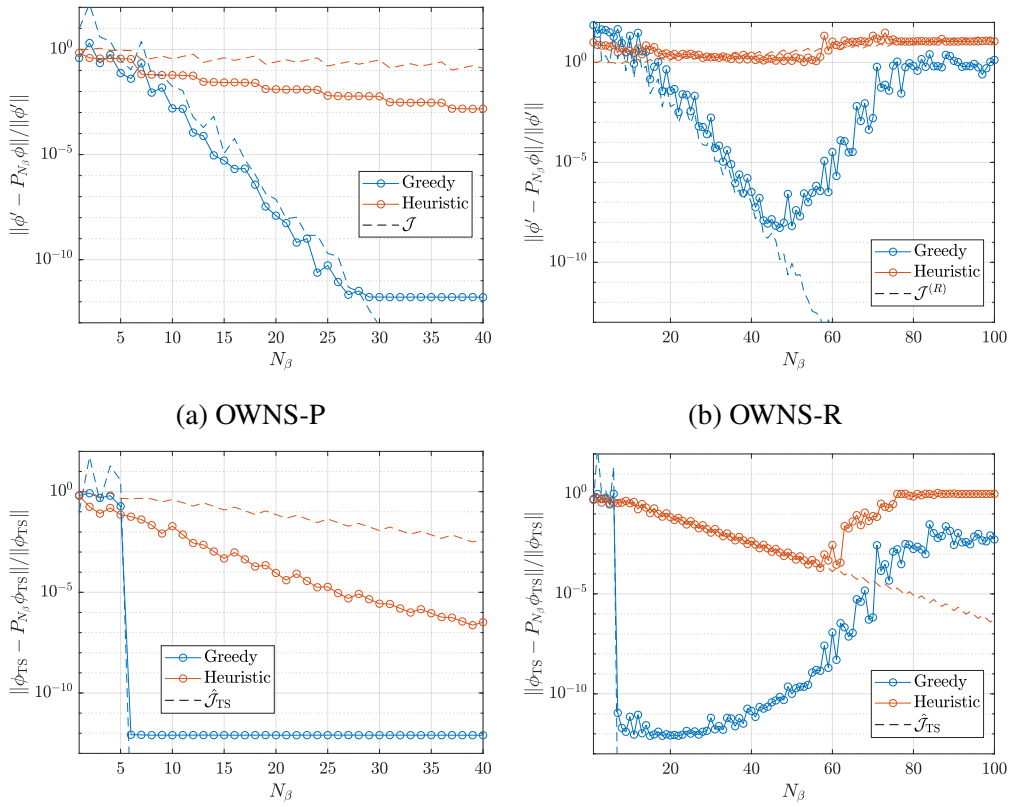

(a) OWNS-P

(b) OWNS-R

(c) OWNS-P, TS wave only

(d) OWNS-R, TS wave only

Figure 4.5: Error convergence as a function of N_β for OWNS-P and OWNS-R for the 2D low-speed boundary-layer flow.

increasing due to rounding error when computing β_*^j. We demonstrate this in Figure 4.6 by plotting an estimate for the relative error in the polynomial factorization, which we compute by choosing random complex numbers $c_k = a_k + ib_k$ with $a_k, b_k \in [-1, 1]$ for $k = 1, \ldots, 100$ and computing the error in the polynomial approximation as

$$\max_{k=1,\ldots,100} \frac{|2\prod_{j=1}^{N_\beta}(c_k - \beta_*^j) - \prod_{j=1}^{N_\beta}(c_k - \beta_-^j) - \prod_{j=1}^{N_\beta}(c_k - \beta_+^j)|}{|\prod_{j=1}^{N_\beta}(c_k - \beta_-^j) - \prod_{j=1}^{N_\beta}(c_k - \beta_+^j)|}. \tag{4.4}$$

Figure 4.6 shows that this error is an increasing function of N_β, which explains why adding more recursion parameters for sufficiently large values of N_β increases, rather than decreases the OWNS-R projection error. OWNS-R can lead to a reduced computational cost relative to OWNS-P, but this is helpful only if the OWNS-R march is stable and accurate. Therefore, future work should investigate how to perform the polynomial factorization such that the effects of rounding errors on the accuracy of the OWNS-R approximation are minimized.

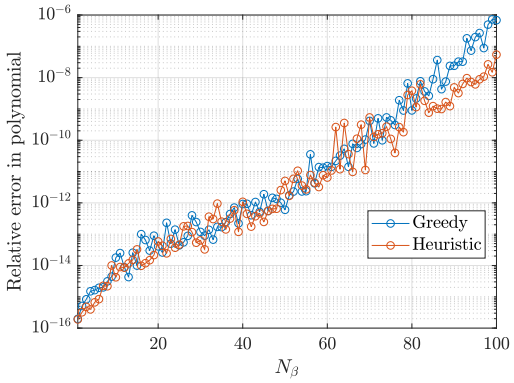

Figure 4.6: For OWNS-R, the error in computing β_*^j increases with increasing N_β.

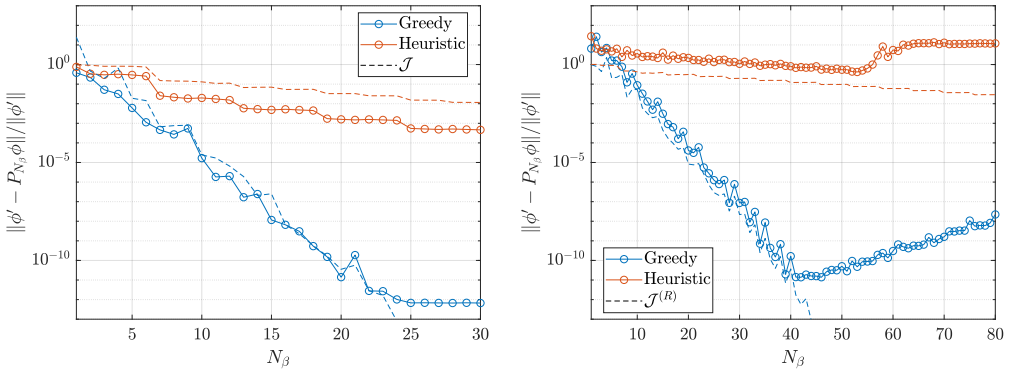

(a) OWNS-P (b) OWNS-R

Figure 4.7: Error convergence as a function of N_β for OWNS-P and OWNS-R for the low-speed oblique wave case.

4.2.4 3D low-speed boundary-layer flow

We investigate the oblique-wave case studied by Joslin et al. (1993), with disturbance frequency and wavenumber are $F = 86\times10^{-6}$ and $b = 0.222\times10^{-3}$, respectively, for the wall-normal domain $y \in [0, 60]$ with $N_y = 100$ at $Re_x = 2.74 \times 10^5$. Figure 4.7 shows that greedy selection yields rapid convergence of the objective function and projection error. Moreover, OWNS-P achieves machine-zero error with $N_\beta = 24$, while OWNS-R does not, due to rounding errors in computing β_*^j. We further note that the 3D case converges with fewer recursion parameters because the upstream- and downstream-going branches are more widely separated than in the 2D case, which makes it easier to choose recursion parameters that keep both $\|F_{++}\|$ and $\|F_{--}^{-1}\|$ small, as noted by Towne and Colonius (2015).

4.3 Demonstration of the greedy algorithm for spatial marching

The greedy algorithm is advantageous because it yields a rapidly convergent OWNS approximation without the need to manually choose flow-dependent recursion parameters. However, this requires that the eigenvalues of M be computed, which adds a cost that is not present in the heuristic approach. Here we demonstrate that the overall computational cost of spatial-marching using OWNS can be reduced using the greedy selection (algorithm 1) and tracking (algorithm 2) procedures.

4.3.1 Linear calculation

We first demonstrate, for the oblique-wave case studied by Joslin et al. (1993) and discussed in Section 4.2.4, that greedy parameter selection reduces computational cost in both linear and nonlinear calculations. The problem parameters remain the same as before, and we consider the streamwise domain $Re_x \in [2.74, 6.08] \times 10^5$ with $N_x = 2000$ stations. We compare the number of recursion parameters required for convergence and measure speed-up based on total wall-clock time, including all steps of the greedy selection process.

Due to instability in OWNS-R with heuristic parameter selection for the linear evolution of the oblique wave, we compare OWNS-P and OWNS-R with greedy selection to OWNS-P with heuristic selection. To ensure meaningful comparisons, we select N_β as the smallest value that yields 10%, 1%, and 0.1% relative error in the N-factor, measured against the OWNS-P greedy calculation with $N_\beta = 30$. We choose to measure error using the N-factor. Table 4.1 summarizes the data, and shows that the speed-up of OWNS-R with greedy parameter selection is most pronounced when the desired error is 1%, while for OWNS-P with greedy parameter selection it is 0.1%. If a tight error tolerance is desired, then OWNS-P is preferable, while OWNS-R is preferable for looser error tolerances. We further that the greedy approach yields a net decrease in computational cost, despite the added cost of computing the eigenvalues, as it allows convergence with fewer recursion parameters.

4.3.2 Nonlinear calculation

For the nonlinear calculations, we truncate the Fourier series at $M = 3$ temporal and $N = 4$ spanwise modes, while we specify at the inlet that the oblique wave has amplitude $u'^{(1,1)}_{\max} = \sqrt{2} \times 10^{-3}$. We again select N_β as the smallest value for which the relative error in the N-factor is 0.1% with respect to the reference solution. For NOWNS, heuristic and greedy parameter selection require $N_\beta = 18$ and $N_\beta = 6$, respectively, resulting in a speed-up of 3.83 for the greedy approach

	N_β			Speed-up		
Error	P-H	P-G	R-G	P-H	P-G	R-G
10%	11	5	29	1.0	2.3	3.6
1%	17	5	29	1.0	3.9	6.0
0.1%	18	5	36	1.0	4.2	4.9

Table 4.1: Speed-up achieved by using greedy parameter selection with OWNS-P (P-G) and OWNS-R (R-G) relative to heuristic parameter selection with OWNS-P (P-H) for different relative errors in the N-factor for the 3D low-speed boundary-layer flow.

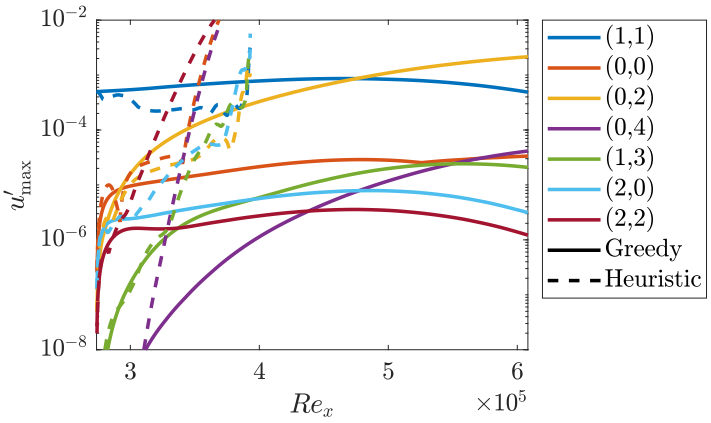

Figure 4.8: NOWNS for oblique-wave breakdown, comparing greedy and heuristic recursion parameter selection with $N_\beta = 6$. Although NOWNS with greedy selection is sufficiently converged, heuristic selection is not, and the solution blows-up.

relative to the heuristic. Figure 4.8 compares solutions obtained using NOWNS with both parameter selection methods using $N_\beta = 6$. While greedy selection yields a converged solution, the heuristic does not and the solution diverges.

4.4 Summary

We demonstrated that our proposed greedy algorithm can yield faster convergence and a reduced computational cost, relative to heuristic parameter selection, for linear and nonlinear stability analyses of boundary-layer flows. We have focused on flows with a single inhomogeneous direction (the wall-normal direction), and we note that the approach may not extend directly to flows with two inhomogeneous directions (wall-normal and spanwise) due to the increased grid size. Future work should explore how to adapt the greedy algorithm for such cases. Additionally, future work should investigate the development of *a posteriori* error estimates so that we can estimate the error introduced by a recursion parameter set without needing to

calculate the eigen-spectrum of M, which may also make it possible to indirectly implement the greedy algorithm without solving for the eigenvalues of M.

Chapter 5

THE NOWNS APPROACH FOR LOW-SPEED BOUNDARY-LAYER TRANSITION PREDICTION

In Chapter 3 we demonstrated that NOWNS can replicate the K-type transition scenario simulated using DNS by Rist and Fasel (1995). More recently, Sayadi et al. (2013) computed the complete transition to turbulence for the H- and K-type paths. We show that NOWNS matches the u-velocity amplitudes predicted by Sayadi et al. (2013) in the early stages of transition, and that it is able to qualitatively reproduce their u-velocity contour plots demonstrating the aligned (staggered) Λ-vortex structure that is characteristic of K-type (H-type) transition. The NOWNS march fails before the flow becomes fully-turbulent, but we plot the mean skin friction coefficient to demonstrate that NOWNS is able to accurately predict the initial rise in skin-friction coefficient, relative to DNS, during the onset of laminar-turbulent transition. This section is adapted from Sleeman et al. (2024a). We further note that Fasel et al. (1990) and Rist and Fasel (1995) have previously compared their DNS results to experimental results in the literature. Since we are applying NOWNS to these DNS cases, we forego discussions of experimental results and refer to Fasel et al. (1990) and Rist and Fasel (1995).

5.1 K-type transition

For K-type transition, we use the blowing/suction function specified in (3.31), which corresponds to the function used in Rigas et al. (2021) and Rist and Fasel (1995). However, to match the calculations of Sayadi et al. (2013), we modify the parameters such that $Re_x(x_1) = 1.36 \times 10^5$, $Re_x(x_2) = 1.56 \times 10^5$, $F = 110 \times 10^{-6}$ and $b = 0.419 \times 10^{-3}$ to match Sayadi et al. (2013). We further choose $M = 4$ temporal modes and $N = 8$ spanwise modes, with 1,300 stations over the streamwise domain $Re_x \in [1.36 \times 10^5, 2.73 \times 10^5]$, and 100 grid points in the wall-normal direction for $y \in [0, 60]$.

Figure 5.1 shows excellent agreement between the u' amplitudes of NOWNS and the DNS Sayadi et al. (2013), where the gray strip denotes the blowing/suction strip. Recall that we refer to modes according to their temporal frequency and their spanwise wave number as (m, n), where m refers to the frequency $\omega_m = m\omega$ and n refers to the spanwise wave number $\beta_n = n\beta$, while the amplitudes are

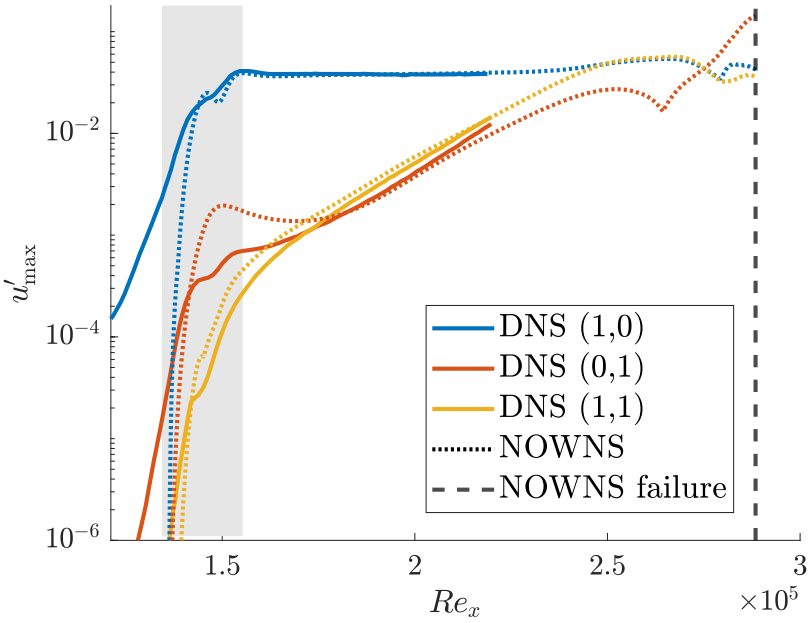

Figure 5.1: u'-velocity amplitudes for K-type transition, compared to the DNS of Sayadi et al. (2013).

defined as (3.30). We note that in the early stages of the march there is disagreement between the DNS and NOWNS calculations because the blowing/suction strip causes upstream effects that NOWNS neglects by construction. However, these disturbances are convective in nature, and the amplitudes predicted by NOWNS rapidly converge to those predicted by DNS as the march progresses downstream. We also note that Sayadi et al. (2013) do not plot the u' amplitudes for the entire streamwise domain, which is why the NOWNS amplitudes extend farther downstream. Figure 5.2 shows the u-velocity contours at $y/\delta_{\text{inlet}} = 0.6$, as in Sayadi et al. (2013). We observe the aligned Λ-vortex structure that is characteristic of K-type transition, and good qualitative agreement with Sayadi et al. (2013).

5.2 H-type transition

For H-type transition we use the blowing/suction strip function

$$f(x,z,t) = 1.5\times10^{-3}\sin(2\omega t)v_a(x) + 1.5\times10^{-5}\sin(\omega t)\cos(\beta z)v_a(x), \quad (5.1)$$

where for $v_a(x)$ defined in (3.31b). We choose $Re_x(x_1) = 1.65\times10^5$ and $Re_x(x_2) = 1.81\times10^5$, with $2F = 124\times10^{-6}$ and $b = 0.419\times10^{-3}$. To match the parameters of Sayadi et al. (2013), we choose $M = 8$ temporal modes and $N = 14$ spanwise modes, with 2,370 stations over the streamwise domain $Re_x \in [1.65\times10^5, 5.16\times10^5]$, and 100 grid points in the wall-normal direction for $y \in [0, 60]$. As in the

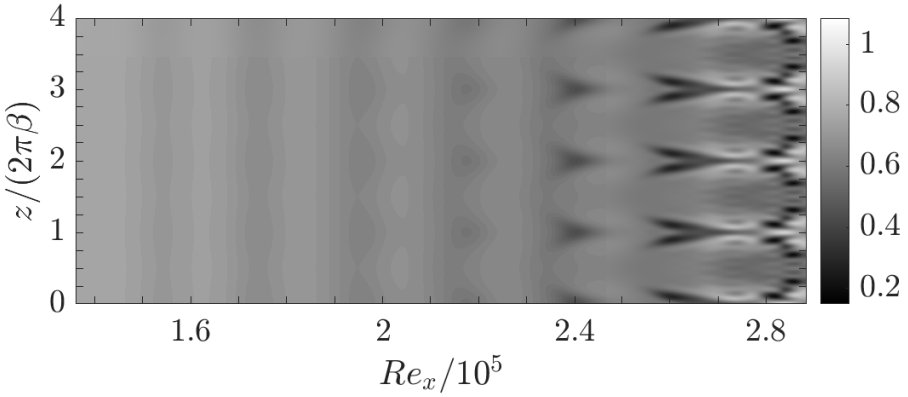

Figure 5.2: u-velocity contours at $y/\delta_{\text{inlet}} = 0.6$ for K-type transition, demonstrating the aligned Λ-vortex structure.

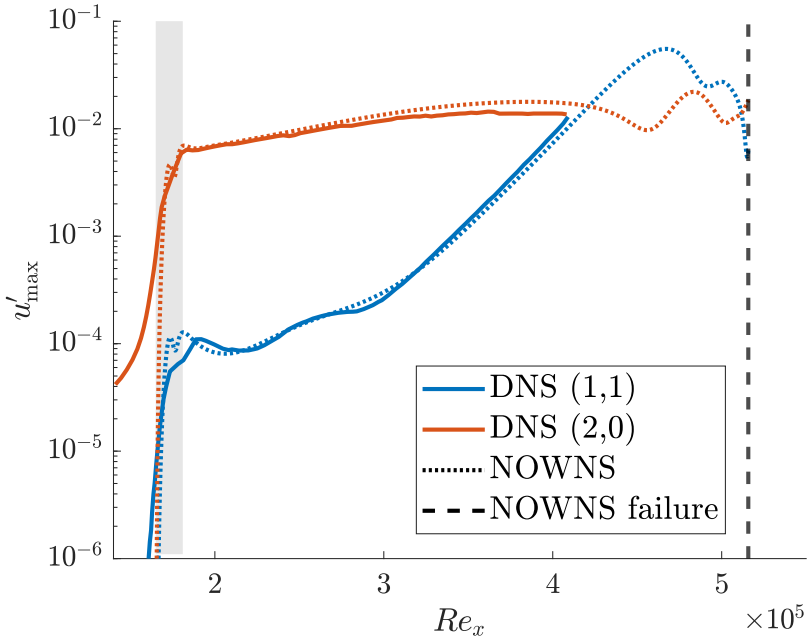

Figure 5.3: u'-velocity amplitudes for H-type transition, compared to the DNS of Sayadi et al. (2013).

K-type transition case, Figure 5.3 demonstrates that the amplitudes predicted by NOWNS agree well with those from DNS, for the streamwise domain where DNS results are available, while Figure 5.4 demonstrates the staggered Λ-vortex structure characteristic of H-type transition.

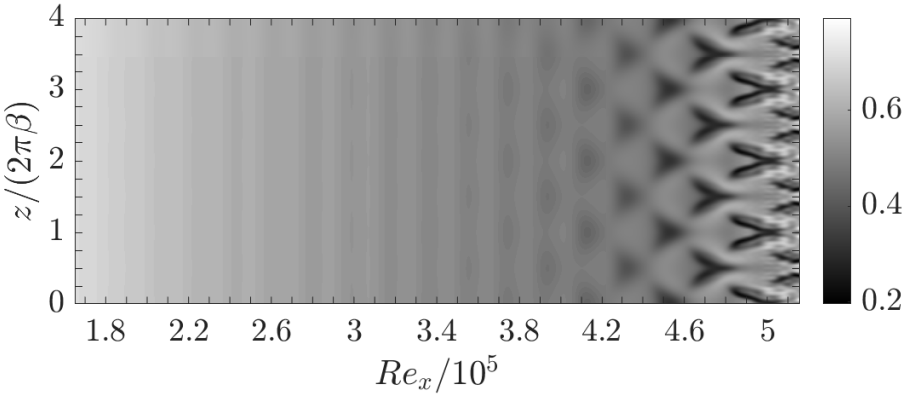

Figure 5.4: u-velocity contours at $y/\delta_{\text{inlet}} = 0.6$ for H-type transition, demonstrating the staggered Λ-vortex structure.

5.3 Skin friction

Boundary-layer transition is characterized by a rapid rise of the skin friction drag. We will measure the skin friction drag using the dimensionless skin-friction coefficient

$$C_f = \frac{\tau_w^*}{\frac{1}{2}(U_\infty^*)^2/\nu_\infty^*}, \quad \tau_w^* = \mu^* \frac{\partial u^*}{\partial y^*},$$

where τ_w^* is the wall shear stress. We rewrite this in terms of the dimensionless variables as

$$C_f = \frac{2\nu_\infty^*}{(U_\infty^*)^2}\mu^* \frac{\partial u^*}{\partial y^*} = 2\frac{\nu_\infty^*\mu^*}{\delta_0^* U_\infty^*}\frac{\partial u}{\partial y} = 2\mu\frac{\nu_\infty^*\mu_\infty^*}{U_\infty^*}\sqrt{\frac{U_\infty^*}{x_0^*\mu_\infty^*\nu_\infty^*}}\frac{\partial u}{\partial y} = \frac{2\mu}{\sqrt{Re_x(x_0)}}\frac{\partial u}{\partial y},$$

so that from NOWNS we obtain the time- and spanwise-averaged skin friction coefficient as

$$C_{f,\text{ave.}} = \frac{1}{T}\frac{1}{2\pi\beta}\int_{t+T}^{t}\int_{z}^{z+1/(2\pi\beta)} \frac{2\mu}{\sqrt{Re_x(x_0)}}\frac{\partial u}{\partial y}\mathrm{d}\bar{z}\mathrm{d}\bar{t} = \frac{2\mu(\bar{T}+\hat{T}_{00})}{\sqrt{Re_x(x_0)}}\frac{\partial[\bar{u}+\hat{u}_{00}]}{\partial y}.$$

Next, the laminar value can be obtained from the Blasius solution, while we use the turbulent correlation from White (2006). In summary, we plot the following skin friction coefficients:

$$C_{f,\text{ave.}} = \frac{2\mu(\bar{T}+\hat{T}_{00})}{\sqrt{Re_x(x_0)}}\frac{\partial[\bar{u}+\hat{u}_{00}]}{\partial y}, \quad C_{f,\text{lam.}} = \frac{0.664}{\sqrt{Re_x}}, \quad C_{f,\text{turb.}} = \frac{0.455}{\ln^2(0.06Re_x)}.$$

Figure 5.5 compares these values against the DNS values from Sayadi et al. (2013), and we see that for both H- and K-type transition NOWNS correctly predicts the initial rise in the skin friction coefficient, but following the initial rise, the NOWNS

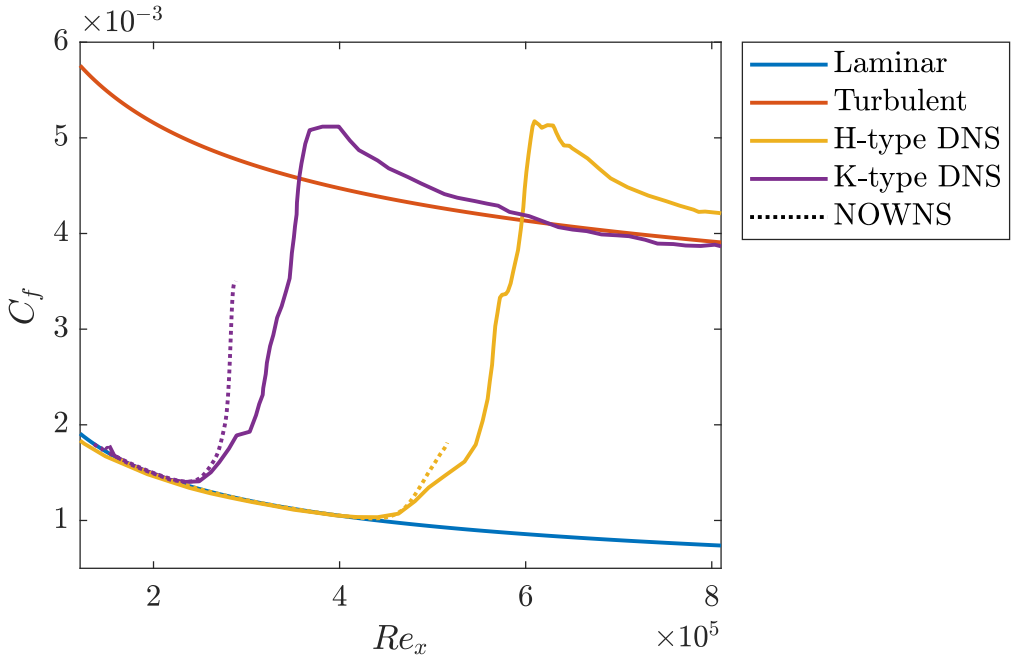

Figure 5.5: Skin friction coefficient for K- and H-type transition, compared to the DNS of Sayadi et al. (2013).

predicts a much more rapid growth than DNS, before eventually failing. When we say the NOWNS march fails, we mean that the Newton solver fails to converge to the desired error tolerance.

Transition is characterized by a rise in skin friction coefficient, in which it initially overshoots the turbulent correlation, before converging to this value downstream (see Figure 5.5). If NOWNS overshot the turbulent value before failing, we could likely say that it predicted transition. However, NOWNS fails before reaching this value, so it is not clear when we can say that it predicts transition.

5.4 Investigations into the failure of the NOWNS march

We discuss the root cause of NOWNS' failure, separating errors into modeling and discretization errors. We also note that we say that NOWNS fails when the Newton's method fails to converge. However, it becomes inaccurate before it fails, since the skin friction coefficient no longer agrees with the value predicted by DNS. Even if we modified the nonlinear solution method so it continued to converge, it would be inaccurate.

5.4.1 Discretization errors

Section 1.4.3 discusses PSE's minimum step-size requirement, which prevents it from properly resolving all streamwise length scales, while also making it more challenging for the nonlinear solver to converge. NOWNS does not have this minimum step-size requirement, yet it still becomes inaccurate following the onset of transition, before eventually failing (the Newton solver does not converge to the desired error tolerance). This suggests that the minimum step-size requirement is not necessarily the root cause of NPSE's failure, since taking arbitrarily small steps using NOWNS still leads to failure.

To ensure that the failure is not due to a lack of resolution, we doubled the resolution in x, y, M, and N, and we found that the results did not change substantially. We also performed the calculation without enforcing symmetry in z, and again found that the result did not change substantially. Prior to the development of the greedy algorithm (see Chapter 4), we were concerned that the recursion parameters were not properly tuned following the onset of transition, since they were originally developed for a Blasius profile. However, the greedy algorithm allows us to automatically choose recursion parameters that achieve any desired error tolerance, even following the onset of transition. Increasing N_β does not change the results substantially, so that recursion parameter selection is also not likely the root cause of failure.

5.4.2 Modeling errors in NOWNS

Proposition 2.2.10 shows that the linear OWNS approach can evolve the upstream- and downstream-going modes independently of each other, and recover the global solution as the sum of the upstream- and downstream-going solutions. However, this property is lost for the nonlinear equations, since we lose the effect of the upstream-going solution on the nonlinear term:

$$PF(\hat{\boldsymbol{\phi}}' + \hat{\boldsymbol{\phi}}'') \neq PF(\hat{\boldsymbol{\phi}}').$$

If $\|P[F(\hat{\boldsymbol{\phi}}' + \hat{\boldsymbol{\phi}}'') - F(\hat{\boldsymbol{\phi}}')]\|$ is small, then we expect NOWNS to be accurate, while it becomes less accurate as this term becomes larger.

The 3D Euler equations have characteristics $\bar{u}$, $\bar{u}$, $\bar{u}$, $\bar{u} - \bar{c}$, and $\bar{u} + \bar{c}$. For a subsonic boundary-layer flow, we have $\bar{u} > 0$ and $\bar{u} < \bar{c}$, so that

$$\bar{u}, \bar{u}, \bar{u}, \bar{u} + \bar{c} > 0, \quad \bar{u} - \bar{c} < 0.$$

The OWNS approach removes upstream-going modes associated with $\bar{u} - \bar{c}$, which is a modeling error, since the NOWNS model is not consistent with flow it is

trying to model. It is possible that modes associated with this characteristic are important following the onset of transition, and that NOWNS cannot be accurate since it neglects these upstream-going modes, which is a limitation of one-way spatial-marching.

In linear OWNS, we linearize the projection operator about the base flow, $\bar{\boldsymbol{q}}$. In contrast, for nonlinear OWNS we have the choice to linearize about either the base flow or the corrected mean flow, $\bar{\boldsymbol{q}} + \hat{\boldsymbol{q}}'_{00}$. Appendix G.4 compares these two approaches for K-type transition and finds that it does not substantially affect the calculation. However, the mean flow distortion calculated by NOWNS neglects upstream effects by construction, which represents a modeling error. Therefore, it is possible that the results would change more substantially if we linearized about the mean flow computed using a global solver.

5.4.2.1 Negative upstream streamwise velocity

For Blasius boundary layers, the u-velocity is downstream-going throughout the whole domain, so that $\bar{u} > 0$ everywhere. In nonlinear calculations, we must also consider the corrected mean flow, $\bar{u} + \hat{u}'_{00}$, which arises due to nonlinear interactions of the mean flow distortion, $\hat{u}'_{00}$, with the base flow. For the cases considered in this work, we find that the corrected mean flow is also downstream-going throughout the whole domain, $\bar{u} + u'_{00} > 0$, but that the flow can instantaneously have a negative u-velocity, $\bar{u} + u' < 0$. For the 2D high-amplitude TS wave evolution from Section 3.4.1, as well as the H- and K-type transition scenarios considered here, we find that the negative u-velocity precedes the failure of the NOWNS march.

For the 2D case from Section 3.4.1, we find that NOWNS is able to (accurately) march farther downstream than NSPE before failing. In Section 3.4.2, we also applied NOWNS to a large-amplitude oblique-wave breakdown case where NPSE fails. We found that although NOWNS is not accurate compared to DNS, it is able to march farther downstream than NPSE, and does not fail. We further note that no negative u-velocity is observed for this case. It appears that the failure of the NOWNS march is correlated with instantaneous u-velocities.

5.5 Summary

We have demonstrated that NOWNS accurately simulates the early stages of transition by matching the u-velocity amplitudes predicted by DNS, while correctly predicting the initial rise in the skin friction coefficient, showing that NOWNS can

be used to predict transition onset analytically. Our investigation into the cause of NOWNS' failure suggests that it is due to a modeling error, since NOWNS neglects upstream effects by construction. Future work should develop a criterion with which to predict transition using NOWNS, and should consider potential modifications to the routine such that it can march farther downstream while matching accurately DNS results.

Chapter 6

NOWNS FOR STABILITY AND TRANSITION ANALYSIS OF HIGH-SPEED BOUNDARY-LAYER FLOWS

This chapter presents the extension of NOWNS to high-speed flows, along with a demonstration of the greedy algorithm from Chapter 4, and some of the results are adapted from Sleeman and Colonius (2025).

High-speed boundary-layer transition is challenging to study experimentally using wind and shock tunnel measurements because of the high noise levels (Schneider, 2001), while they are not necessarily representative of flight tests because free-stream fluctuations introduce higher amplitude disturbances than those typically experienced in flight. Quiet tunnels can relieve some of these problems, but are limited by the Reynolds number they can achieve. Therefore, NOWNS could be a valuable tool for studying transition mechanisms in high-speed flows.

6.1 Governing equations

Whereas for low-speed flows we performed our analysis in terms of the primitive variables $(\nu, \boldsymbol{u}, p)$, for high-speed flows we will instead use $(\rho, \boldsymbol{u}, T)$, as was done in (Kamal, 2023). The non-dimensional compressible Navier-Stokes equations for an ideal gas can be written as

$$\frac{\partial \rho}{\partial t} + \nabla \cdot (\rho \boldsymbol{u}) = 0, \tag{6.1a}$$

$$\rho \frac{D\boldsymbol{u}}{Dt} + \nabla p = \frac{1}{Re} \nabla \cdot \tau, \tag{6.1b}$$

$$\rho c_p \frac{DT}{Dt} - \frac{Dp}{Dt} = \frac{1}{PrRe} \nabla \cdot \big(k(T) \nabla T\big) + \frac{1}{Re} \tau : \nabla \boldsymbol{u}, \tag{6.1c}$$

for the stress tensor (1.1e). We assume that Pr and c_p are constant, while μ is a function of temperature according to Sutherland's law

$$\mu^*(T^*) = \mu^*_\infty \left(\frac{T^*}{T^*_\infty} \right)^{3/2} \frac{T^*_\infty + S^*}{T^* + S^*}, \tag{6.2}$$

where $S^* = 110.4\text{K}$, so that $k^*_\infty(T) = \mu^*(T) c^*_p / Pr$.

6.2 Demonstration of greedy algorithm for high-speed flows

We consider the Mach 4.5 boundary-layer flow over an adiabatic flat plate studied by Ma and Zhong (2003), which was used by Zhu and Towne (2023) as a validation

case for the OWNS-R formulation. The flow conditions are $M_\infty = 4.5$, $T^*_\infty = 65.15$ K, $p^*_\infty = 728.44$ Pa, $Pr = 0.72$, and unit Reynolds number $Re^*_\infty = \rho^*_\infty U^*_\infty / \mu^*_\infty = 7.2 \times 10^6 /$ m.

6.2.1 Error convergence at the domain inlet

First we compare the greedy and heuristic approaches at $Re_x = 5.625 \times 10^3$, where Figure 6.1 shows the convergence of the error as a function of N_β for OWNS-P and OWNS-R. We again observe that OWNS-P achieves machine zero error, while OWNS-R does not. We also highlight that for OWNS-R only, we excluded downstream-going eigenvalues with $\alpha_i > 100$ from the selection procedure, which improves the accuracy of the approximation. Excluding these modes does not significantly affect the accuracy of the approximation because they decay rapidly. We also note that heuristic parameter selection does a better job of capturing Mack's second mode (MM), which is the dominant instability for high-speed boundary-layer flows. For low-speed flows, the eigenvalue associated with the TS wave is far (in the complex plane) from the rest of the eigenvalues of M, while for high-speed flows, MM is close to the other eigenvalues. Therefore, the greedy algorithm does not choose MM as a recursion parameter, explaining the slower convergence. In contrast, Kamal (2023) places the heuristic recursion parameters such that many are clustered near MM. As described in Remark 4.1.1, the user could specify MM as an eigenvalue to track, improving the performance of the greedy approach.

6.2.2 Linear calculation for Mack's second mode

We use OWNS with greedy and heuristic recursion parameter selection to perform a linear stability calculation of Mack's second mode over the streamwise domain $Re_x \in [5.625, 12.1] \times 10^5$ with $N_x = 4,500$ streamwise stations. We compute the N-factor based on the temperature disturbance and find that the greedy approach leads to a cost increase relative to heuristic recursion parameter selection.

The reference solution is the greedy OWNS-P calculation with $N_\beta = 20$, and table 6.1 shows that heuristic recursion parameter selection generally converges with fewer recursion parameters, which is consistent with our observations in section 6.2.1 that the error in Mack's second mode converges more quickly using heuristic, rather than greedy, parameter selection. Although greedy selection will generally achieve faster

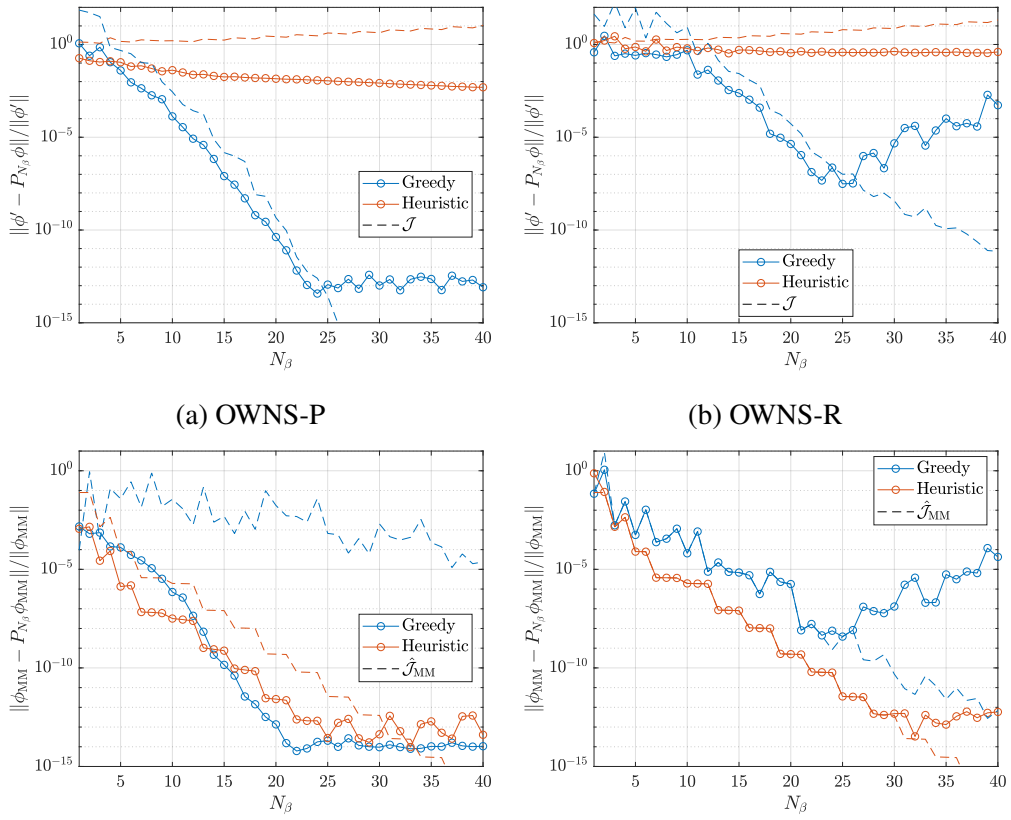

(a) OWNS-P

(b) OWNS-R

(c) OWNS-P, MM only

(d) OWNS-R, MM only

Figure 6.1: Convergence of the error for greedy and heuristic parameter selection for 2D high-speed boundary-layer flow.

	N_β			Speed-up		
Error	P-H	P-G	R-G	P-H	P-G	R-G
10%	1	6	17	1.0	0.34	0.83
1%	1	6	21	1.0	0.34	0.83
0.1%	2	7	22	1.0	0.32	0.82

Table 6.1: Speed-up achieved by using greedy parameter selection with OWNS-P (P-G) and OWNS-R (R-G) relative to heuristic parameter selection with OWNS-P (P-H) for different relative errors in the N-factor for the 2D high-speed boundary-layer flow.

convergence, heuristic selection can be better when parameters are carefully chosen. We note that if the greedy algorithm is initialized with Mack's second mode, then it also converges with $N_\beta = 1$ for OWNS-P.

6.3 Extension of NOWNS to high-speed flows

Kamal et al. (2020) extended linear OWNS from low- to high-speed boundary-layer

flows, and we follow a similar procedure for NOWNS.

6.3.1 Temperature-dependent fluid properties

For the low-speed flows discussed in Chapters 3, 4, and 5, we assumed that the fluid properties were constant, while they are function of temperature for high-speed flows. Let $\Phi(T)$ denote a temperature-dependent fluid property, where $T = \bar{T} + T'$. In linear OWNS we take a Taylor series expansion about $\bar{T}$ and discard all terms higher than linear order to obtain

$$\Phi(T) = \Phi(\bar{T}) + \left.\frac{\partial \Phi}{\partial T}\right|_{T=\bar{T}} T' + O(T'^2). \tag{6.3a}$$

However, we wish to retain these terms in NOWNS, so we instead write

$$\Phi(T) = \Phi(\bar{T}) + \left.\frac{\partial \Phi}{\partial T}\right|_{T=\bar{T}} T' + \Phi'(\bar{T}, T'), \tag{6.3b}$$

for

$$\Phi'(\bar{T}, T') = \Phi(\bar{T} + T') - \Phi(\bar{T}) - \left.\frac{\partial \Phi}{\partial T}\right|_{T=\bar{T}} T'. \tag{6.3c}$$

As an example, we consider the quadratic product

$$\begin{aligned}(\bar{\boldsymbol{q}} + \boldsymbol{q}') \times \Phi(\bar{T} + T') = \underbrace{\bar{\boldsymbol{q}} \times \Phi(\bar{T})}_{\text{Discarded terms}} &+ \underbrace{\boldsymbol{q}' \times \Phi(\bar{T}) + \bar{\boldsymbol{q}} \times \left.\frac{\partial \Phi}{\partial T}\right|_{T=\bar{T}} T'}_{\text{Linear terms}} \\ &+ \underbrace{\bar{\boldsymbol{q}} \times \Phi'(\bar{T}, T') + \boldsymbol{q}' \times \left[\left.\frac{\partial \Phi}{\partial T}\right|_{T=\bar{T}} T' + \Phi'(\bar{T}, T')\right]}_{\text{Nonlinear terms}},\end{aligned}$$

where terms without a disturbance variable are discarded (the baseflow satisfies the governing equations), while terms that are higher than first-order in the disturbance variables are used only by nonlinear OWNS. Therefore, in the nonlinear calculation (after simplification), we write

$$\begin{aligned}(\bar{\boldsymbol{q}} + \boldsymbol{q}') \times \Phi(\bar{T} + T') = &\underbrace{\boldsymbol{q}' \times \Phi(\bar{T}) + \bar{\boldsymbol{q}} \times \left.\frac{\partial \Phi}{\partial T}\right|_{T=\bar{T}} T'}_{\text{Linear terms}} \\ &+ \underbrace{\bar{\boldsymbol{q}} \times \Phi'(\bar{T}, T') + \boldsymbol{q}' \times [\Phi(T) - \Phi(\bar{T})]}_{\text{Nonlinear terms}}.\end{aligned} \tag{6.4}$$

We can simplify further to obtain

$$(\bar{\boldsymbol{q}} + \boldsymbol{q}') \times \Phi(\bar{T} + T') = \boldsymbol{q}' \times \Phi(\bar{T}) + [\bar{\boldsymbol{q}} + \boldsymbol{q}'] \times [\Phi(T) - \Phi(\bar{T})], \tag{6.5}$$

which matches the expression commonly employed in high-speed NPSE (Chang et al., 1993; Chang and Malik, 1994).

6.3.2 Linearizing about the corrected mean flow

In Chapter 3, we presented NOWNS for projection operators linearized about the base flow, $\bar{\boldsymbol{q}}$. In Appendix G.4, we compared results for low-speed K-type transition linearized about the base flow, $\bar{\boldsymbol{q}}$, and the corrected mean flow, $\bar{\boldsymbol{q}} + \hat{\boldsymbol{q}}_{00}$, and we found that the difference was not substantial. However, we might expect the difference to be more pronounced for high-speed flows because the number of upstream- and downstream-going modes can be different for $\bar{\boldsymbol{q}}$ and $\hat{\boldsymbol{q}}_{00}$, as explained below.

The number of upstream- and downstream-going modes are determined by the characteristics of $A(\bar{\boldsymbol{q}})$

$$\bar{u}, \bar{u}, \bar{u}, \bar{u} - \sqrt{\gamma R_g \bar{T}}, \bar{u} + \sqrt{\gamma R_g \bar{T}},$$

or $A(\bar{\boldsymbol{q}} + \hat{\boldsymbol{q}}_{00})$

$$\bar{u} + \hat{u}_{00}, \bar{u} + \hat{u}_{00}, \bar{u} + \hat{u}_{00}, \bar{u} + \hat{u}_{00} - \sqrt{\gamma R_g (\bar{T} + \hat{T}_{00})}, \bar{u} + \hat{u}_{00} + \sqrt{\gamma R_g (\bar{T} + \hat{T}_{00})}.$$

For the low-speed flows considered in this work, the characteristics of $A(\bar{\boldsymbol{q}})$ and $A(\bar{\boldsymbol{q}} + \hat{\boldsymbol{q}}_{00})$ have the same signs, since $\bar{u}$ and $\hat{u}_{00}$ have the same sign and $\hat{T}_{00}$ is small. In contrast, for high-speed flows, $\hat{T}_{00}$ can grow large, so that

$$\operatorname{sign}(\bar{u} - \sqrt{\gamma R_g \bar{T}}) \neq \operatorname{sign}(\bar{u} + \hat{u}_{00} - \sqrt{\gamma R_g (\bar{T} + \hat{T}_{00})}).$$

Therefore, the base flow and corrected mean flow will have different numbers of upstream- and downstream-going modes, and we might expect that linearizing about the corrected mean flow instead of the base flow will have a larger impact than in the low-speed cases. However, we find again that the difference between linearizing about $\bar{\boldsymbol{q}}$ and $\hat{\boldsymbol{q}}_{00}$ is negligible for high-speed flows.

6.3.3 Disturbance amplitude

Whereas for low-speed flows we have measured disturbance amplitude in terms of the u-velocity, we will instead measure it in terms of the temperature as

$$T'^{(m,n)}_{\max}(x) = \frac{c_{m,n}}{T_\infty} \max_y |T'_{m,n}(x, y)|, \tag{6.6a}$$

for

$$c_{m,n} = \begin{cases} 1 & m = n = 0, \\ \sqrt{2} & m = 0, n \neq 0;\ n = 0, m \neq 0, \\ 2 & \text{otherwise.} \end{cases} \tag{6.6b}$$

6.4 2D nonlinear evolution of Mack's second mode

We make the calculation from 6.2.2 nonlinear by specifying that Mack's second mode has an amplitude of 10% based on the temperature disturbance, relative to the free-stream value, while we truncate the Fourier series at $M = 10$, with $N_\beta = 12$ recursion parameters chosen using the greedy algorithm. We plot the temperature disturbance amplitudes for both the linear and nonlinear OWNS calculations in Figure 6.2. We see that the two calculations initially match, but as the disturbances grow, the linear calculation exhibits larger growth of the fundamental disturbance, while the MFD grows substantially for the nonlinear calculation.

Figures 6.4a and 6.4b show that the heuristic parameter selection yields reasonable temperature profiles for the MFD and fundamental disturbance, respectively. However, Figures 6.4c and 6.4e show that there are non-physical grid effects present near the sonic line for heuristic parameter selection, while these are not present when greedy selection is used, as shown in Figures 6.4d and 6.4f. We additionally compare the temperature profiles at the domain outlet for the first and second harmonics of Mack's second mode in Figure 6.5. Although heuristic parameter selection outperforms greedy (in terms of computational cost) for the linear problem, the same set of heuristic parameters do not work in the nonlinear case. As discussed above, the high-speed heuristic recursion parameters have been tailored to track Mack's second mode, but they do so at the expense of the other modes, and this effect is noticeable for the higher harmonics in nonlinear calculations.

Figure 6.3 compares the amplitudes computed when linearized about the base flow to the amplitudes computed when linearized about the corrected mean flow. The results are nearly indistinguishable, but this may be due to the small disturbance amplitude.

6.5 Oblique breakdown of Mack's first mode

While TS waves are most unstable for $\beta = 0$, Mack's first and second modes are most unstable when $\beta \neq 0$, so we extend our analysis to 3D disturbances. 3D disturbances to Mach 6 flat-plate boundary-layer flows have been studied using DNS by Leinemann et al. (2021) and Franko and Lele (2013). Both studies introduce disturbances using a blowing/suction strip. Both groups investigated oblique breakdown of Mack's first mode and fundamental transition for Mack's second mode, while Franko and Lele (2013) additionally studied oblique breakdown of Mack's second

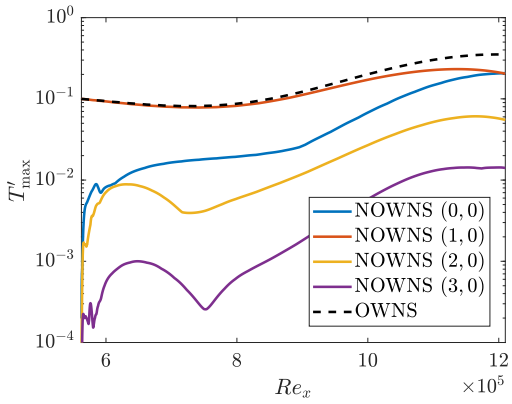

Figure 6.2: Temperature disturbance amplitudes for 2D nonlinear evolution of Mack's second mode for a Mach 4.5 flat-plate boundary-layer flow, computed using NOWNS and compared to linear OWNS.

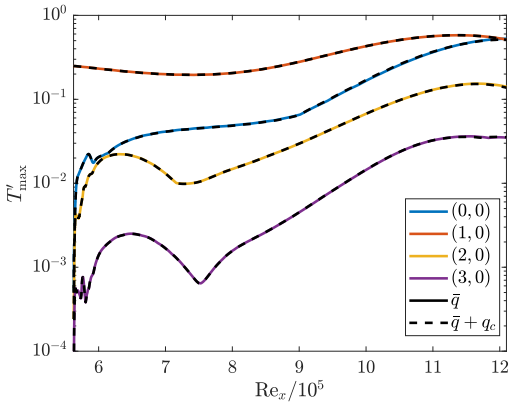

Figure 6.3: Comparison of temperature disturbance amplitudes for NOWNS calculation linearized about base flow and corrected mean flow for 2D nonlinear evolution of Mack's second mode for a Mach 4.5 flat-plate boundary-layer flow.

mode. We will use the conditions of Leinemann et al. (2021), where the free-stream Mach number is $M_\infty = 6$, the stagnation pressure and temperature are 956.3 kPa and 420 K, respectively, while the unit Reynolds number is $Re_\infty = 10.8224 \times 10^6$/ m. We assume the fluid to be a perfect gas with $\gamma = 1.4$, while we also assume a constant $Pr = 0.71$. The dynamic viscosity is computed according to Sutherland's law. Although both Leinemann et al. (2021) and Franko and Lele (2013) introduced disturbances using a blowing/suction strip, which NOWNS can do, we will introduce our disturbance using LST. The disturbance frequency is $f^* = 35$ kHz while the spanwise wavenumber is $\beta^* = 330/\mathrm{m}$. We use a fourth-order Padé-filter (Gaitonde and Visbal, 2000) with $\alpha_f = 0.3$ to remove numerical oscillations. Increasing the wall-normal resolution does not affect the solution substantially, indicating that we

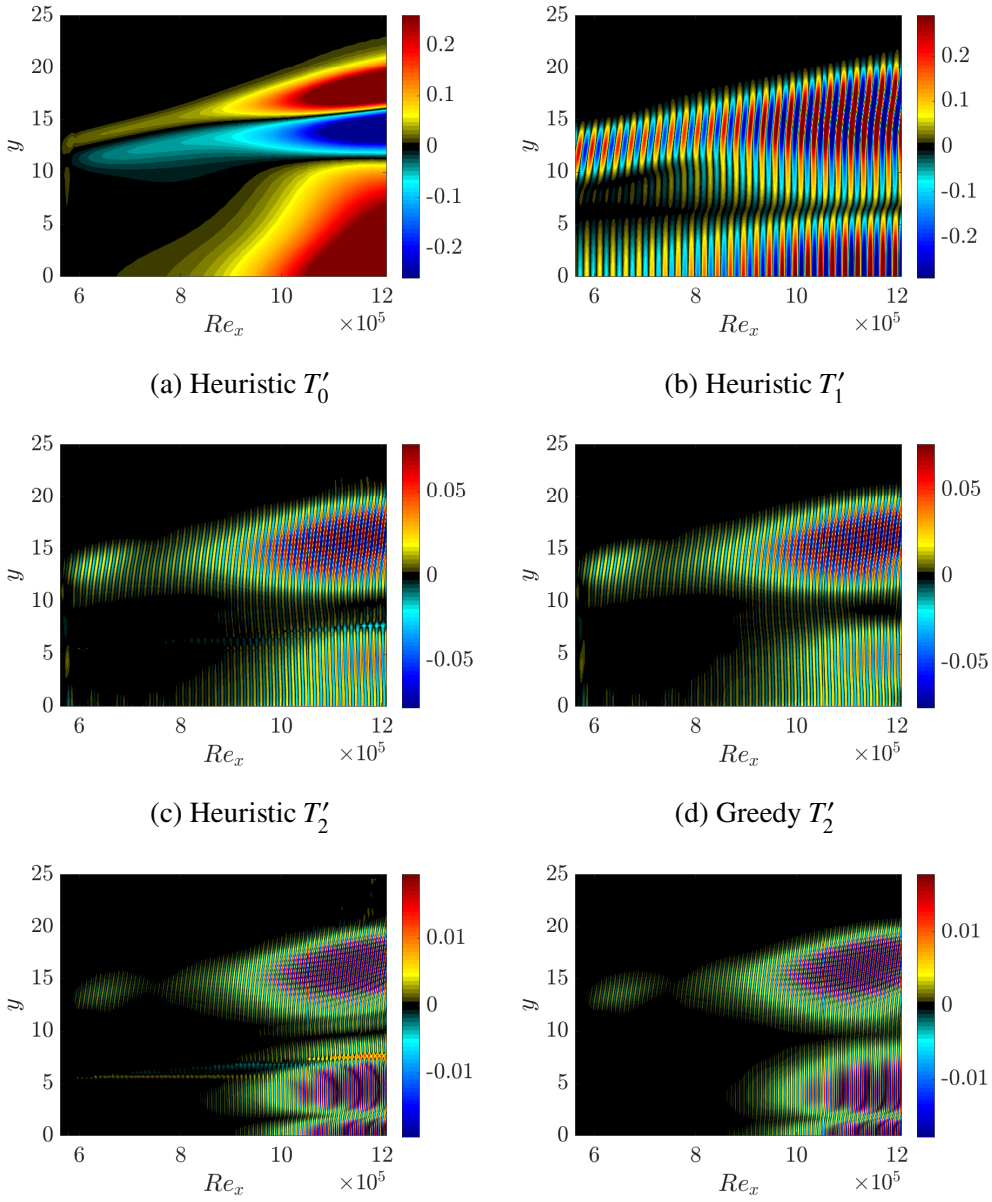

(a) Heuristic T_0'

(b) Heuristic T_1'

(c) Heuristic T_2'

(d) Greedy T_2'

(e) Heuristic T_3'

(f) Greedy T_3'

Figure 6.4: Temperature contours for first and second harmonic of Mack's second mode with heuristic and greedy recursion parameter selection.

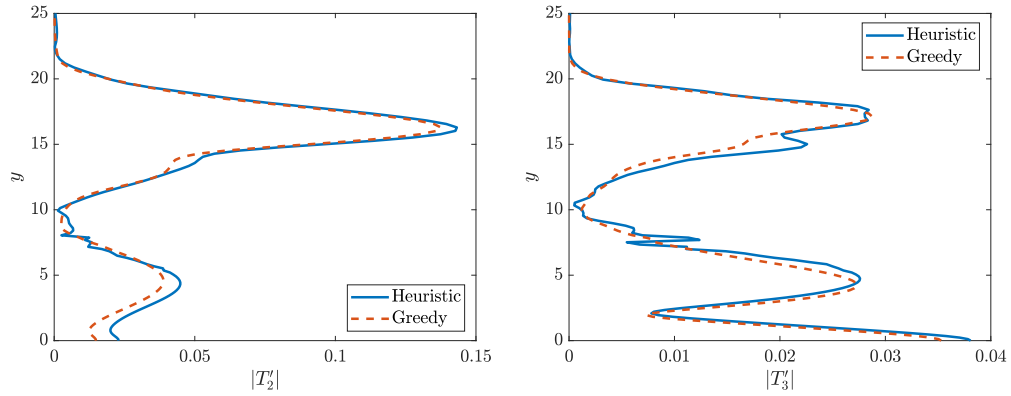

Figure 6.5: Temperature profiles at domain outlet for first and second harmonics of Mack's second mode with heuristic and greedy recursion parameter selection.

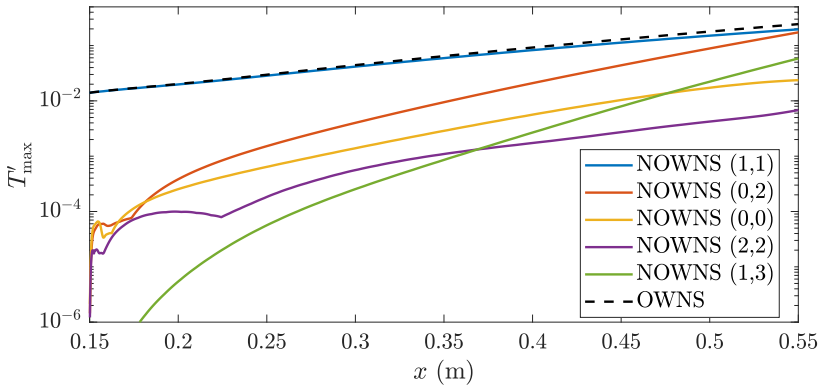

Figure 6.6: Temperature disturbance amplitudes for small amplitude oblique breakdown of Mack's first mode for Mach 6 flat-plate boundary-layer flow.

have enough grid-points to resolve all physically-relevant waves.

6.5.1 Small amplitude

We consider first a low-amplitude case, with an amplitude of 1.4% based on temperature. The domain is $x \times y \in [0.15\text{ m}, 0.55\text{ m}] \times [0\text{ m}, 0.025\text{ m}]$ with $N_x = 2,500$ and $N_y = 200$, while we $M = 3$ and $N = 4$ temporal and spanwise Fourier modes, respectively, with $N_\beta = 12$ recursion parameters chosen using the greedy algorithm. We plot the disturbance amplitudes in Figure 6.6, where we observe that the amplitude of the oblique wave grows more slowly in the nonlinear calculation, as compared to the linear calculation. Additionally, the vortex mode $(0, 2)$ grows to be the largest disturbance near the end of the domain. We find that the difference in linearizing about the corrected mean flow instead of the base flow is negligible, and so we do not compare the results.

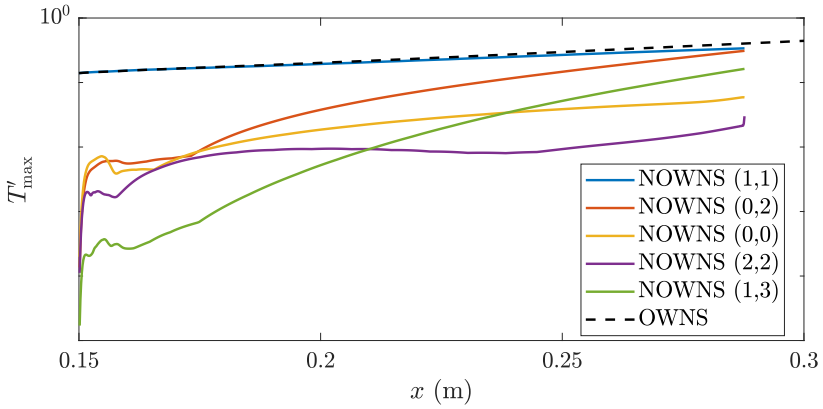

Figure 6.7: Temperature disturbance amplitudes for large amplitude oblique breakdown of Mack's first mode for Mach 6 flat-plate boundary-layer flow.

6.5.2 Large amplitude

We increase the amplitude to 14%, while we truncate the domain to $x \times y \in [0.15\text{ m}, 0.45\text{ m}] \times [0\text{ m}, 0.025\text{ m}]$ with $N_x = 2000$ and $N_y = 200$. We increase the number of Fourier modes to $M = N = 7$, while we maintain the same number of recursion parameters. We plot the temperature amplitudes in Figure 6.7, where we see again that the amplitude of the oblique wave grows more slowly in the nonlinear calculation, while the vortex mode $(0, 2)$ grows to be nearly the largest disturbance near the end of the march. We further note that the march fails at $x = 0.288$m, corresponding to station 919. We see from Figure 6.8 that the rise in the skin friction coefficient is small, indicating the transition has only just begun. Future work should explore why NOWNS fails so early into the transition process compared to the low-speed flows studied in Chapter 5. We also note that linearizing about the corrected mean flow instead of the base flow has a negligible impact on the solution.

6.6 Oblique breakdown of Mack's second mode

Mack's first mode is the dominant instability at lower frequencies, while Mack's second mode is dominant for higher frequencies. Leinemann et al. (2021) investigated fundamental transition of Mack's second mode for the same Mach 6 boundary-layer flow for which they investigated oblique breakdown of Mack's first mode, but with a frequency of $f^* = 95$ kHz and a spanwise wavenumber $\beta^* = 500/\text{m}$. Rather than study fundamental transition, we consider oblique breakdown of Mack's second mode. We use a fourth-order Padé-filter (Gaitonde and Visbal, 2000) with $\alpha_f = 0.3$ to remove numerical oscillations.

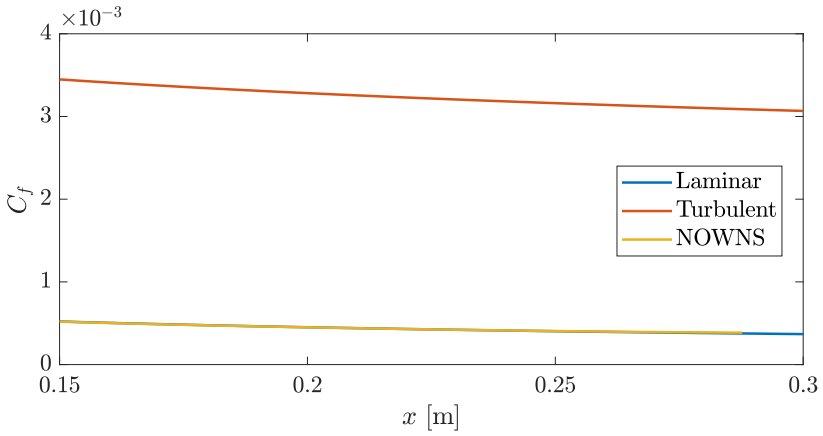

Figure 6.8: Skin friction coefficient for large amplitude oblique breakdown of Mack's first mode for Mach 6 flat-plate boundary-layer flow.

6.6.1 Small amplitude

We consider first a low-amplitude case, with an amplitude of 1.4% based on temperature. The domain is $x \times y \in [0.15\text{ m}, 0.55\text{ m}] \times [0\text{ m}, 0.025\text{ m}]$ with $N_x = 2,000$ and $N_y = 200$, while we $M = 3$ and $N = 4$ temporal and spanwise Fourier modes, respectively, with $N_\beta = 12$ recursion parameters chosen using the greedy algorithm. We plot the disturbance amplitudes in Figure 6.6, where we observe that the amplitude of the oblique wave grows more slowly in the nonlinear calculation, as compared to the linear calculation. Additionally, the vortex mode $(0, 2)$ grows to be the largest disturbance near the end of the domain. Note that NOWNS calculation is linearized about $\bar{\boldsymbol{q}} + \boldsymbol{q}_c$ instead of $\bar{\boldsymbol{q}}$. Figure 6.9 compares the linear calculation to the nonlinear calculation linearized about the corrected mean flow. We see that the vortex mode $(0, 2)$ becomes the largest disturbance, while the oblique wave has a smaller amplitude in the nonlinear calculation than in the linear calculation.

6.6.2 Large amplitude

We increase the amplitude to 14%, while we truncate the domain to $x \times y \in [0.15\text{ m}, 0.45\text{ m}] \times [0\text{ m}, 0.025\text{ m}]$ with $N_x = 2000$ and $N_y = 200$. We increase the number of Fourier modes to $M = N = 7$, while we maintain the same number of recursion parameters. We plot the temperature amplitudes in Figure 6.10, where we see again that the amplitude of the oblique wave grows more slowly in the nonlinear calculation, while the vortex mode $(0, 2)$ quickly overtakes the oblique wave to be the largest disturbance. We further note that the march fails at $x = 0.0.350$m, corresponding to station 1336. We see from Figure 6.11 that the rise in the skin

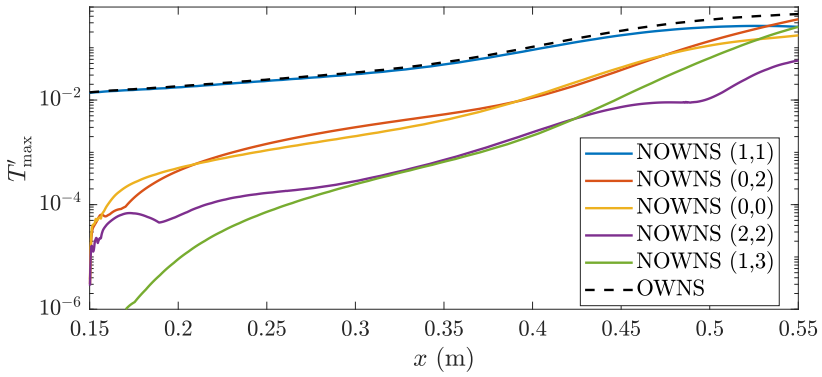

Figure 6.9: Temperature disturbance amplitudes for small amplitude oblique breakdown of Mack's second mode for Mach 6 flat-plate boundary-layer flow.

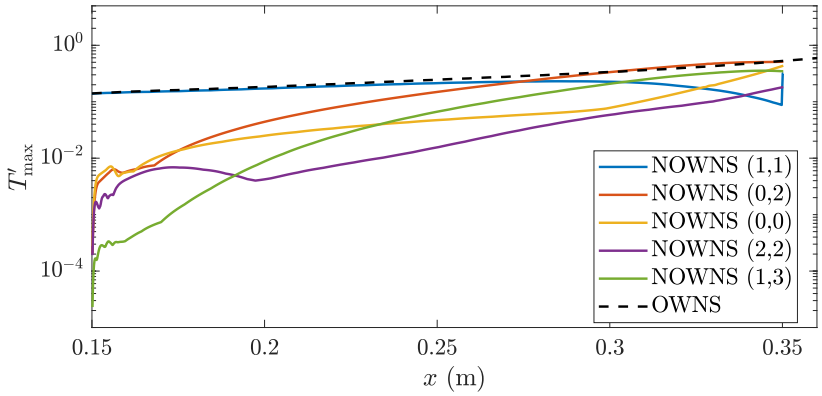

Figure 6.10: Temperature disturbance amplitudes for large amplitude oblique breakdown of Mack's second mode for Mach 6 flat-plate boundary-layer flow.

friction coefficient is larger than for the oblique breakdown of Mack's first mode in figure 6.8, but still smaller than the low-speed cases. We again find that linearizing about the corrected mean flow instead of the base flow has a negligible impact on the solution.

We plot the u-velocity contours in figure 6.12, where we observe that streaks associated with the $(0, 2)$ mode develop towards the end of the domain. Figure 6.13 plots the temperature contour in the $y - z$ plane at the domain outlet, while figure 6.14 plots the pressure contour in the symmetry plane and figure 6.15 plots the pressure contour at the wall.

6.7 Summary

We have demonstrated that greedy parameter selection works well for both linear and nonlinear calculations in high-speed boundary-layer flows. Although heuristic

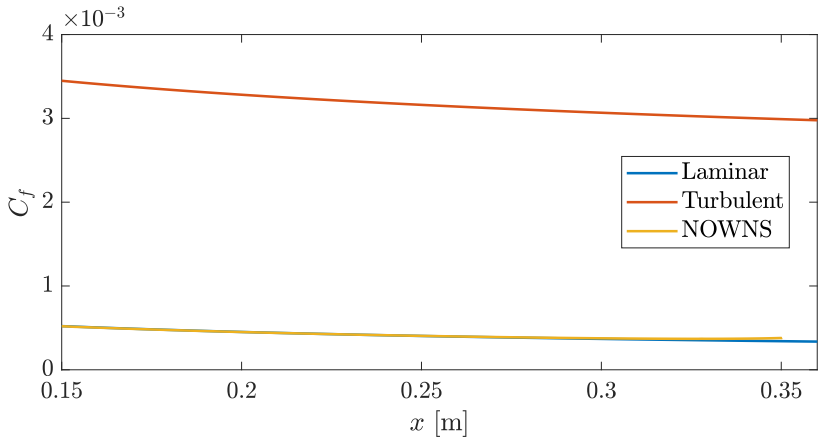

Figure 6.11: Skin friction coefficient for large amplitude oblique breakdown of Mack's second mode for Mach 6 flat-plate boundary-layer flow.

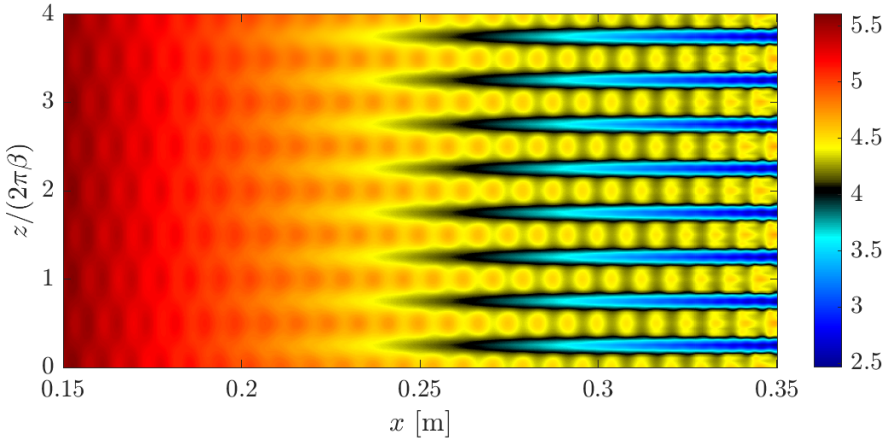

Figure 6.12: Contours of u-velocity at $y = 0.00189$m for oblique breakdown of Mack's second mode, exhibiting streaks towards the end of the domain

parameter selection outperforms greedy for tracking Mack's second mode in the linear calculation, greedy outperforms heuristic in the nonlinear calculation because other modes are introduced by the nonlinear term for the higher harmonics, and these are not properly evolved by the heuristic recursion parameters. In principle, it is possible to modify the heuristic parameters to enable accurate nonlinear calculations, but the greedy algorithm circumvents this problem by automatically choosing parameters that yield a rapidly convergent error in the OWNS approximation. We have demonstrated that NOWNS can be used to study the nonlinear evolution of Mack's first and second modes in high-speed boundary-layer flows, and we have compared results obtained when linearized about the base flow to results obtained

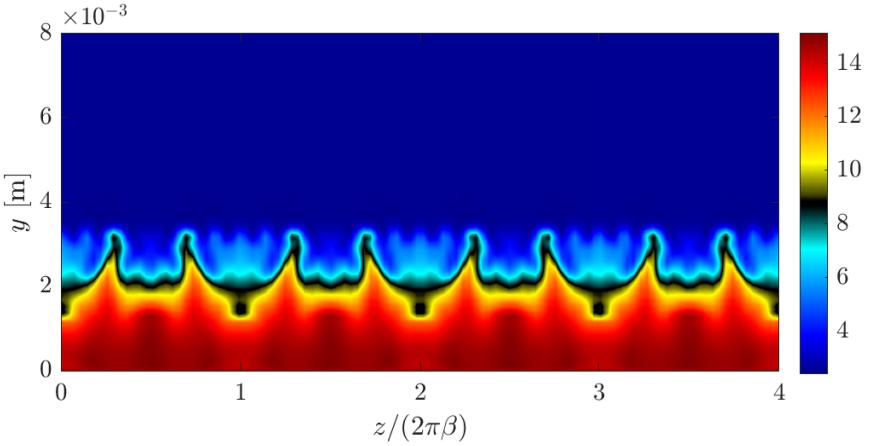

Figure 6.13: Temperature contours in the $y-z$ plane at the domain outlet for oblique breakdown of Mack's second mode.

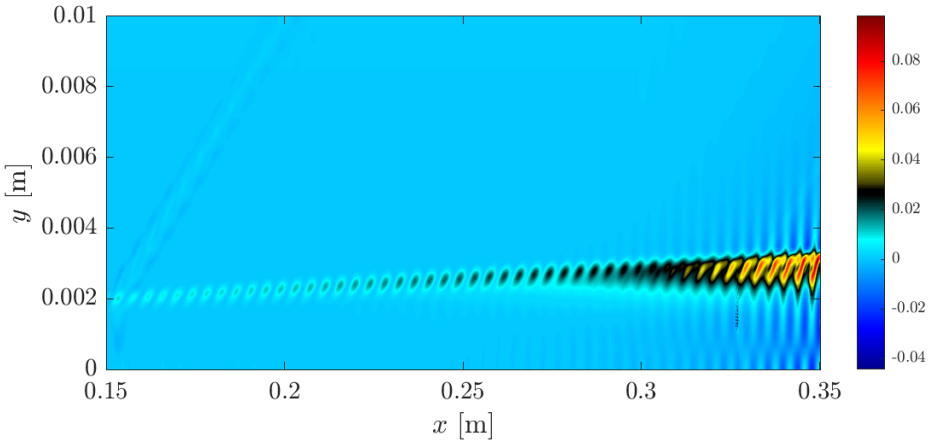

Figure 6.14: Pressure contours at $z = 0$ for oblique breakdown of Mack's second mode.

when linearized about the corrected mean flow. For both the oblique breakdown of Mack's first and second mode, the march fails before a significant rise in the skin friction coefficient occurs. Future work should attempt to modify the routine such that NOWNS can march farther into the transitional regime.

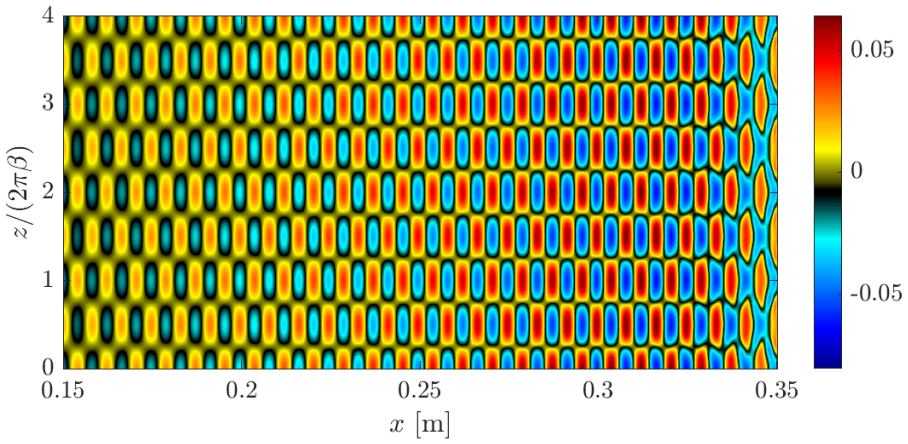

Figure 6.15: Pressure contours at $y = 0$ for oblique breakdown of Mack's second mode.

Chapter 7

CONCLUSIONS AND FUTURE WORK

7.1 Conclusions

This thesis developed the nonlinear One-Way Navier-Stokes (NOWNS) equations based on the OWNS projection (OWNS-P) approach. Chapter 1 provided background information on boundary-layer flows and methods for hydrodynamic stability analysis. Although linear methods can be used to predict transition in low-speed boundary-layer flows by combining them with an empirical correlation, this approach is less accurate for high-speed flows, particularly with complex geometries. In principle, laminar-turbulent transition can be predicted using DNS and LES, but these methods are limited by their high computational costs. NPSE is a low-cost alternative, but it fails for strong nonlinearities, is inaccurate for non-modal and multi-modal instabilities, and has a minimum step-size for numerical stability. In contrast NOWNS does not have a minimum step-size requirement and is accurate for non-modal and multi-modal instabilities, and succeeds for stronger nonlinearities than NPSE.

Chapter 2 introduced the OWNS-P (Towne et al., 2022) and OWNS-R (Zhu and Towne, 2023) approaches, while Chapter 3 developed NOWNS based on OWNS-P. We validated NOWNS against DNS for low-speed boundary-layer flows in cases where NPSE is already successful, and then we highlighted three strengths of NOWNS relative to NPSE:

1. It can handles larger disturbances than NPSE, although it also fails for sufficiently large disturbances.
2. It can handle large amounts of numerical noise, while NPSE fails.
3. It can handle arbitrary disturbances, such as those introduced using a blowing/suction strip, while NPSE requires the disturbances to specified as a (modal) inlet boundary condition.

The OWNS approximation relies on a recursive filter to remove upstream-going waves, which requires that recursion parameters be specified. Previous work has chosen these parameter heuristically, based on the Euler equations linearized about

a uniform flow. Chapter 4 develops a greedy algorithm for recursion parameter selection, which we demonstrate to have better convergence properties than the heuristic approach, leading to a new decrease in computational cost.

In Chapter 5 we demonstrate that for the H- and K-type transition scenarios commonly observed in low-speed boundary-layer flows, NOWNS is able to accurately predict the onset of transition, relative to DNS, before the march eventually fails. We do not believe this failure is due to discretization errors, and is instead due to modeling errors related to upstream effects which are removed (neglected) by construction.

Chapter 6 extends the NOWNS procedure to high-speed boundary layer flows and demonstrates the importance of the greedy algorithm for high-speed NOWNS. In particular, we show that heuristic parameter selection leads to a non-physical grid-effect along the sonic line. We further demonstrate that NOWNS has the potential to predict transition in high-speed boundary-layer flows by applying it oblique breakdown of Mack's first and second modes for a Mach 6 isothermal flat-plate boundary-layer flow.

7.2 Future Work

The results from this thesis suggest several avenues for future work on nonlinear disturbance evolution using NOWNS.

7.2.1 Transition prediction

We have developed and validated NOWNS for low-speed flows, showing that it can accurately predict transition onset. While DNS predicts an overshoot of the turbulent correlation, followed by agreement with the turbulent correlation, NOWNS fails before this can occur. Therefore, future work should develop a criterion to enable NOWNS to predict transition without skin-friction overshoot. Alternatively, NOWNS should be modified so that it can march far enough downstream to observe skin-friction overshoot.

7.2.2 High-speed boundary-layer flows

High-speed flows are characterized by multi-modal disturbances with short wavelengths and long streamwise domains over which they are unstable, so that NOWNS is well-suited to study these disturbances. Therefore, NOWNS should be validated for high-speed boundary-layer flows and applied to study realistic flight geometries, such as the HiFIRE-5 flight vehicle. In particular, it should be used to study

stationary and traveling crossflow vortices. Moreover, it should be used to identify optimal (worst-case) disturbances for high-speed boundary-layer flows in a multi-fidelity optimization framework, where NOWNS is used as a low-fidelity model to be queried rapidly, while a high-fidelity model (such as DNS/LES) is used to ensure accuracy.

7.2.3 Recursion parameter selection

In our initial work to extend NOWNS to high-speed flows, we observed non-physical grid-like effects along the sonic line, which we eliminated using the greedy algorithm. In principle, it is possible to choose heuristic recursion parameters such that the grid-like effects disappear, which should be another focus of future work. In addition, the recursion parameters chosen by the greedy algorithm could be used as a guide for choosing better recursion parameters using the heuristic approach.

7.2.4 Numerical filtering

For the high-speed flows, we used a fourth-order Padé-filter (Gaitonde and Visbal, 2000) with $\alpha_f = 0.3$ to remove numerical oscillations. Future work should investigate alternative filtering strategies.

7.2.5 Free-shear flows

This thesis has focused only on boundary-layer flows. However, future work could use NOWNS to study nonlinear disturbance evolution in free-shear flows, such as jets and mixing layers.

7.2.6 Parallelization

The current NOWNS code is written in MATLAB is runs in serial. However, the LU decomposition for each linear OWNS system could be performed in parallel, so future work should parallelize the code in a different programming language, such as C++.

Bibliography

Araya, D., Bitter, N., Wheaton, B. M., Kamal, O., Colonius, T., Knutson, A., Johnson, H., Nichols, J., Candler, G. V., Russo, V., and Brehm, C. 2022. Assessment of linear methods for analysis of boundary layer instabilities on a finned cone at mach 6. In *AIAA AVIATION 2022 Forum*. doi: 10.2514/6.2022-3247.

Berlin, S., Wiegel, M., and Henningson, D. S. 1999. Numerical and experimental investigations of oblique boundary layer transition. *Journal of Fluid Mechanics*, 393:23–57. doi: 10.1017/S002211209900511X.

Bertolotti, F. P., Herbert, T., and Spalart, P. R. 1992. Linear and nonlinear stability of the Blasius boundary layer. *Journal of Fluid Mechanics*, 242:441–474. doi: 10.1017/S0022112092002453.

Bertolotti, F. P., 1991. *Linear and nonlinear stability of boundary layers with streamwise varying properties*. PhD thesis, The Ohio State University.

Blasius, P. R. H. 1908. Grenzschichten in Flüssigkeiten mit kleiner Reibung. *Zeitschrift für angewandte Mathematik und Physik*, 56:1–37.

Briggs, R. J., 1964. Electron-stream interaction with plasmas.

Broadhurst, M. S. and Sherwin, S. J. 2008. The parabolised stability equations for 3d-flows: implementation and numerical stability. *Applied Numerical Mathematics*, 58(7):1017–1029. ISSN 0168-9274. doi: https://doi.org/10.1016/j.apnum.2007.04.016. Spectral Methods in Computational Fluid Dynamics.

Chang, C.-L. and Malik, M. R. 1994. Oblique-mode breakdown and secondary instability in supersonic boundary layers. *Journal of Fluid Mechanics*, 273: 323–360. doi: 10.1017/S0022112094001965.

Chang, C.-L., Malik, M. R., Erlebacher, G., and Hussaini, M. Y., 1993. Linear and nonlinear PSE for compressible boundary layers. NASA Contractor Report 191537. Institute for Computer Applications in Science and Engineering (ICASE).

Cheung, L. C. and Lele, S. K., 2007. *Aeroacoustic Noise Prediction and the Dynamics of Shear Layers and Jets Using the Nonlinear Parabolized Stability Equations*. PhD thesis, Stanford.

Claerbout, J. F. *Fundamentals of geophysical data processing with applications to petroleum prospecting. [Textbook]*. McGraw-Hill Book Co., Inc.,New York, 1976.

Claerbout, J. F. *Imaging the earth's interior*. Blackwell Scientific Pub.,Palo Alto, CA, 1985.

Collins, M. D. 1989. Applications and time-domain solution of higher-order parabolic equations in underwater acoustics. *The Journal of the Acoustical Society of America*, 86(3):1097–1102. ISSN 0001-4966. doi: 10.1121/1.398101.

Day, M. J., Mansour, N. N., and Reynolds, W. C. 2001. Nonlinear stability and structure of compressible reacting mixing layers. *Journal of Fluid Mechanics*, 446:375–408. doi: 10.1017/S002211200100595X.

Day, M. J., 1999. *Structure and stability of compressible reacting mixing layers*. PhD thesis, Stanford University, California.

De Tullio, N., Paredes, P., Sandham, N. D., and Theofilis, V. 2013. Laminar–turbulent transition induced by a discrete roughness element in a supersonic boundary layer. *Journal of Fluid Mechanics*, 735:613–646. doi: 10.1017/jfm.2013.520.

Fasel, H. F., Rist, U., and Konzelmann, U. 1990. Numerical investigation of the three-dimensional development in boundary-layer transition. *AIAA Journal*, 28 (1):29–37. doi: 10.2514/3.10349.

Fedorov, A. 2011. Transition and stability of high-speed boundary layers. *Annual Review of Fluid Mechanics*, 43(Volume 43, 2011):79–95. ISSN 1545-4479. doi: https://doi.org/10.1146/annurev-fluid-122109-160750.

Franko, K. J. and Lele, S. K. 2013. Breakdown mechanisms and heat transfer overshoot in hypersonic zero pressure gradient boundary layers. *Journal of Fluid Mechanics*, 730:491–532. doi: 10.1017/jfm.2013.350.

Gaitonde, D. V. and Visbal, M. R. 2000. Padé-type higher-order boundary filters for the navier-stokes equations. *AIAA Journal*, 38(11):2103–2112. doi: 10.2514/2.872.

Givoli, D. and Neta, B. 2003. High-order non-reflecting boundary scheme for time-dependent waves. *Journal of Computational Physics*, 186(1):24–46. ISSN 0021-9991. doi: 10.1016/S0021-9991(03)00005-6.

Guddati, M. N. 2006. Arbitrarily wide-angle wave equations for complex media. *Computer Methods in Applied Mechanics and Engineering*, 195(1):65–93. ISSN 0045-7825. doi: 10.1016/j.cma.2005.01.006.

Hack, M. P. and Moin, P. 2017. Algebraic disturbance growth by interaction of orr and lift-up mechanisms. *Journal of Fluid Mechanics*, 829:112–126. doi: 10.1017/jfm.2017.557.

Hagstrom, T. and Warburton, T. 2004. A new auxiliary variable formulation of high-order local radiation boundary conditions: corner compatibility conditions and extensions to first-order systems. *Wave Motion*, 39(4):327–338. doi: 10.1016/j.wavemoti.2003.12.007. New computational methods for wave propagation.

Halpern, L. and Trefethen, L. N. 1988. Wide-angle one-way wave equations. *The Journal of the Acoustical Society of America*, 84(4):1397–1404. ISSN 0001-4966. doi: 10.1121/1.396586.

Herbert, T. 1988. Secondary instability of boundary layers. *Annual Review of Fluid Mechanics*, 20(1):487–526. doi: 10.1146/annurev.fl.20.010188.002415.

Herbert, T. 1997. Parabolized stability equations. *Annual Review of Fluid Mechanics*, 29(1):245–283. doi: 10.1146/annurev.fluid.29.1.245.

Higdon, R. L. 1986. Initial-boundary value problems for linear hyperbolic systems. *SIAM Review*, 28(2):177–217.

Huai, X., Joslin, R. D., and Piomelli, U. 1997. Large-eddy simulation of transition to turbulence in boundary layers. *Theoretical and Computational Fluid Dynamics*, 9:149–163.

Huerre, P. and Monkewitz, P. A. 1985. Absolute and convective instabilities in free shear layers. *Journal of Fluid Mechanics*, 159:151–168. doi: 10.1017/S0022112085003147.

Jensen, F. B., Kuperman, W. A., Porter, M. B., Schmidt, H., and Bartram, J. F. 1995. Computational ocean acoustics. *The Journal of the Acoustical Society of America*, 97(5):3213–3213. ISSN 0001-4966. doi: 10.1121/1.411832.

Joslin, R. D., Streett, C. L., and Chang, C. L. 1993. Spatial direct numerical simulation of boundary-layer transition mechanisms: Validation of PSE theory. *Theoretical and Computational Fluid Dynamics*, 4(6):271–288. doi: 10.1007/BF00418777.

Joslin, R., Streett, C., and Chang, C.-L., 1991. Validation of three-dimensional incompressible spatial direct numerical simulation code: a comparison with linear stability and parabolic stability equation theories for boundary-layer transition on a flat plate. NASA Technical Paper TP-3205.

Kachanov, Y. S. and Levchenko, V. Y. 1984. The resonant interaction of disturbances at laminar-turbulent transition in a boundary layer. *Journal of Fluid Mechanics*, 138:209–247. doi: 10.1017/S0022112084000100.

Kamal, O., 2023. *Optimal receptivity and the generalization of the One-Way Navier-Stokes (OWNS) Equations to complex high-speed boundary layers and jets*. PhD thesis, California Institute of Technology.

Kamal, O., Rigas, G., Lakebrink, M. T., and Colonius, T. 2020. Application of the One-Way Navier-Stokes (OWNS) Equations to hypersonic boundary layers. In *AIAA AVIATION 2020 FORUM*. doi: 10.2514/6.2020-2986.

Kamal, O., Rigas, G., Lakebrink, M., and Colonius, T. 2021. Input/output analysis of hypersonic boundary layers using the One-Way Navier-Stokes (OWNS) Equations. In *AIAA AVIATION 2021 FORUM*. doi: 10.2514/6.2021-2827.

Kamal, O., Rigas, G., Lakebrink, M. T., and Colonius, T. 2022. Input/output analysis of a Mach-6 cooled-wall hypersonic boundary layer using the One-Way Navier-Stokes (OWNS) Equations. In *AIAA AVIATION 2022 Forum*. doi: 10.2514/6.2022-3556.

Klebanoff, P. S., Tidstrom, K. D., and Sargent, L. M. 1962. The three-dimensional nature of boundary-layer instability. *Journal of Fluid Mechanics*, 12(1):1–34. doi: 10.1017/S0022112062000014.

Kreiss, H.-O. 1970. Initial boundary value problems for hyperbolic systems. *Communications on Pure and Applied Mathematics*, 23(3):277–298. doi: https://doi.org/10.1002/cpa.3160230304.

Lakebrink, M. T., Paredes, P., and Borg, M. P. 2017. Toward robust prediction of crossflow-wave instability in hypersonic boundary layers. *Computers & Fluids*, 144:1–9. ISSN 0045-7930. doi: https://doi.org/10.1016/j.compfluid.2016.11.016.

Lee, D., Pierce, A. D., and Shang, E.-C. 2000. Parabolic equation development in the twentieth century. *Journal of Computational Acoustics*, 08(04):527–637. doi: 10.1142/S0218396X00000388.

Leinemann, M., Hader, C., and Fasel, H. F. 2021. Direct numerical simulations of the nonlinear boundary layer transition regime on a flat plate at Mach 6. In *AIAA Scitech 2021 Forum*. doi: 10.2514/6.2021-1739.

Li, F. and Malik, M. R. 1996. On the nature of PSE approximation. *Theoretical and Computational Fluid Dynamics*, 8(4):253–273. doi: 10.1007/BF00639695.

Li, F. and Malik, M. R. 1997. Spectral analysis of parabolized stability equations. *Computers & Fluids*, 26(3):279–297. ISSN 0045-7930. doi: https://doi.org/10.1016/S0045-7930(96)00044-8. URL `https://www.sciencedirect.com/science/article/pii/S0045793096000448`.

Ma, Y. and Zhong, X. 2003. Receptivity of a supersonic boundary layer over a flat plate. Part 1. Wave structures and interactions. *Journal of Fluid Mechanics*, 488:31–78. doi: 10.1017/S0022112003004786.

Mack, L. M., 1984. Boundary-layer linear stability theory. Advisory Group for Aerospace Research and Development (AGARD) Report No. 709, Part 3. *Special Course on Stability and Transition of Laminar Flow*.

Monokrousos, A., Åkervik, E., Brandt, L., and Henningson, D. S. 2010. Global three-dimensional optimal disturbances in the Blasius boundary-layer flow using time-steppers. *Journal of Fluid Mechanics*, 650:181–214. doi: 10.1017/S0022112009993703.

Morkovin, M. V. 1969. On the many faces of transition. In Wells, C. S., editor, *Viscous Drag Reduction*, pages 1–31, Boston, MA. Springer US. ISBN 978-1-4899-5579-1.

Morkovin, M. V., Eli, R., and Herbert, T. 1994. Transition in open flow systems: a reassessment. *Bull. APS*, 39.

Orr, W. M. 1907. The Stability or Instability of the Steady Motions of a Perfect Liquid and of a Viscous Liquid. Part II: A Viscous Liquid. *Proceedings of the Royal Irish Academy. Section A: Mathematical and Physical Sciences*, 27:69–138. ISSN 00358975. URL http://www.jstor.org/stable/20490591.

Paredes, P., Hanifi, A., Theofilis, V., and Henningson, D. S. 2015. The Nonlinear PSE-3D Concept for Transition Prediction in Flows with a Single Slowly-varying Spatial Direction. *Procedia IUTAM*, 14:36–44. ISSN 2210-9838. doi: https://doi.org/10.1016/j.piutam.2015.03.021. URL https://www.sciencedirect.com/science/article/pii/S2210983815000474.

Paredes, P., Choudhari, M. M., and Li, F. 2016a. Transition due to streamwise streaks in a supersonic flat plate boundary layer. *Phys. Rev. Fluids*, 1:083601. doi: 10.1103/PhysRevFluids.1.083601.

Paredes, P., Choudhari, M. M., Li, F., and Chang, C.-L. 2016b. Optimal growth in hypersonic boundary layers. *AIAA Journal*, 54(10):3050–3061. doi: 10.2514/1.J054912.

Prandtl, L. 1904. Über Flüssigkeitsbewegung bei sehr kleiner Reibung. In *Verhandlinger 3. Int. Math. Kongr. Heidelberg*, page 484–491.

Pruett, C. D., Zang, T. A., Chang, C.-L., and Carpenter, M. H. 1995. Spatial direct numerical simulation of high-speed boundary-layer flows part I: Algorithmic considerations and validation. *Theor. Comput. Fluid Dyn.*, 7(1):49–76.

Rigas, G., Colonius, T., and Beyar, M. 2017a. Stability of wall-bounded fows using one-way spatial integration of Navier-Stokes equations. In *55th AIAA Aerospace Sciences Meeting*. doi: 10.2514/6.2017-1881.

Rigas, G., Schmidt, O. T., Colonius, T., and Brès, G. A. 2017b. One way navier-stokes and resolvent analysis for modeling coherent structures in a supersonic turbulent jet. In *23rd AIAA/CEAS Aeroacoustics Conference*. doi: 10.2514/6.2017-4046.

Rigas, G., Sipp, D., and Colonius, T. 2021. Nonlinear input/output analysis: application to boundary layer transition. *Journal of Fluid Mechanics*, 911:A15. doi: 10.1017/jfm.2020.982.

Rist, U. and Fasel, H. 1995. Direct numerical simulation of controlled transition in a flat-plate boundary layer. *Journal of Fluid Mechanics*, 298:211–248. doi: 10.1017/S0022112095003284.

Rodríguez, D., Jotkar, M. R., and Gennaro, E. M. 2018. Wavepacket models for subsonic twin jets using 3D parabolized stability equations. *Comptes Rendus Mécanique*, 346(10):890–902. ISSN 1631-0721. doi: https://doi.org/10.1016/j.crme.2018.07.002. URL https://www.sciencedirect.com/science/article/pii/S163107211830144X. Jet noise modelling and control / Modélisation et contrôle du bruit de jet.

Rudel, C., Pernet, S., and Brazier, J.-P. 2022. Numerical Factorization of Propagation Operator for Hyperbolic Equations and Application to One-way, True Amplitude One-way Equations and Bremmer Series. *Journal of Scientific Computing*, 93. doi: 10.1007/s10915-022-01985-7.

Sayadi, T., Hamman, C. W., and Moin, P. 2013. Direct numerical simulation of complete H-type and K-type transitions with implications for the dynamics of turbulent boundary layers. *Journal of Fluid Mechanics*, 724:480–509. doi: 10.1017/jfm.2013.142.

Schlichting, H. 1933. Zur enstehung der turbulenz bei der plattenströmung. *Nachrichten von der Gesellschaft der Wissenschaften zu Göttingen, Mathematisch-Physikalische Klasse*, pages 181–208.

Schlichting, H. and Gersten, K. *Boundary-Layer Theory*. Springer Berlin Heidelberg, 2017. ISBN 9783662529195. doi: 10.1007/978-3-662-52919-5. URL http://dx.doi.org/10.1007/978-3-662-52919-5.

Schmid, P. and Henningson, D. *Stability and Transition in Shear Flows*, volume 142, chapter 7.2.1. Springer New York, NY, 2001. doi: 10.1007/978-1-4613-0185-1.

Schneider, S. P. 2001. Effects of high-speed tunnel noise on laminar-turbulent transition. *Journal of Spacecraft and Rockets*, 38(3):323–333. doi: 10.2514/2.3705.

Scholten, A., Paredes, P., Choudhari, M. M., Li, F., Carpenter, M., and Bailey, M. 2024. Nonlinear nonmodal analysis of hypersonic flow over blunt cones. *AIAA Journal*, 62(9):3271–3283. doi: 10.2514/1.J063602.

Schubauer, G. B. and Skramstad, H. K. 1947. Laminar-boundary-layer oscillations and transition on a flat plate. *Journal of research of the National Bureau of Standards*, 38:251.

Sleeman, M. K. and Colonius, T. 2025. Greedy recursion parameter selection for the One-Way Navier-Stokes (OWNS) equations. *arXiv*. doi: 10.48550/arXiv.2506.02320.

Sleeman, M. K., Lakebrink, M. T., and Colonius, T. 2023. Nonlinear stability of wall-bounded flows using the One-Way Navier-Stokes (OWNS) Equations. In *AIAA AVIATION 2023 Forum*. doi: 10.2514/6.2023-3273.

Sleeman, M. K., Lakebrink, M. T., and Colonius, T. 2024a. Simulation of K-type and H-type Transition Using the Nonlinear One-Way Navier-Stokes Approach. In *Tenth IUTAM Symposium on Laminar-Turbulent Transition*.

Sleeman, M. K., Lakebrink, M. T., and Colonius, T. 2024b. The Nonlinear One-Way Navier-Stokes (NOWNS) Approach for Boundary-Layer Transition. In *AIAA AVIATION FORUM AND ASCEND 2024*. doi: 10.2514/6.2024-3530.

Sleeman, M. K., Colonius, T., and Lakebrink, M. T. 2025. Boundary-Layer Stability Analysis Using the Nonlinear One-Way Navier–Stokes Approach. *AIAA J.*, 63 (8):3145–3159. doi: 10.2514/1.J064909.

Smith, A., Company, D. A., Gamberoni, N., Sub-Committee, A. R. C. F. M., and Department, D. A. C. E. S. D. E. *Transition, Pressure Gradient and Stability Theory*. ARC-19322. Douglas Aircraft Company, El Segundo Division, 1956.

Sommerfeld, A. 1908. Bin Beitrag zur Hydrodynamischen Erklaerung der Turbulenten Fluessigkeitsbewegungen. In *4th International Congress of Mathematics*.

Tempelmann, D., Hanifi, A., and Henningson, D. S. 2010. Spatial optimal growth in three-dimensional boundary layers. *Journal of Fluid Mechanics*, 646:5–37. doi: 10.1017/S0022112009993260.

Tempelmann, D., Hanifi, A., and Henningson, D. S. 2012. Spatial optimal growth in three-dimensional compressible boundary layers. *Journal of Fluid Mechanics*, 704:251–279. doi: 10.1017/jfm.2012.235.

Thompson, K. W. 1987. Time dependent boundary conditions for hyperbolic systems. *Journal of Computational Physics*, 68(1):1–24. ISSN 0021-9991. doi: https://doi.org/10.1016/0021-9991(87)90041-6. URL `https://www.sciencedirect.com/science/article/pii/0021999187900416`.

Tollmien, W. 1929. Über die Entstehung der Turbulenz. 1. Mitteilung. *Nachrichten von der Gesellschaft der Wissenschaften zu Göttingen, Mathematisch-Physikalische Klasse*, pages 21–44.

Towne, A., 2016. *Advancements in Jet Turbulence and Noise Modeling: Accurate One-Way Solutions and Empirical Evaluation of the Nonlinear Forcing of Wavepackets*. PhD thesis, California Institute of Technology.

Towne, A. and Colonius, T. 2015. One-way spatial integration of hyperbolic equations. *Journal of Computational Physics*, 300:844–861. ISSN 0021-9991. doi: https://doi.org/10.1016/j.jcp.2015.08.015.

Towne, A., Rigas, G., and Colonius, T. 2019. A critical assessment of the parabolized stability equations. *Theoretical and Computational Fluid Dynamics*, 33. doi: 10.1007/s00162-019-00498-8.

Towne, A., Rigas, G., Kamal, O., Pickering, E., and Colonius, T. 2022. Efficient global resolvent analysis via the one-way Navier–Stokes equations. *Journal of Fluid Mechanics*, 948:A9. doi: 10.1017/jfm.2022.647.

Trefethen, L. N. and Halpern, L. 1986. Well-posedness of one-way wave equations and absorbing boundary conditions. *Mathematics of Computation*, 47(176):421–435.

Van Ingen, J., Sub-Committee, A. R. C. F. M., and Technische Hogeschool Delft, V. *A Suggested Semi-empirical Method for the Calculation of the Boundary Layer Transition Region*. ARC-19337. TH Delft, Delft, 1956.

White, F. *Viscous Fluid Flow*. McGraw-Hill Internation Edition, 2006.

Zhu, M. and Towne, A. 2023. Recursive one-way Navier-Stokes equations with PSE-like cost. *Journal of Computational Physics*, 473:111744. ISSN 0021-9991. doi: https://doi.org/10.1016/j.jcp.2022.111744. URL https://www.sciencedirect.com/science/article/pii/S0021999122008075.

Appendix A

NAVIER-STOKES EQUATIONS

Given the non-dimensional Navier-Stokes equations (1.1), we define the vector $\boldsymbol{q} = (v, u, v, w, p)$ and write

$$\begin{aligned}
&\frac{\partial \boldsymbol{q}}{\partial t} + [A_x(\boldsymbol{q}) + B_x(\boldsymbol{q})]\frac{\partial \boldsymbol{q}}{\partial x} + [A_y(\boldsymbol{q}) + B_y(\boldsymbol{q})]\frac{\partial \boldsymbol{q}}{\partial y} \\
&\quad + [A_z(\boldsymbol{q}) + B_z(\boldsymbol{q})]\frac{\partial \boldsymbol{q}}{\partial z} + B_{xx}(\boldsymbol{q})\frac{\partial^2 \boldsymbol{q}}{\partial x^2} + B_{yy}(\boldsymbol{q})\frac{\partial^2 \boldsymbol{q}}{\partial y^2} + B_{zz}(\boldsymbol{q})\frac{\partial^2 \boldsymbol{q}}{\partial z^2} \\
&\quad + B_{xy}(\boldsymbol{q})\frac{\partial^2 \boldsymbol{q}}{\partial x \partial y} + B_{xz}(\boldsymbol{q})\frac{\partial^2 \boldsymbol{q}}{\partial x \partial z} + B_{yz}(\boldsymbol{q})\frac{\partial^2 \boldsymbol{q}}{\partial y \partial z} = 0,
\end{aligned} \tag{A.1}$$

where B denotes viscous terms while A denotes inviscid terms. Next we decompose the flow into a time-invariant equilibrium solution, $\bar{\boldsymbol{q}}$, and a time-varying disturbance variable, $\boldsymbol{q}'$, such that $\boldsymbol{q} = \bar{\boldsymbol{q}} + \boldsymbol{q}'$, which we use to obtain

$$\begin{aligned}
&\frac{\partial \boldsymbol{q}'}{\partial t} + [A_x(\bar{\boldsymbol{q}}) + B_x(\bar{\boldsymbol{q}})]\frac{\partial \boldsymbol{q}'}{\partial x} + [A_y(\bar{\boldsymbol{q}}) + B_y(\bar{\boldsymbol{q}})]\frac{\partial \boldsymbol{q}'}{\partial y} + [A_z(\bar{\boldsymbol{q}}) + B_z(\bar{\boldsymbol{q}})]\frac{\partial \boldsymbol{q}'}{\partial z} \\
&\quad + C(\bar{\boldsymbol{q}})\boldsymbol{q}' + B_{xx}(\bar{\boldsymbol{q}})\frac{\partial^2 \boldsymbol{q}'}{\partial x^2} + B_{yy}(\bar{\boldsymbol{q}})\frac{\partial^2 \boldsymbol{q}'}{\partial y^2} + B_{zz}(\bar{\boldsymbol{q}})\frac{\partial^2 \boldsymbol{q}'}{\partial z^2} \\
&\quad + B_{xy}(\bar{\boldsymbol{q}})\frac{\partial^2 \boldsymbol{q}'}{\partial x \partial y} + B_{xz}(\bar{\boldsymbol{q}})\frac{\partial^2 \boldsymbol{q}'}{\partial x \partial z} + B_{yz}(\bar{\boldsymbol{q}})\frac{\partial^2 \boldsymbol{q}'}{\partial y \partial z} = \boldsymbol{F}(\boldsymbol{q}'),
\end{aligned} \tag{A.2}$$

where we have defined $C(\bar{\boldsymbol{q}})$ such that

$$\begin{aligned}
C(\bar{\boldsymbol{q}})\boldsymbol{q}' &= [A_x(\boldsymbol{q}') + B_x(\boldsymbol{q}')]\frac{\partial \bar{\boldsymbol{q}}}{\partial x} + [A_y(\boldsymbol{q}') + B_y(\boldsymbol{q}')]\frac{\partial \bar{\boldsymbol{q}}}{\partial y} \\
&\quad + [A_z(\boldsymbol{q}') + B_z(\boldsymbol{q}')]\frac{\partial \bar{\boldsymbol{q}}}{\partial z} + B_{xx}(\boldsymbol{q}')\frac{\partial^2 \bar{\boldsymbol{q}}}{\partial x^2} + B_{yy}(\boldsymbol{q}')\frac{\partial^2 \bar{\boldsymbol{q}}}{\partial y^2} \\
&\quad + B_{zz}(\boldsymbol{q}')\frac{\partial^2 \bar{\boldsymbol{q}}}{\partial z^2} + B_{xy}(\boldsymbol{q}')\frac{\partial^2 \bar{\boldsymbol{q}}}{\partial x \partial y} + B_{xz}(\boldsymbol{q}')\frac{\partial^2 \bar{\boldsymbol{q}}}{\partial x \partial z} + B_{yz}(\boldsymbol{q}')\frac{\partial^2 \bar{\boldsymbol{q}}}{\partial y \partial z},
\end{aligned} \tag{A.3}$$

and the nonlinear term

$$\begin{aligned}
\boldsymbol{F}(\boldsymbol{q}') &= -[A_x(\boldsymbol{q}') + B_x(\boldsymbol{q}')]\frac{\partial \boldsymbol{q}'}{\partial x} - [A_y(\boldsymbol{q}') + B_y(\boldsymbol{q}')]\frac{\partial \boldsymbol{q}'}{\partial y} \\
&\quad - [A_z(\boldsymbol{q}') + B_z(\boldsymbol{q}')]\frac{\partial \boldsymbol{q}'}{\partial z} - B_{xx}(\boldsymbol{q}')\frac{\partial^2 \boldsymbol{q}'}{\partial x^2} - B_{yy}(\boldsymbol{q}')\frac{\partial^2 \boldsymbol{q}'}{\partial y^2} \\
&\quad - B_{yy}(\boldsymbol{q}')\frac{\partial^2 \boldsymbol{q}'}{\partial z^2} - B_{xy}(\boldsymbol{q}')\frac{\partial^2 \boldsymbol{q}'}{\partial x \partial y} - B_{xz}(\boldsymbol{q}')\frac{\partial^2 \boldsymbol{q}'}{\partial x \partial z} - B_{yz}(\boldsymbol{q}')\frac{\partial^2 \boldsymbol{q}'}{\partial y \partial z}.
\end{aligned} \tag{A.4}$$

We further define the linear operator

$$\begin{aligned}\mathcal{L}(\bar{\boldsymbol{q}}) = &-\frac{\partial}{\partial t} - [A_y(\bar{\boldsymbol{q}}) + B_y(\bar{\boldsymbol{q}})]\frac{\partial \boldsymbol{q}'}{\partial y} - [A_z(\bar{\boldsymbol{q}}) + B_z(\bar{\boldsymbol{q}})]\frac{\partial \boldsymbol{q}'}{\partial z} - C(\bar{\boldsymbol{q}})\boldsymbol{q}' \\ &- B_{yy}(\bar{\boldsymbol{q}})\frac{\partial^2 \boldsymbol{q}'}{\partial y^2} - B_{zz}(\bar{\boldsymbol{q}})\frac{\partial^2 \boldsymbol{q}'}{\partial z^2} - B_{yz}(\bar{\boldsymbol{q}})\frac{\partial^2 \boldsymbol{q}'}{\partial y \partial z} = 0,\end{aligned} \tag{A.5}$$

yielding

$$\begin{aligned}A_x(\bar{\boldsymbol{q}})\frac{\partial \boldsymbol{q}'}{\partial x} = &\mathcal{L}(\bar{\boldsymbol{q}})\boldsymbol{q}' + \boldsymbol{F}(\boldsymbol{q}') - B_x(\bar{\boldsymbol{q}})\frac{\partial \boldsymbol{q}'}{\partial x} \\ &- B_{xx}(\bar{\boldsymbol{q}})\frac{\partial^2 \boldsymbol{q}'}{\partial x^2} - B_{xy}(\bar{\boldsymbol{q}})\frac{\partial^2 \boldsymbol{q}'}{\partial x \partial y} - B_{xz}(\bar{\boldsymbol{q}})\frac{\partial^2 \boldsymbol{q}'}{\partial x \partial z}.\end{aligned} \tag{A.6}$$

The operators for the first derivatives (without viscous terms), A_x, A_y, and A_z, as well as the operators for the first derivatives (with viscous terms) B_x, B_y, and B_z, are given by

$$A_x(\boldsymbol{q}) = \begin{bmatrix} u & -\nu & 0 & 0 & 0 \\ 0 & u & 0 & 0 & \nu \\ 0 & 0 & u & 0 & 0 \\ 0 & 0 & 0 & u & 0 \\ 0 & \gamma p & 0 & 0 & u \end{bmatrix}, \qquad B_x(\boldsymbol{q}) = -\frac{2\gamma}{PrRe}\begin{bmatrix} 0 & 0 & 0 & 0 & 0 \\ 0 & 0 & 0 & 0 & 0 \\ 0 & 0 & 0 & 0 & 0 \\ 0 & 0 & 0 & 0 & 0 \\ \frac{\partial p}{\partial x} & 0 & 0 & 0 & \frac{\partial \nu}{\partial x} \end{bmatrix},$$

$$A_y(\boldsymbol{q}) = \begin{bmatrix} v & 0 & -\nu & 0 & 0 \\ 0 & v & 0 & 0 & 0 \\ 0 & 0 & v & 0 & \nu \\ 0 & 0 & 0 & v & 0 \\ 0 & 0 & \gamma p & 0 & v \end{bmatrix}, \qquad B_y(\boldsymbol{q}) = -\frac{2\gamma}{PrRe}\begin{bmatrix} 0 & 0 & 0 & 0 & 0 \\ 0 & 0 & 0 & 0 & 0 \\ 0 & 0 & 0 & 0 & 0 \\ 0 & 0 & 0 & 0 & 0 \\ \frac{\partial p}{\partial y} & 0 & 0 & 0 & \frac{\partial \nu}{\partial y} \end{bmatrix},$$

$$A_z(\boldsymbol{q}) = \begin{bmatrix} w & 0 & 0 & -\nu & 0 \\ 0 & w & 0 & 0 & 0 \\ 0 & 0 & w & 0 & 0 \\ 0 & 0 & 0 & w & \nu \\ 0 & 0 & 0 & \gamma p & w \end{bmatrix}, \qquad B_z(\boldsymbol{q}) = -\frac{2\gamma}{PrRe}\begin{bmatrix} 0 & 0 & 0 & 0 & 0 \\ 0 & 0 & 0 & 0 & 0 \\ 0 & 0 & 0 & 0 & 0 \\ 0 & 0 & 0 & 0 & 0 \\ \frac{\partial p}{\partial z} & 0 & 0 & 0 & \frac{\partial \nu}{\partial z} \end{bmatrix}.$$

For the second derivatives B_{xx}, B_{yy}, B_{zz}, B_{xy}, B_{xz}, and B_{yz} we have

$$B_{xx}(\boldsymbol{q}) = \begin{bmatrix} 0 & 0 & 0 & 0 & 0 \\ 0 & -\frac{4}{3}\frac{\nu}{Re} & 0 & 0 & 0 \\ 0 & 0 & -\frac{\nu}{Re} & 0 & 0 \\ 0 & 0 & 0 & -\frac{\nu}{Re} & 0 \\ -\frac{\gamma p}{RePr} & 0 & 0 & 0 & -\frac{\gamma\nu}{RePr} \end{bmatrix}, \qquad B_{xy}(\boldsymbol{q}) = \begin{bmatrix} 0 & 0 & 0 & 0 & 0 \\ 0 & 0 & -\frac{\nu}{3Re} & 0 & 0 \\ 0 & -\frac{\nu}{3Re} & 0 & 0 & 0 \\ 0 & 0 & 0 & 0 & 0 \\ 0 & 0 & 0 & 0 & 0 \end{bmatrix},$$

$$B_{yy}(\boldsymbol{q}) = \begin{bmatrix} 0 & 0 & 0 & 0 & 0 \\ 0 & -\frac{\nu}{Re} & 0 & 0 & 0 \\ 0 & 0 & -\frac{4}{3}\frac{\nu}{Re} & 0 & 0 \\ 0 & 0 & 0 & -\frac{\nu}{Re} & 0 \\ -\frac{\gamma p}{RePr} & 0 & 0 & 0 & -\frac{\gamma\nu}{RePr} \end{bmatrix}, \qquad B_{xz}(\boldsymbol{q}) = \begin{bmatrix} 0 & 0 & 0 & 0 & 0 \\ 0 & 0 & 0 & -\frac{\nu}{3Re} & 0 \\ 0 & 0 & 0 & 0 & 0 \\ 0 & -\frac{\nu}{3Re} & 0 & 0 & 0 \\ 0 & 0 & 0 & 0 & 0 \end{bmatrix},$$

$$B_{zz}(\boldsymbol{q}) = \begin{bmatrix} 0 & 0 & 0 & 0 & 0 \\ 0 & -\frac{\nu}{Re} & 0 & 0 & 0 \\ 0 & 0 & -\frac{\nu}{Re} & 0 & 0 \\ 0 & 0 & 0 & -\frac{4}{3}\frac{\nu}{Re} & 0 \\ -\frac{\gamma p}{RePr} & 0 & 0 & 0 & -\frac{\gamma\nu}{RePr} \end{bmatrix}, \qquad B_{yz}(\boldsymbol{q}) = \begin{bmatrix} 0 & 0 & 0 & 0 & 0 \\ 0 & 0 & 0 & 0 & 0 \\ 0 & 0 & 0 & -\frac{\nu}{3Re} & 0 \\ 0 & 0 & -\frac{\nu}{3Re} & 0 & 0 \\ 0 & 0 & 0 & 0 & 0 \end{bmatrix}.$$

Finally, the operator C is given by

$$C(\boldsymbol{q}) = \begin{bmatrix} -\nabla\cdot\boldsymbol{u} & \frac{\partial\nu}{\partial x} & \frac{\partial\nu}{\partial y} & \frac{\partial\nu}{\partial z} & 0 \\ \frac{\partial p}{\partial x} - \frac{1}{Re}\nabla^2 u - \frac{1}{3Re}[\partial_{xx}u + \partial_{xy}v + \partial_{xz}w] & \frac{\partial u}{\partial x} & \frac{\partial u}{\partial y} & \frac{\partial u}{\partial z} & 0 \\ \frac{\partial p}{\partial y} - \frac{1}{Re}\nabla^2 v - \frac{1}{3Re}[\partial_{xy}u + \partial_{yy}v + \partial_{yz}w] & \frac{\partial v}{\partial x} & \frac{\partial v}{\partial y} & \frac{\partial v}{\partial z} & 0 \\ \frac{\partial p}{\partial z} - \frac{1}{Re}\nabla^2 w - \frac{1}{3Re}[\partial_{xz}u + \partial_{yz}v + \partial_{zz}w] & \frac{\partial w}{\partial x} & \frac{\partial w}{\partial y} & \frac{\partial w}{\partial z} & 0 \\ -\frac{\gamma}{RePr}\nabla^2 p & \frac{\partial p}{\partial x} & \frac{\partial p}{\partial y} & \frac{\partial p}{\partial z} & \gamma\nabla\cdot\boldsymbol{u} - \frac{\gamma}{RePr}\nabla^2\nu \end{bmatrix},$$

while the nonlinear term is a vector comprising the following components:

$$F_1(\boldsymbol{q}) = u\frac{\partial\nu}{\partial x} + \nu\frac{\partial\nu}{\partial y} + w\frac{\partial\nu}{\partial z} - \nu\frac{\partial u}{\partial x} - \nu\frac{\partial v}{\partial y} - \nu\frac{\partial w}{\partial z},$$

$$F_2(\boldsymbol{q}) = \nu\frac{\partial p}{\partial x} - u\frac{\partial u}{\partial x} - v\frac{\partial u}{\partial y} - w\frac{\partial u}{\partial z} + \frac{1}{Re}\nu\nabla^2 u + \frac{1}{3Re}\Big(\frac{\partial^2 u}{\partial x^2} + \frac{\partial^2 v}{\partial x\partial y} + \frac{\partial^2 w}{\partial x\partial z}\Big),$$

$$F_3(\boldsymbol{q}) = \nu\frac{\partial p}{\partial y} - u\frac{\partial v}{\partial x} - v\frac{\partial v}{\partial y} - w\frac{\partial v}{\partial z} + \frac{1}{Re}\nu\nabla^2 u + \frac{1}{3Re}\Big(\frac{\partial^2 u}{\partial x\partial y} + \frac{\partial^2 v}{\partial y^2} + \frac{\partial^2 w}{\partial y\partial z}\Big),$$

$$F_4(\boldsymbol{q}) = \nu\frac{\partial p}{\partial z} - u\frac{\partial w}{\partial x} - v\frac{\partial w}{\partial y} - w\frac{\partial w}{\partial z} + \frac{1}{Re}\nu\nabla^2 u + \frac{1}{3Re}\Big(\frac{\partial^2 u}{\partial x\partial z} + \frac{\partial^2 v}{\partial y\partial z} + \frac{\partial^2 w}{\partial z^2}\Big),$$

$$F_5(\boldsymbol{q}) = \frac{\gamma}{RePr}[\nu\nabla^2 p + 2\nabla p\cdot\nabla\nu + p\nabla^2\nu] - \boldsymbol{u}\cdot\nabla p - \gamma p\nabla\cdot\boldsymbol{u}.$$

Appendix B

SIMILARITY SOLUTIONS

B.1 Blasius equation

A time-invariant equilibrium solution (base flow) can be obtained for flat-plate boundary-layer flows by solving the Blasius equation (Blasius, 1908). We assume a 2D steady flow where $\partial p/\partial x = 0$, and the streamwise length scale is much larger than the wall-normal length scale, yielding the equations

$$\frac{\partial(\rho^* u^*)}{\partial x^*} + \frac{\partial(\rho^* v^*)}{\partial x^*} = 0, \tag{B.1a}$$

$$\rho^*\left(u^*\frac{\partial u^*}{\partial x^*} + v^*\frac{\partial u^*}{\partial y^*}\right) = \frac{\partial}{\partial y^*}\left(\mu^*\frac{\partial u^*}{\partial y^*}\right), \tag{B.1b}$$

$$\rho^*\left(u^*\frac{\partial h^*}{\partial x^*} + v^*\frac{\partial h^*}{\partial y^*} = \frac{\partial}{\partial y^*}\left(\frac{\mu^*}{Pr}\frac{\partial h^*}{\partial y^*}\right) + \mu^*\left(\frac{\partial \mu^*}{\partial y^*}\right)^2, \right. \tag{B.1c}$$

where $\rho^* = 1/v^*$ is the density and h^* is the enthalpy. In addition, the y-momentum equation yields $\partial p/\partial y$ so that the pressure is uniform throughout the flow. We introduce self-similar variables using the Howarth–Dorodnitsyn transformation (Schlichting and Gersten, 2017)

$$\eta = \sqrt{\frac{\rho^*_\infty U^*_\infty}{2\mu^*_\infty x^*}}\int_0^{y^*}\frac{\rho^*}{\rho^*_\infty}d\tilde{y}, \quad \psi = \sqrt{2\mu^*_\infty\rho^*_\infty U^*_\infty x^*}f(\eta), \tag{B.2}$$

where ψ is a stream function such that

$$\rho^* u^* = \frac{\partial\psi}{\partial y^*}, \quad \rho^* v^* = -\frac{\partial\psi}{\partial x^*},$$

so that conservation of mass is satisfied by construction. Next

$$\frac{\partial\eta}{\partial x^*} = -\frac{\eta}{2x^*}, \quad \frac{\partial\eta}{\partial y^*} = \frac{\rho^*}{\rho^*_\infty}\sqrt{\frac{\rho^*_\infty U^*_\infty}{2\mu^*_\infty x^*}},$$

while

$$u^* = \frac{1}{\rho^*}\frac{\partial\psi}{\partial y^*} = \frac{1}{\rho^*}\sqrt{2\mu^*_\infty\rho^*_\infty U^*_\infty x^*}f'\frac{\partial\eta}{\partial y^*}. = U^*_\infty f',$$

so that

$$\frac{\partial u^*}{\partial x^*} = U^*_\infty f''\frac{\partial\eta}{\partial x^*}, \quad \frac{\partial u^*}{\partial y^*} = U^*_\infty f''\frac{\partial\eta}{\partial y^*},$$

and conservation of x-momentum becomes

$$\frac{\partial}{\partial\eta}\Big(\frac{\rho^*\mu^*}{\rho^*_\infty\mu^*_\infty}f''\Big) + ff'' = 0.$$

We assume that the temperature is a function of η only so that $T^* = T^*(\eta)$, while for an ideal gas $dh^* = c^*_p dT^*$ and $a^*_\infty = \gamma R^* T^*_\infty$ so that the conservation of energy equation becomes

$$\frac{\partial}{\partial\eta}\Big(\frac{1}{Pr}\frac{\mu^*\rho^*}{\mu^*_\infty\rho^*_\infty}(T^*)'\Big) + (\gamma-1)\mathrm{Ma}^2_\infty\frac{\mu^*\rho^*T^*_\infty}{\mu^*_\infty\rho^*_\infty}(f'')^2 + f(T^*)' = 0.$$

Assuming that $\mu^* \propto T^*$ we obtain in non-dimensional form

$$f''' + ff'' = 0, \tag{B.3a}$$

$$\frac{1}{Pr}T'' + fT' + (\gamma-1)\mathrm{Ma}^2_\infty(f'')^2 = 0. \tag{B.3b}$$

We must enforce the no-slip and no-penetration boundary conditions so that $f(0) = f'(0) = 0$, while in the far-field we must have $\lim_{\eta\to\infty} u(\eta) = U_\infty$ so that $\lim_{\eta\to\infty} f'(\eta) = 1$. At the wall we satisfy either isothermal, $T'(0) = 0$, or adiabatic, $T(0) = 0$, boundary conditions, while in the free-stream we must have $\lim_{\eta\to\infty} T(\eta) = 1$. We solve this ODE for (f, f', f'', T, T') using a shooting method, which we then use to compute the base flow as a function of x and y. Then the base flow (v, u, v, p) can be obtained using

$$v(\eta) = T(\eta), \quad u(\eta) = \frac{\partial f}{\partial\eta}, \quad v(\eta) = T\sqrt{\frac{1}{2xRe}}[\eta f' - f], \quad p = \frac{1}{\gamma}, \tag{B.4}$$

where the expression for p comes from the ideal gas law and by using that p is constant, while for a given x, we solve for y in terms of η as

$$y(\eta) = \sqrt{2x}Re\int_0^\eta T d\tilde{\eta}. \tag{B.5}$$

Appendix C

SPECIAL CASES OF SINGULAR A

If A is singular, then we obtain

$$\tilde{A} = \begin{bmatrix} A_{++} & 0 & 0 \\ 0 & A_{--} & 0 \\ 0 & 0 & A_{00} \end{bmatrix} \tag{C.1}$$

for diagonal $A_{++} \in \mathbb{R}^{N_+ \times N_+}$ with $A_{++} > 0$, $A_{--} \in \mathbb{R}^{N_- \times N_-}$ with $A_{--} < 0$, and $A_{00} \in \mathbb{R}^{N_0 \times N_0}$ with $A_{00} = 0$, where $N_+ + N_- + N_0 = N$. Then we define

$$\tilde{A}_{\pm\pm} = \begin{bmatrix} A_{++} & 0 \\ 0 & A_{--} \end{bmatrix} \tag{C.2a}$$

and

$$\begin{aligned} \tilde{L}(s) &= \begin{bmatrix} L_{\pm\pm} & L_{\pm 0} \\ L_{0\pm} & L_{00} \end{bmatrix} \\ &= \begin{bmatrix} sI_{\pm\pm} + \sum_{j=2}^{d} i\omega_j \tilde{B}_{j,\pm\pm} + \tilde{C}_{\pm\pm} & \sum_{j=2}^{d} i\omega_j \tilde{B}_{j,\pm 0} + \tilde{C}_{\pm 0} \\ \sum_{j=2}^{d} i\omega_j \tilde{B}_{j,0\pm} + \tilde{C}_{0\pm} & sI_{00} + \sum_{j=2}^{d} i\omega_j \tilde{B}_{j,00} + \tilde{C}_{00} \end{bmatrix}, \end{aligned} \tag{C.2b}$$

so that

$$\tilde{A}_{\pm\pm} \frac{d\hat{\boldsymbol{\phi}}_\pm}{dx} = L_{\pm\pm}\hat{\boldsymbol{\phi}}_\pm + L_{\pm 0}\hat{\boldsymbol{\phi}}_0 + \hat{\boldsymbol{f}}_{\phi,\pm} \tag{C.3a}$$

$$0 = L_{0\pm}\hat{\boldsymbol{\phi}}_\pm + L_{00}\hat{\boldsymbol{\phi}}_0 + \hat{\boldsymbol{f}}_{\phi,0}. \tag{C.3b}$$

The zero eigenvalues, $\tilde{A}_{00}$, correspond to points in the base flow where the streamwise velocity is exactly zero or sonic. In practice, unless a grid point is placed exactly on the sonic line, we will have $\tilde{A}_{00}$ associated with wall boundary-conditions only, so that L_{00} will be invertible and we can eliminate $\hat{\boldsymbol{\phi}}_0$ as

$$\hat{\boldsymbol{\phi}}_0 = -L_{00}^{-1}(L_{0\pm}\hat{\boldsymbol{\phi}}_\pm + \hat{\boldsymbol{f}}_{\phi,0}). \tag{C.4}$$

We then define

$$M = \tilde{A}_{\pm\pm}^{-1}(L_{\pm\pm} - L_{\pm 0}L_{00}^{-1}L_{0\pm}), \quad \hat{\boldsymbol{g}} = \tilde{A}_{\pm\pm}^{-1}(\hat{\boldsymbol{f}}_{\phi,\pm} - L_{\pm 0}L_{00}^{-1}\hat{\boldsymbol{f}}_{\phi,0}), \tag{C.5}$$

to obtain the ODE

$$\frac{d\hat{\boldsymbol{\phi}}}{dx} = M\hat{\boldsymbol{\phi}}_\pm + \hat{\boldsymbol{g}}, \tag{C.6}$$

which can be treated as in the non-singular case.

Appendix D

PROOFS FOR OWNS-P AND OWNS-R

D.1 Proofs for OWNS-P

Proof: [Proof of Proposition 2.2.13] First note that (2.16b) through (2.16d) can be diagonalized using

$$(M - i\beta I)\hat{\boldsymbol{\phi}} = (VDV^{-1} - i\beta VV^{-1})V\boldsymbol{\psi} = V(D - i\beta I)\boldsymbol{\psi},$$

where V has full rank while $(D - i\beta I)$ is diagonal so that each scalar component of $\{\boldsymbol{\psi}^j\}_{j=-N_\beta}^{N_\beta}$ and $\boldsymbol{\psi}$ can be treated separately as

$$\begin{aligned}
(\alpha_k - \beta_-^j)\psi_k^{-j} - (\alpha_k - \beta_+^j)\psi_k^{-j-1} &= 0, \quad j = 1, \ldots, N_\beta - 1, \\
(\alpha_k - \beta_-^0)\psi_k^0 - (\alpha_k - \beta_+^0)\psi_k^{-1} &= (\alpha_k - \beta_-^0)\psi_k, \\
(\alpha_k - \beta_+^j)\psi_k^j - (\alpha_k - \beta_-^j)\psi_k^{j+1} &= 0, \quad j = 0, \ldots, N_\beta - 1,
\end{aligned}$$

for $k = 1, \ldots, N$. For the downstream-going modes we obtain

$$\psi_k^0 - \psi_k = \prod_{j=0}^{N_\beta - 1} \frac{\alpha_k - \beta_+^j}{\alpha_k - \beta_-^j} \psi_k^{-N_\beta} = F_k \psi_k^{-N_\beta}, \tag{D.1a}$$

$$\psi_k^{N_\beta} = \prod_{j=0}^{N_\beta - 1} \frac{\alpha_k - \beta_+^j}{\alpha_k - \beta_-^j} \psi_k^0 = F_k \psi_k^0, \tag{D.1b}$$

so that

$$F_{++}\boldsymbol{\psi}_+^{-N_\beta} = \boldsymbol{\psi}_+^0 - \boldsymbol{\psi}_+, \quad F_{++}\boldsymbol{\psi}_+^0 = \boldsymbol{\psi}_+^{N_\beta}, \tag{D.1c}$$

for $k = 1, \ldots, N_+$. Similarly, for the upstream-going modes we obtain

$$\psi_k^0 = \prod_{j=0}^{N_\beta - 1} \frac{\alpha_k - \beta_-^j}{\alpha_k - \beta_+^j} \psi_k^{N_\beta} = F_k^{-1} \psi_k^{N_\beta}, \tag{D.2a}$$

$$\psi_k^{-N_\beta} = \prod_{j=0}^{N_\beta - 1} \frac{\alpha_k - \beta_-^j}{\alpha_k - \beta_+^j} (\psi_k^0 - \psi_k) = F_k^{-1} (\psi_k^0 - \psi_k), \tag{D.2b}$$

so that

$$F_{--}^{-1}\boldsymbol{\psi}_-^{N_\beta} = \boldsymbol{\psi}_-^0, \quad F_{--}^{-1}(\boldsymbol{\psi}_-^0 - \boldsymbol{\psi}_-) = \boldsymbol{\psi}_-^{-N_\beta}, \tag{D.2c}$$

for $k = N_+ + 1, \ldots, N$. Next recall that

$$\begin{bmatrix} \hat{\boldsymbol{\phi}}_+ \\ \hat{\boldsymbol{\phi}}_- \end{bmatrix} = \begin{bmatrix} V_{++} & V_{+-} \\ V_{-+} & V_{--} \end{bmatrix} \begin{bmatrix} \boldsymbol{\psi}_+ \\ \boldsymbol{\psi}_- \end{bmatrix} = \begin{bmatrix} V_{++}\boldsymbol{\psi}_+ + V_{+-}\boldsymbol{\psi}_- \\ V_{-+}\boldsymbol{\psi}_+ + V_{--}\boldsymbol{\psi}_- \end{bmatrix}$$

so that (2.16a) and (2.16e) are equivalent to

$$\begin{aligned} \hat{\boldsymbol{\phi}}_+^{-N_\beta} &= V_{++}\boldsymbol{\psi}_+^{-N_\beta} + V_{+-}\boldsymbol{\psi}_-^{-N_\beta} = 0, \\ \hat{\boldsymbol{\phi}}_-^{N_\beta} &= V_{-+}\boldsymbol{\psi}_+^{N_\beta} + V_{--}\boldsymbol{\psi}_-^{N_\beta} = 0. \end{aligned}$$

or

$$\boldsymbol{\psi}_+^{-N_\beta} = -V_{++}^{-1}V_{+-}\boldsymbol{\psi}_-^{-N_\beta}, \quad \boldsymbol{\psi}_-^{N_\beta} = -V_{--}^{-1}V_{-+}\boldsymbol{\psi}_+^{N_\beta}.$$

We pre-multiply by F_{++} and F_{--}^{-1} to obtain

$$\begin{aligned} \boldsymbol{\psi}_+^0 - \boldsymbol{\psi}_+ = F_{++}\boldsymbol{\psi}_+^{-N_\beta} &= -F_{++}V_{++}^{-1}V_{+-}\boldsymbol{\psi}_-^{-N_\beta} = -F_{++}V_{++}^{-1}V_{+-}F_{--}^{-1}(\boldsymbol{\psi}_-^0 - \boldsymbol{\psi}_-), \\ \boldsymbol{\psi}_-^0 = F_{--}^{-1}\boldsymbol{\psi}_-^{N_\beta} &= -F_{--}^{-1}V_{--}^{-1}V_{-+}\boldsymbol{\psi}_+^{N_\beta} = -F_{--}^{-1}V_{--}^{-1}V_{-+}F_{++}\boldsymbol{\psi}_+^0, \end{aligned}$$

and rearranging yields

$$\begin{aligned} &\boldsymbol{\psi}_+^0 + F_{++}V_{++}^{-1}V_{+-}F_{--}^{-1}\boldsymbol{\psi}_-^0 = \boldsymbol{\psi}_+ + F_{++}V_{++}^{-1}V_{+-}F_{--}^{-1}\boldsymbol{\psi}_-, \\ &F_{--}^{-1}V_{--}^{-1}V_{-+}F_{++}\boldsymbol{\psi}_+^0 + \boldsymbol{\psi}_-^0 = 0, \end{aligned}$$

which in matrix form becomes

$$\begin{bmatrix} I_{++} & F_{++}V_{++}^{-1}V_{+-}F_{--}^{-1} \\ F_{--}^{-1}V_{--}^{-1}V_{-+}F_{++} & I_{--} \end{bmatrix} \begin{bmatrix} \boldsymbol{\psi}_+^0 \\ \boldsymbol{\psi}_-^0 \end{bmatrix} = \begin{bmatrix} I_{++} & F_{++}V_{++}^{-1}V_{+-}F_{--}^{-1} \\ 0 & 0 \end{bmatrix} \begin{bmatrix} \boldsymbol{\psi}_+ \\ \boldsymbol{\psi}_- \end{bmatrix}.$$

Using R_{N_β} from (2.17b), the above is equivalent to $R_{N_\beta}^{-1}\boldsymbol{\psi}^0 = ER_{N_\beta}^{-1}\boldsymbol{\psi}$, so that $\hat{\boldsymbol{\phi}}^0 = VR_{N_\beta}ER_{N_\beta}^{-1}V^{-1}\hat{\boldsymbol{\phi}} = P_{N_\beta}\hat{\boldsymbol{\phi}}_0$. Thus, we have shown that the action of the filter (2.16) can be applied using the projection matrix (2.17a). □

Proof: [Proof of Proposition 2.2.15] Clearly $P_{N_\beta} \to P$ if and only if $R_{N_\beta}^{-1} \to I$, while F is diagonal so that

$$\begin{aligned} (F_{++}V_{++}^{-1}V_{+-}F_{--}^{-1})_{mn} &= \prod_{j=0}^{N_\beta-1} \frac{\alpha_m - \beta_+^j}{\alpha_m - \beta_-^j}\frac{\alpha_n - \beta_-^j}{\alpha_n - \beta_+^j}(V_{++}^{-1}V_{+-})_{mn}, \\ (F_{--}^{-1}V_{--}^{-1}V_{-+}F_{++})_{nm} &= \prod_{j=0}^{N_\beta-1} \frac{\alpha_m - \beta_+^j}{\alpha_m - \beta_-^j}\frac{\alpha_n - \beta_-^j}{\alpha_n - \beta_+^j}(V_{++}^{-1}V_{+-})_{nm}, \end{aligned}$$

and $R_{N_\beta}^{-1} \to I$ if and only if (2.18) holds. □

Proof: [Proof of Proposition 2.2.16] First we show that if $\alpha_m \neq \alpha_n$ for all $m = i^{(+)}$ and $n = i^{(-)}$ then we can always choose recursion parameters such that the OWNS-O approximation converges. Without loss of generality, assume that $N_+ \leq N_-$. Then

$$\prod_{j=0}^{N_+-1} \frac{|\alpha_m - \beta_+^j|}{|\alpha_m - \beta_-^j|} \frac{|\alpha_n - \beta_-^j|}{|\alpha_n - \beta_+^j|} = 0, \quad \forall m = i^{(+)}, n = i^{(-)},$$

were we have used

$$\begin{aligned}
\alpha_m - \beta_+^{m-1} &= 0, \quad \forall m = 1, \ldots, N_+, \\
\alpha_m - \beta_-^{j-1} &\neq 0, \quad \forall m, j = 1, \ldots, N_+, \\
\alpha_n - \beta_+^{j-1} &\neq 0, \quad \forall j = 1, \ldots, N_+, \quad \forall n = 1, \ldots, N_-.
\end{aligned}$$

An identical procedure for $N_- < N_+$ proves that $\alpha_m \neq \alpha_n$ for all $m = i^{(+)}$ and $n = i^{(-)}$ is a sufficient condition for convergence.

If $\alpha_{\tilde{m}} = \alpha_{\tilde{n}}$ for some some $\tilde{m} = i^{(+)}$ and $\tilde{n} = i^{(-)}$, then

$$(F_{--}^{-1}V_{--}^{-1}V_{-+}F_{++})_{\tilde{n}\tilde{m}} = \prod_{j=0}^{N_\beta-1} \frac{\alpha_{\tilde{m}} - \beta_+^j}{\alpha_{\tilde{m}} - \beta_-^j} \frac{\alpha_{\tilde{n}} - \beta_-^j}{\alpha_{\tilde{n}} - \beta_+^j} (V_{--}^{-1}V_{-+})_{\tilde{n}\tilde{m}} = (V_{--}^{-1}V_{-+})_{\tilde{n}\tilde{m}}$$

so that $R_{N_\beta}^{-1} \neq I$, no matter how the recursion parameters are chosen, proving the necessity of the condition. □

Theorem D.1.1 (Block matrix inverse) *If a matrix is partitioned into four blocks such that*

$$R = \begin{bmatrix} R_{++} & R_{+-} \\ R_{-+} & R_{--} \end{bmatrix}, \tag{D.3a}$$

then it can be inverted blockwise as

$$R^{-1} = \begin{bmatrix} R_{++} & R_{+-} \\ R_{-+} & R_{--} \end{bmatrix}^{-1} = \begin{bmatrix} [R^{-1}]_{++} & [R^{-1}]_{+-} \\ [R^{-1}]_{-+} & [R^{-1}]_{--} \end{bmatrix}, \tag{D.3b}$$

where

$$[R^{-1}]_{++} = (R_{++} - R_{+-}R_{--}^{-1}R_{-+})^{-1}, \tag{D.3c}$$

$$[R^{-1}]_{+-} = -(R_{++} - R_{+-}R_{--}^{-1}R_{-+})^{-1}R_{+-}R_{--}^{-1}, \tag{D.3d}$$

$$[R^{-1}]_{-+} = -R_{--}^{-1}R_{-+}(R_{++} - R_{+-}R_{--}^{-1}R_{-+})^{-1}, \tag{D.3e}$$

$$[R^{-1}]_{--} = R_{--}^{-1} + R_{--}^{-1}R_{-+}(R_{++} - R_{+-}R_{--}^{-1}R_{-+})^{-1}R_{+-}R_{--}^{-1}. \tag{D.3f}$$

Theorem D.1.2 (Neumann series) *For a matrix R, if the sum* $\sum_{k=0}^{\infty} R^k$ *converges to a finite value, then*

$$(I - R)^{-1} = \sum_{k=0}^{\infty} R^k. \tag{D.4}$$

The proof of Proposition 2.2.17 relies on two theorems. Theorem D.1.1 provides an expression for the inverse of a block matrix, while theorem D.1.2 provides conditions under which $\|(I_{++} - F_{++}V_{++}^{-1}V_{+-}F_{--}^{-2}V_{--}^{-1}V_{-+}F_{++})^{-1}\|$ is finite.

Proof: [Proof of Proposition 2.2.17] First note that

$$\begin{aligned}\|P - P_{N_\beta}\| &= \|VEV^{-1} - VR_{N_\beta}^{-1}ER_{N_\beta}V^{-1}\| \\ &= \|V(E - R_{N_\beta}^{-1}ER_{N_\beta})V^{-1}\| \\ &\leq \|V\|\|E - R_{N_\beta}^{-1}ER_{N_\beta}\|\|V^{-1}\|,\end{aligned}$$

while by theorem D.1.1 for the inverse of a block matrix

$$\begin{aligned}R_{N_\beta}^{-1}ER_{N_\beta} &= \begin{bmatrix}[R_{N_\beta}^{-1}]_{++} & [R_{N_\beta}^{-1}]_{+-} \\ [R_{N_\beta}^{-1}]_{-+} & [R_{N_\beta}^{-1}]_{--}\end{bmatrix}\begin{bmatrix}I_{++} & 0 \\ 0 & 0\end{bmatrix}\begin{bmatrix}[R_{N_\beta}]_{++} & [R_{N_\beta}]_{+-} \\ [R_{N_\beta}]_{-+} & [R_{N_\beta}]_{--}\end{bmatrix} \\ &= \begin{bmatrix}[R_{N_\beta}^{-1}]_{++} & 0 \\ [R_{N_\beta}^{-1}]_{-+} & 0\end{bmatrix}\begin{bmatrix}[R_{N_\beta}]_{++} & [R_{N_\beta}]_{+-} \\ 0 & 0\end{bmatrix} \\ &= \begin{bmatrix}[R_{N_\beta}^{-1}]_{++}[R_{N_\beta}]_{++} & [R_{N_\beta}^{-1}]_{++}[R_{N_\beta}]_{+-} \\ [R_{N_\beta}^{-1}]_{-+}[R_{N_\beta}]_{++} & [R_{N_\beta}^{-1}]_{-+}[R_{N_\beta}]_{+-}\end{bmatrix}\end{aligned}$$

so that

$$E - R_{N_\beta}^{-1}ER_{N_\beta} = \begin{bmatrix}[R_{N_\beta}^{-1}]_{++}[R_{N_\beta}]_{++} - I_{++} & [R_{N_\beta}^{-1}]_{++}[R_{N_\beta}]_{+-} \\ [R_{N_\beta}^{-1}]_{-+}[R_{N_\beta}]_{++} & [R_{N_\beta}^{-1}]_{-+}[R_{N_\beta}]_{+-}\end{bmatrix}.$$

By the triangle inequality

$$\begin{aligned}\|E - R_{N_\beta}^{-1}ER_{N_\beta}\| \leq{}& \|[R_{N_\beta}^{-1}]_{++}[R_{N_\beta}]_{++} - I_{++}\| + \|[R_{N_\beta}^{-1}]_{++}[R_{N_\beta}]_{+-}\| \\ &+ \|[R_{N_\beta}^{-1}]_{-+}[R_{N_\beta}]_{++}\| + \|[R_{N_\beta}^{-1}]_{-+}[R_{N_\beta}]_{+-}\|,\end{aligned}$$

while

$$\begin{aligned}[R_{N_\beta}]_{++} &= I_{++} \\ [R_{N_\beta}]_{+-} &= F_{++}V_{++}^{-1}V_{+-}F_{--}^{-1} \\ [R_{N_\beta}^{-1}]_{++} &= (I_{++} - F_{++}V_{++}^{-1}V_{+-}F_{--}^{-2}V_{--}^{-1}V_{-+}F_{++})^{-1}, \\ [R_{N_\beta}^{-1}]_{-+} &= -F_{--}^{-1}V_{--}^{-1}V_{-+}F_{++}(I_{++} - F_{++}V_{++}^{-1}V_{+-}F_{--}^{-2}V_{--}^{-1}V_{-+}F_{++})^{-1},\end{aligned}$$

so that

$$\begin{aligned}
\|[R_{N_\beta}^{-1}]_{++}[R_{N_\beta}]_{++} - I_{++}\| &\le \|F_{++}V_{++}^{-1}V_{+-}F_{--}^{-1}\| \times \|F_{--}^{-1}V_{--}^{-1}V_{-+}F_{++}\| \\
&\quad \times \|(I_{++} - F_{++}V_{++}^{-1}V_{+-}F_{--}^{-2}V_{--}^{-1}V_{-+}F_{++})^{-1}\|, \\
\|[R_{N_\beta}^{-1}]_{++}[R_{N_\beta}]_{+-}\| &\le \|F_{++}V_{++}^{-1}V_{+-}F_{--}^{-1}\| \\
&\quad \times \|(I_{++} - F_{++}V_{++}^{-1}V_{+-}F_{--}^{-2}V_{--}^{-1}V_{-+}F_{++})^{-1}\|, \\
\|[R_{N_\beta}^{-1}]_{-+}[R_{N_\beta}]_{++}\| &\le \|F_{--}^{-1}V_{--}^{-1}V_{-+}F_{++}\| \\
&\quad \times \|(I_{++} - F_{++}V_{++}^{-1}V_{+-}F_{--}^{-2}V_{--}^{-1}V_{-+}F_{++})^{-1}\|, \\
\|[R_{N_\beta}^{-1}]_{-+}[R_{N_\beta}]_{+-}\| &\le \|F_{--}^{-1}V_{--}^{-1}V_{-+}F_{++}\| \times \|F_{++}V_{++}^{-1}V_{+-}F_{--}^{-1}\| \\
&\quad \times \|(I_{++} - F_{++}V_{++}^{-1}V_{+-}F_{--}^{-2}V_{--}^{-1}V_{-+}F_{++})^{-1}\|.
\end{aligned}$$

Combining these results yields

$$\begin{aligned}
\|E - R_{N_\beta}^{-1}ER_{N_\beta}\| \le \|(I_{++} - F_{++}V_{++}^{-1}V_{+-}F_{--}^{-2}V_{--}^{-1}V_{-+}F_{++})^{-1}\|\big(&\|F_{++}V_{++}^{-1}V_{+-}F_{--}^{-1}\| \\
&+ 2\|F_{++}V_{++}^{-1}V_{+-}F_{--}^{-1}\|\|F_{--}^{-1}V_{--}^{-1}V_{-+}F_{++}\| + \|F_{--}^{-1}V_{--}^{-1}V_{-+}F_{++}\|\big).
\end{aligned}$$

Next we note that

$$\sum_{k=0}^{\infty}(F_{++}V_{++}^{-1}V_{+-}F_{--}^{-2}V_{--}^{-1}V_{-+}F_{++})^k$$

is finite if

$$\|F_{++}\|\|F_{--}^{-1}\| < (\|V_{++}^{-1}V_{+-}\|\|V_{--}^{-1}V_{-+}\|)^{-1/2}.$$

Take some $\hat{\epsilon} > 0$ such that $\hat{\epsilon} \ll 1$ and define

$$\epsilon = \min\{\hat{\epsilon}, \|V_{++}^{-1}V_{+-}\|^{-1/2}\|V_{--}^{-1}V_{-+}\|^{-1/2}\}.$$

Then assuming $\|F_{++}\|\|F_{--}^{-1}\| < \epsilon$, theorem D.1.2 for Neumann series applies and

$$\begin{aligned}
&\|(I_{++} - F_{++}V_{++}^{-1}V_{+-}F_{--}^{-2}V_{--}^{-1}V_{-+}F_{++})^{-1}\| \\
&\le \sum_{k=0}^{\infty}\|F_{++}V_{++}^{-1}V_{+-}F_{--}^{-2}V_{--}^{-1}V_{-+}F_{++}\|^k \\
&\le \sum_{k=0}^{\infty}(\|F_{++}\|^2\|F_{--}^{-1}\|^2\|V_{++}^{-1}V_{+-}\|\|V_{--}^{-1}V_{-+}\|)^k \\
&= 1 + \|F_{++}\|^2\|F_{--}^{-1}\|^2\|V_{++}^{-1}V_{+-}\|\|V_{--}^{-1}V_{-+}\| + O(\|F_{++}\|^4\|F_{--}^{-1}\|^4),
\end{aligned}$$

while

$$\begin{aligned}
\|F_{++}V_{++}^{-1}V_{+-}F_{--}^{-1}\| &\le \|F_{++}\|\|F_{--}^{-1}\|\|V_{++}^{-1}V_{+-}\|, \\
\|F_{--}^{-1}V_{--}^{-1}V_{-+}F_{++}\| &\le \|F_{++}\|\|F_{--}^{-1}\|\|V_{--}^{-1}V_{-+}\|,
\end{aligned}$$

so that

$$\begin{aligned}\|E - R_{N_\beta}^{-1} E R_{N_\beta}\| \leq\ & [1 + \|F_{++}\|^2 \|F_{--}^{-1}\|^2 \|V_{++}^{-1} V_{+-}\| \|V_{--}^{-1} V_{-+}\| + O(\epsilon^4)] \\ & \times \|F_{++}\| \|F_{--}^{-1}\| [\|V_{++}^{-1} V_{+-}\| + \|V_{--}^{-1} V_{-+}\| \\ & + 2\|F_{++}\| \|F_{--}^{-1}\| \|V_{--}^{-1} V_{-+}\| \|V_{++}^{-1} V_{+-}\|] \\ =\ & \|F_{++}\| \|F_{--}^{-1}\| \left(\|V_{++}^{-1} V_{+-}\| + \|V_{--}^{-1} V_{-+}\|\right) + O(\epsilon^2),\end{aligned}$$

and

$$\|P_{N_\beta} - P\| \leq \|V\| \|F_{++}\| \|F_{--}^{-1}\| \left(\|V_{++}^{-1} V_{+-}\| + \|V_{--}^{-1} V_{-+}\|\right) \|V^{-1}\| + O(\epsilon^2),$$

where we have used $\|F_{++}\| \|F_{--}^{-1}\| < \epsilon$. □

Proof: [Proof of Proposition 2.2.22] Note that $\|PM - MP\| = 0$ while

$$\begin{aligned}\|P_{N_\beta} M - M P_{N_\beta}\| &= \|(P_{N_\beta} - P)M + M(P - P_{N_\beta})\| \\ &\leq 2\|P_{N_\beta} - P\| \|M\| \\ &\leq 2\|V\| \|F_{++}\| \|F_{--}^{-1}\| \left(\|V_{++}^{-1} V_{+-}\|\right. \\ &\quad \left. + \|V_{--}^{-1} V_{-+}\|\right) \|V^{-1}\| \|M\| + O(\epsilon^2),\end{aligned}$$

by Proposition 2.2.17. □

Proof: [Proof of Proposition 2.2.18] A downstream-going mode associated with α_m is retained accurately if $\psi_m^0 - \psi_m = 0$, while by equation (D.1a) we have

$$\psi_m^0 - \psi_m = \prod_{j=0}^{N_\beta - 1} \frac{\alpha_m - \beta_+^j}{\alpha_m - \beta_-^j} \psi_m^{-N_\beta} = 0$$

since $\alpha_m = \beta_+^j$ for some β_+^j, while $\alpha_m \neq \beta_-^j$ for all β_-^j. An upstream-going mode associated with α_n is removed if $\psi_n^0 = 0$, while by equation (D.2a) we have

$$\psi_n^0 = \prod_{j=0}^{N_\beta - 1} \frac{\alpha_n - \beta_-^j}{\alpha_n - \beta_+^j} \psi_n^{N_\beta} = 0$$

since $\alpha_n = \beta_-^j$ for some β_-^j, while $\alpha_n \neq \beta_+^j$ for all β_+^j. □

D.2 Proofs for OWNS-R

Proof: [Proof of Proposition 2.2.25] First note that

$$\begin{aligned} E_{N_\beta}^{(k)} &= \left(1 + c\prod_{j=1}^{N_\beta}\frac{\alpha_k - \beta_+^j}{\alpha_k - \beta_-^j}\right)^{-1} \\ &= \left(\frac{\prod_{j=1}^{N_\beta}(\alpha_k - \beta_-^j) + c\prod_{j=1}^{N_\beta}(\alpha_k - \beta_+^j)}{\prod_{j=1}^{N_\beta}(\alpha_k - \beta_-^j)}\right)^{-1} \\ &= \frac{\prod_{j=1}^{N_\beta}(\alpha_k - \beta_-^j)}{\prod_{j=1}^{N_\beta}(\alpha_k - \beta_-^j) + c\prod_{j=1}^{N_\beta}(\alpha_k - \beta_+^j)}, \end{aligned}$$

for $k = 1, \ldots, N$, then observe that

$$P_{N_\beta}^{(R)} = (I + cZ)^{-1} = [V(I + cF)V^{-1}]^{-1} = V(I + cF)^{-1}V^{-1} = VE_{N_\beta}V^{-1}.$$

□

Proof: [Proof of Proposition 2.2.27] First note that

$$P_{N_\beta}^{(R)}P_{N_\beta}^{(R)} = VE_{N_\beta}V^{-1}VE_{N_\beta}V^{-1} = VE_{N_\beta}^2V^{-1},$$

so that $P_{N_\beta}^{(R)}$ is a projection matrix if and only if $E_{N_\beta}^2 = E_{N_\beta}$. Since E_{N_β} is diagonal, we can consider each entry separately so that we must have $E_{N_\beta,k}^2 = E_{N_\beta,k}$ for $k = 1, \ldots, N$. We know that $E_{N_\beta,k}^2 = E_{N_\beta,k}$ if and only if $E_{N_\beta,k} = 0$ or $E_{N_\beta,k} = 1$, concluding the proof. □

Proof: [Proof of Proposition 2.2.31] First we show that if $\alpha_m \neq \alpha_n$ for all pairs of $m = i^{(+)}$ and $n = i^{(-)}$, then we can always choose recursion parameters such that the OWNS-R approximation converges. Note that

$$\begin{aligned} E_{N_\beta}^{(k)} &= \frac{\prod_{j=1}^{N}(\alpha_k - \beta_-^j)}{\prod_{j=1}^{N}(\alpha_k - \beta_-^j) + 0} = 1, \quad k = i^{(+)}, \\ E_{N_\beta}^{(k)} &= \frac{0}{0 + c\prod_{j=1}^{N}(\alpha_k - \beta_+^j)} = 0, \quad k = i^{(-)}, \end{aligned}$$

where $\prod_{j=1}^{N}(\alpha_k - \beta_-^j) \neq 0$ for $k = i^{(+)}$ and $\prod_{j=1}^{N}(\alpha_k - \beta_+^j) \neq 0$ for $k = i^{(-)}$ by construction.

Next we show that if $\alpha_{\tilde{m}} = \alpha_{\tilde{n}}$ for some $\tilde{m} = i^{(+)}$ and $\tilde{n} = i^{(-)}$, then there does not exist any choice of recursion parameters such that $P_{N_\beta}^{(R)} \to P$. By contradiction, suppose

there exists recursion parameters such that $P^{(R)}_{N_\beta}$ converges to P when $\alpha_{\tilde{m}} = \alpha_{\tilde{n}}$ for some $\tilde{m} = i^{(+)}$ and $\tilde{n} = i^{(+)}$. Then we must have $E^{(\tilde{m})}_{N_\beta} \to 1$ and $E^{(\tilde{n})}_{N_\beta} \to 0$, but $E^{(\tilde{m})}_{N_\beta} = E^{(\tilde{n})}_{N_\beta}$ and $1 \neq 0$, leading to a contradiction. □

Proof: [Proof of Proposition 2.2.34] Note that

$$\|P - P^{(R)}_{N_\beta}\| = \|VEV^{-1} - VE_{N_\beta}V^{-1}\| \leq \|V\|\|E - E_{N_\beta}\|\|V^{-1}\|,$$

where for the downstream-going modes

$$\begin{aligned} E^{(k)} - E^{(k)}_{N_\beta} &= 1 - \frac{\prod_{j=1}^{N}(\alpha_k - \beta^j_-)}{\prod_{j=1}^{N}(\alpha_k - \beta^j_-) + c\prod_{j=1}^{N}(\alpha_k - \beta^j_+)} \\ &= \frac{c\prod_{j=1}^{N}(\alpha_k - \beta^j_+)}{\prod_{j=1}^{N}(\alpha_k - \beta^j_-) + c\prod_{j=1}^{N}(\alpha_k - \beta^j_+)} \\ &= \frac{cF_k}{1 + cF_k}, \end{aligned}$$

for $k = i^{(+)}$, while for the upstream-going modes

$$\begin{aligned} E^{(k)} - E^{(k)}_{N_\beta} &= 0 - \frac{\prod_{j=1}^{N}(\alpha_k - \beta^j_-)}{\prod_{j=1}^{N}(\alpha_k - \beta^j_-) + c\prod_{j=1}^{N}(\alpha_k - \beta^j_+)} \\ &= -\frac{F_k^{-1}}{F_k^{-1} + c}, \end{aligned}$$

for $k = i^{(-)}$. Assuming that $|F_k| < \epsilon \ll 1$ for $k = i^{(+)}$ and $|F_k^{-1}| < \epsilon \ll 1$ for $k = i^{(-)}$ we obtain

$$\begin{aligned} |E^{(k)} - E^{(k)}_{N_\beta}| &= |c||F_k| + O(|F_k|^2), \quad k = i^{(+)} \\ |E^{(k)} - E^{(k)}_{N_\beta}| &= |F_k^{-1}| + O(|F_k^{-1}|^2), \quad k = i^{(-)}. \end{aligned}$$

Since $E - E_{N_\beta}$ is a diagonal matrix we obtain

$$\begin{aligned} \|E - E_{N_\beta}\| &= \max\Big\{\max_{k=1,\ldots,N_+}|c||F_k| + O(\epsilon^2), \max_{k=N_++1,\ldots,N}|F_k^{-1}| + O(\epsilon^2)\Big\} \\ &= \max\big\{|c|\|F_{++}\|, \|F_{--}^{-1}\|\big\} + O(\epsilon^2), \end{aligned}$$

so that

$$\|P - P^{(R)}_{N_\beta}\| \leq \|V\| \max\big\{|c|\|F_{++}\|, \|F_{--}^{-1}\|\big\}\|V^{-1}\| + O(\epsilon^2).$$

□

Proof: [Proof of Proposition 2.2.35] If $\beta_+^j = \alpha_m$ for downstream-going mode α_m, then $E_{N_\beta}^{(m)} = 1$. Taking $\boldsymbol{\psi}$ such that $\psi_k = 0$ for $k \neq m$ and $\psi_m = 1$, we have $P_{N_\beta}^{(R)} V\boldsymbol{\psi} = VE_{N_\beta}\boldsymbol{\psi} = V\boldsymbol{\psi}$. Similarly, if $\beta_-^j = \alpha_n$ for upstream-going mode α_n, then $E_{N_\beta}^{(}n) = 0$. Taking $\boldsymbol{\psi}$ such that $\psi_k = 0$ for $k \neq n$ and $\psi_n = 1$, we have $P_{N_\beta}^{(R)} V\boldsymbol{\psi} = VE_{N_\beta}\boldsymbol{\psi} = 0$. □

Proof: [Proof of Proposition 2.2.38] Note that

$$(P_{N_\beta}^{(R)})^n = VE_{N_\beta}^n V^{-1},$$

and that

$$\lim_{n\to\infty} |E_{N_\beta}^{(k)}|^n = \begin{cases} 0 & |E_{N_\beta}^{(k)}| < 0, \\ 1 & |E_{N_\beta}^{(k)}| = 1, \\ \infty & |E_{N_\beta}^{(k)}| > 1. \end{cases}$$

If $|E_{N_\beta}^{(k)}| < 1$, then mode k will be removed by repeated applications of $P_{N_\beta}^{(R)}$, which is desirable for upstream-going modes, but not for downstream-going modes. In contrast, if $|E_{N_\beta}^{(k)}| > 1$, then mode k will grow without bound through repeated applications of $P_{N_\beta}^{(R)}$, which is undesirable for both upstream- and downstream-going modes. If $E_{N_\beta}^{(k)} = 1$, then mode k will be accurately retained. Therefore, repeated applications of $P_{N_\beta}^{(R)}$ introduces error unless unless $|E_{N_\beta}^{(n)}| < 1$ for all $n = i^{(-)}$, and $E_{N_\beta}^{(m)} = 1$ for all $m = i^{(+)}$. □

Proof: [Proof or Proposition 2.2.41] Note that

$$E_{N_\beta}^{(k)} = \frac{\prod_{j=1}^{N_\beta}(\alpha_k - \beta_-^j)}{\prod_{j=1}^{N_\beta}(\alpha_k - \beta_-^j) + \prod_{j=1}^{N_\beta}(\alpha_k - \beta_+^j)} = \frac{1}{2}\frac{\prod_{j=1}^{N_\beta}(\alpha_k - \beta_-^j)}{\prod_{j=1}^{N_\beta}(\alpha_k - \beta_*^j)},$$

so that

$$\begin{aligned} P_{N_\beta}^{(R)} &= VE_{N_\beta}V^{-1} \\ &= \frac{1}{2}V\prod_{j=1}^{N_\beta}(D - \beta_*^j I)^{-1}(D - \beta_-^j I)V^{-1} \\ &= \frac{1}{2}\prod_{j=1}^{N_\beta}(M - \beta_*^j I)^{-1}(M - \beta_-^j I), \end{aligned}$$

which can be-rearranged into (2.26). □

Appendix E

A VARIATIONAL APPROACH TO OWNS

We will now consider a variational approach to OWNS. Consider the equation for the downstream-going modes in characteristic variables

$$\frac{\partial \hat{\boldsymbol{\phi}}'_{\pm}}{\partial x} = PM\hat{\boldsymbol{\phi}}'_{\pm} + P\hat{\boldsymbol{g}}. \tag{3.10}$$

We note that

$$M = VDV^{-1} = VDU = \begin{bmatrix} V_{++} & V_{+-} \\ V_{-+} & V_{--} \end{bmatrix} \begin{bmatrix} D_{++} & 0 \\ 0 & D_{--} \end{bmatrix} \begin{bmatrix} U_{++} & U_{+-} \\ U_{-+} & U_{--} \end{bmatrix},$$

where $U = V^{-1}$, while the projection operator is defined such that

$$P = \begin{bmatrix} V_{++} & V_{+-} \\ V_{-+} & V_{--} \end{bmatrix} \begin{bmatrix} I_{++} & 0 \\ 0 & 0 \end{bmatrix} \begin{bmatrix} U_{++} & U_{+-} \\ U_{-+} & U_{--} \end{bmatrix} = \begin{bmatrix} V_{++}U_{++} & V_{++}U_{+-} \\ V_{-+}U_{++} & V_{-+}U_{+-} \end{bmatrix}.$$

M has full rank ($N_{\pm}$), while P is rank-deficient unless there are no upstream-going characteristics ($N_{-} = 0$), since $\text{rank}(P) = N_{+} \leq N_{\pm}$, while

$$P^H = \begin{bmatrix} U^H_{++}V^H_{++} & V^H_{-+}U^H_{++} \\ U^H_{+-}V^H_{++} & V^H_{-+}U^H_{+-} \end{bmatrix}.$$

We further define the left and right bases

$$P_L = \begin{bmatrix} V_{++} \\ V_{-+} \end{bmatrix}, \quad P^H_R = \begin{bmatrix} U_{++} & U_{+-} \end{bmatrix},$$

so that

$$P_L P^H_R = \begin{bmatrix} V_{++} \\ V_{-+} \end{bmatrix} \begin{bmatrix} U_{++} & U_{+-} \end{bmatrix} = \begin{bmatrix} V_{++}U_{++} & V_{++}U_{+-} \\ V_{-+}U_{++} & V_{-+}U_{+-} \end{bmatrix} = P,$$

while

$$P^H_R P_L = \begin{bmatrix} U_{++} & U_{+-} \end{bmatrix} \begin{bmatrix} V_{++} \\ V_{-+} \end{bmatrix} = U_{++}V_{++} + U_{+-}V_{-+} = I_{++},$$

where we have used

$$UV = \begin{bmatrix} U_{++}V_{++} + U_{+-}V_{-+} & U_{++}V_{+-} + U_{+-}V_{--} \\ U_{-+}V_{++} + U_{--}V_{-+} & U_{-+}V_{+-} + U_{--}V_{--} \end{bmatrix} = \begin{bmatrix} I_{++} & 0 \\ 0 & I_{--} \end{bmatrix} = I_{\pm\pm}.$$

It is shown in Towne et al. (2022) that $P^2 = P$, so that P is a projection.

E.1 Petrov-Galerkin method

The (Bubnov-)Galerkin method requires an orthogonal projection, while the Petrov-Galerkin method does not. If M is a normal operator, then $M = VDV^H$ by the spectral theorem so that P is self-adjoint and thus orthogonal. In general, M is non-normal, so we consider only the Petrov-Galerkin approach.

We consider the space $\mathcal{V}$ of elliptic solutions

$$\mathcal{V} \equiv \{\boldsymbol{\phi}_\pm \mid \boldsymbol{\phi}_\pm \text{ is bounded}\},$$

which we use to define the trial space $\mathcal{V}_+$ of downstream-going solutions

$$\mathcal{V}_+ \equiv \{\boldsymbol{\phi}_\pm \in \mathcal{V} \mid \boldsymbol{\phi}_\pm = P\boldsymbol{\phi}_\pm\},$$

and the test space

$$\mathcal{W}_+ \equiv \{\boldsymbol{w} \in \mathcal{V} \mid \boldsymbol{w} = P^H\boldsymbol{w}\}.$$

Any solution in the trial space and can be expressed as

$$\boldsymbol{\phi}_\pm = P\boldsymbol{\phi}_\pm = P_L P_R^H \boldsymbol{\phi}_\pm = P_L\boldsymbol{\alpha}, \quad \boldsymbol{\alpha} = P_R^H\boldsymbol{\phi} \in \mathbb{C}^{N_+},$$

while any test function can be expressed as

$$\boldsymbol{w} = P^H\boldsymbol{w} = P_R P_L^H \boldsymbol{w} = P_R\boldsymbol{\beta}, \quad \boldsymbol{\beta} = P_L^H\boldsymbol{w} \in \mathbb{C}^{N_+}.$$

We now consider the weak form of problem (3.9): find $\hat{\boldsymbol{\phi}}_\pm \in \mathcal{V}_+$ such that

$$\boldsymbol{w}^H \frac{\partial \hat{\boldsymbol{\phi}}_\pm}{\partial x} = \boldsymbol{w}^H M\hat{\boldsymbol{\phi}}_\pm + \boldsymbol{w}^H\hat{\boldsymbol{g}}, \quad \forall \boldsymbol{w} \in \mathcal{W}_+.$$

Choosing $\boldsymbol{\beta}_i = \hat{\boldsymbol{e}}_i$, where $\hat{\boldsymbol{e}}_i$ is the unit vector associated with the ith axis, we state our problem: find $\boldsymbol{\alpha} \in \mathbb{C}^{N_+}$ such that

$$P_R^H \frac{\partial (P_L\boldsymbol{\alpha})}{\partial x} = P_R^H M P_L\boldsymbol{\alpha} + P_R^H\hat{\boldsymbol{g}}. \tag{E.1}$$

E.1.1 Constant-coefficient system

If the problem has constant coefficients (in the streamwise direction), then it is straightforward to show that if $\boldsymbol{\alpha}$ is a solution to (E.1), then $P_L\boldsymbol{\alpha}$ is a solution to (3.10). We left multiply (E.1) by P_L to obtain

$$\frac{\partial (P_L\boldsymbol{\alpha})}{\partial x} = P[MP_L\boldsymbol{\alpha} + \hat{\boldsymbol{g}}], \tag{E.2}$$

where we have used that $PP_L\boldsymbol{\alpha} = P_L\boldsymbol{\alpha}$ and that P is not a function of x. We take the difference of (E.2) and (3.10) to obtain

$$\frac{\partial(P_L\boldsymbol{\alpha} - \boldsymbol{\phi}'_\pm)}{\partial x} - PM[P_L\boldsymbol{\alpha} - \boldsymbol{\phi}'_\pm] = \big(\frac{\partial}{\partial x} - M\big)[P_L\boldsymbol{\alpha} - \boldsymbol{\phi}'_\pm] = 0$$

and we use that $\frac{\partial}{\partial x} - M$ has full rank to assert that the above equation is satisfied if and only if $P_L\boldsymbol{\alpha} = \boldsymbol{\phi}'_\pm$.

We can similarly show that the projection of $\boldsymbol{\phi}'_\pm$ into the space $\mathcal{V}_+$, $\boldsymbol{\alpha}_\pm = P_R^H\boldsymbol{\phi}'_\pm$, satisfies (E.1). First we note that $\boldsymbol{\phi}'_\pm = P\boldsymbol{\phi}'_\pm = P_LP_R^H\boldsymbol{\phi}'_\pm = P_L\boldsymbol{\alpha}_\pm$, then we left multiply (3.10) by P_R^H to obtain

$$P_R^H\frac{\partial(P_L\boldsymbol{\alpha}_\pm)}{\partial x} = P_R^HP[MP_L\boldsymbol{\alpha}_\pm + \hat{\boldsymbol{g}}] = P_R^H[MP_L\boldsymbol{\alpha}_\pm + \hat{\boldsymbol{g}}]. \tag{E.3}$$

The difference of (E.1) and (E.3) yields

$$P_R^H\frac{\partial(P_L[\boldsymbol{\alpha} - \boldsymbol{\alpha}_\pm])}{\partial x} - P_R^HMP_L[\boldsymbol{\alpha} - \boldsymbol{\alpha}_\pm] = P_R^H\Big(\frac{\partial}{\partial x} - M\Big)P_L[\boldsymbol{\alpha} - \boldsymbol{\alpha}_\pm] = 0,$$

and we use that $P_R^H\big(\frac{\partial}{\partial x} - M\big)P_L$ has full rank to assert that $\boldsymbol{\alpha} = P_R^H\boldsymbol{\phi}'_\pm = \boldsymbol{\alpha}_\pm$. Therefore, we conclude for a constant-coefficient system that (E.1) and (3.10) are equivalent problems.

E.1.2 Variable-coefficient system

If the coefficients vary in x, then we can show that the projection of $\boldsymbol{\phi}'_\pm$ onto $\mathcal{V}_+$ satisfies (E.1) using the procedure outline for the constant-coefficient system. However, we cannot show that $P_L\boldsymbol{\alpha}$ is a solution to (3.10). Let us assume that $P_L\boldsymbol{\alpha}$ is a solution to (3.10), then we left multiply (E.1) by P_L to obtain

$$P\frac{\partial(P_L\boldsymbol{\alpha})}{\partial x} = PMP_L\boldsymbol{\alpha} + P_R^H\hat{\boldsymbol{g}}. \tag{E.4}$$

If we take the difference of the above equation with (3.10), then we obtain

$$P\frac{\partial(P_L\boldsymbol{\alpha})}{\partial x} - \frac{\partial\boldsymbol{\phi}'_\pm}{\partial x} - PM[P_L\boldsymbol{\alpha} - \boldsymbol{\phi}'_\pm] = 0, \tag{E.5}$$

and we can no longer assert that $P_L\boldsymbol{\alpha} = \boldsymbol{\phi}'_\pm$.

Let us instead consider the problems that result from discretizing in the streamwise direction. Following discretization with an s-order BDF scheme we obtain the fully-discrete form of (3.9)

$$\sum_{j=0}^{s-1} c^{(j)}\boldsymbol{\phi}_\pm^{(n+1-j)} = \Delta x[M^{(n+1)}\boldsymbol{\phi}_\pm^{(n+1)} + \boldsymbol{g}^{(n+1)}].$$

At station $n+1$, the Petrov-Galerkin approach yields the problem

$$c^{(0)}\boldsymbol{\alpha}^{(n+1)} = \Delta x P_R^{(n+1)H}[M^{(n+1)}P_L^{(n+1)}\boldsymbol{\alpha}^{(n+1)} + \boldsymbol{g}^{(n+1)}] - \sum_{j=1}^{s-1} c^{(j)} P_R^{(n+1)H}\boldsymbol{\phi}_{\pm}^{(n+1-j)}. \tag{E.6}$$

Similarly, if we apply the OWNS projection operator, $P^{(n+1)}$, to the discrete form of (3.9) we obtain

$$c^{(0)}\boldsymbol{\phi}_{\pm}'^{(n+1)} = \Delta x P^{(n+1)}[M^{(n+1)}\boldsymbol{\phi}_{\pm}'^{(n+1)} + \boldsymbol{g}^{(n+1)}] - \sum_{j=1}^{s-1} c^{(j)} P^{(n+1)}\boldsymbol{\phi}_{\pm}'^{(n+1-j)}. \tag{E.7}$$

We left multiply (E.6) by $P_L^{(n+1)}$ and take the difference with (E.7) to obtain

$$\left(c^{(0)}I_{\pm\pm} - \Delta x M^{(n+1)}\right)[P_L^{(n+1)}\boldsymbol{\alpha}^{(n+1)} - \boldsymbol{\phi}_{\pm}^{(n+1)\prime}] = 0, \tag{E.8}$$

and we use that $c^{(0)}I_{\pm\pm} - \Delta x M^{(n+1)}$ has full rank to assert that $P_L^{(n+1)}\boldsymbol{\alpha}^{(n+1)} = \boldsymbol{\phi}_{\pm}^{(n+1)\prime}$. Next we left multiply (E.7) by $P_R^{H(n+1)}$ and take the difference with (E.6) to obtain

$$\left(c^{(0)}I_{++} - \Delta x P_R^{H(n+1)}M^{(n+1)}P_L^{(n+1)}\right)[\boldsymbol{\alpha}_{\pm}^{(n+1)} - \boldsymbol{\alpha}^{(n+1)}] = 0, \tag{E.9}$$

and we use that $c^{(0)}I - \Delta x P_R^{H(n+1)}M^{(n+1)}P_L^{(n+1)}$ has full rank to assert that $\boldsymbol{\alpha}_{\pm}^{(n+1)} = \boldsymbol{\alpha}^{(n+1)}$. Therefore, we conclude for a constant-coefficient system, as well as a constant-coefficient system, that (E.6)and (E.7) are equivalent problems.

Let us now consider the OWNS system that results from discretizing (3.10)

$$c^{(0)}\boldsymbol{\phi}_{\pm}'^{(n+1)} = \Delta x P^{(n+1)}[M^{(n+1)}\boldsymbol{\phi}_{\pm}'^{(n+1)} + \boldsymbol{g}^{(n+1)}] - \sum_{j=1}^{s-1} c^{(j)} P^{(n+1-j)}\boldsymbol{\phi}_{\pm}'^{(n+1-j)}. \tag{E.10}$$

The only difference between system (E.7) and (E.10) are how the projection operator is applied to the derivative term. We left multiply (E.6) by $P_L^{(n+1)}$ and take the difference with (E.10) to obtain

$$\begin{aligned}[c^{(0)}I_{\pm\pm} - \Delta x M^{(n+1)}][P_L^{(n+1)}\boldsymbol{\alpha}^{(n+1)} - \boldsymbol{\phi}_{\pm}^{(n+1)}] \\ + \sum_{j=1}^{s-1} c^{(j)}[P^{(n+1)} - P^{(n+1-j)}]\boldsymbol{\phi}_{\pm}^{(n+1-j)} = 0.\end{aligned} \tag{E.11}$$

We can no longer assert that $\boldsymbol{\alpha}^{(n+1)}$ and $\boldsymbol{\phi}_{\pm}^{(n+1)\prime}$ are equal because of the left-over spatial-marching term. We see that while (E.6)and (E.7) are equivalent systems, the system (E.10) is not. We return now our attention to (E.5). If we discretize using an s-order BDF scheme, then we obtain (E.11), showing that Petrov-Galerkin approach is not generally equivalent to the OWNS approach when the coefficients vary. However, the OWNS approach assumes slowly-varying coefficients so that the Petrov-Galerkin and OWNS approaches should yield similar results.

Appendix F

JACOBIAN OF THE NOWNS EQUATIONS

Here we derive the Jacobian of the fully-discrete system of NOWNS equations (3.20) for 2D disturbances. Note that this analysis readily extends to 3D disturbances. We introduce the 2D residual

$$\hat{\boldsymbol{r}}_m^{\ddagger(k_x+1)} = \sum_{l=0}^{s-1} c^{(l)} A^{\ddagger} \hat{\boldsymbol{\phi}}_m^{\ddagger(k_x+1-l)} - \hat{L}_m^{\ddagger} \hat{\boldsymbol{\phi}}_m^{\ddagger(k_x+1)} - \hat{\boldsymbol{F}}_m^{\ddagger(k_x+1)} - \hat{\boldsymbol{f}}_m^{\ddagger(k_x+1)}, \tag{F.1}$$

for $m \in \mathbb{Z}_M$, which mimics the 3D residual defined in (3.23). We take its derivative with respect to $\hat{\boldsymbol{\phi}}_p^{\ddagger(k_x+1)}$ to obtain

$$\frac{\partial \hat{\boldsymbol{r}}_m^{\ddagger(k_x+1)}}{\partial \hat{\boldsymbol{\phi}}_p^{\ddagger(k_x+1)}} = (c^{(0)} A^{\ddagger} - \hat{L}_m^{\ddagger(k_x+1)}) \delta_{mp} - \frac{\partial \hat{\boldsymbol{F}}_m^{\ddagger(k_x+1)}}{\partial \hat{\boldsymbol{\phi}}_p^{\ddagger(k_x+1)}}, \quad m, p = 0, \ldots, 2M, \tag{F.2}$$

Using the definition DFT, it can be shown (for 2D disturbances) that

$$\frac{\partial \hat{\boldsymbol{F}}_m^{\ddagger(k_x+1)}}{\partial \hat{\boldsymbol{\phi}}_p^{\ddagger(k_x+1)}} = \frac{1}{2M+1} \sum_{l=0}^{2M} \frac{\partial \tilde{\boldsymbol{F}}^{\ddagger(k_x+1)}}{\partial \boldsymbol{\phi}^{\ddagger(k_x+1)}}\Big|_{\boldsymbol{\phi}=\boldsymbol{\phi}_l} e^{i2\pi l \frac{p-m}{2M+1}}, \tag{F.3}$$

which allows us to write

$$\frac{\partial \hat{\boldsymbol{F}}_m^{\ddagger(k_x+1)}}{\partial \hat{\boldsymbol{\phi}}_p^{\ddagger(k_x+1)}} = \begin{bmatrix} 0 & 0 & 0 \\ P_{1,m}^{(k_x+1)} \begin{bmatrix} (\tilde{A}_{\pm\pm}^{(k_x+1)})^{-1} \hat{\boldsymbol{J}}_{\pm\pm,p-m}^{(k_x+1)} \\ \hat{\boldsymbol{J}}_{0\pm,p-m}^{(k_x+1)} \end{bmatrix} & P_{1,m}^{(k_x+1)} \begin{bmatrix} (\tilde{A}_{\pm\pm}^{(k_x+1)})^{-1} \hat{\boldsymbol{J}}_{\pm 0,p-m}^{(k_x+1)} \\ \hat{\boldsymbol{J}}_{00,p-m}^{(k_x+1)} \end{bmatrix} & 0 \\ & & 0 \end{bmatrix}, \tag{F.4}$$

for $m, p = 0, \ldots, 2M$. We define

$$\hat{\boldsymbol{J}}_{p-m}^{\ddagger(k_x+1)} = -\frac{\partial \hat{\boldsymbol{F}}_m^{\ddagger(k_x+1)}}{\partial \hat{\boldsymbol{\phi}}_p^{\ddagger(k_x+1)}} \tag{F.5}$$

for $m, p = 0, \ldots, 2M$ and taking $M = 1$, we obtain the Jacobian $\partial R^{(k+1),\sigma} / \partial \Phi^{(k+1),\sigma}$ shown in (F.6), where σ denotes the index for the Newton iteration, while $R^{(k+1),\sigma}$ and $\Phi^{(k+1),\sigma}$ are the concatenated residual and solution vectors defined in (3.26). Note that we have used $\hat{\boldsymbol{J}}_m^{\ddagger(k_x+1)} = \hat{\boldsymbol{J}}_{m+2M+1}^{\ddagger(k_x+1)}$ and $\hat{\boldsymbol{J}}_m^{\ddagger(k_x+1)} = \overline{\hat{\boldsymbol{J}}_{-m}^{\ddagger(k_x+1)}}$ for $m = 0, \ldots, M$.

$$\frac{\partial R^{(k+1),\sigma}}{\partial \Phi^{(k+1),\sigma}} = \begin{bmatrix} (c^{(0)}A^{\ddagger} - \hat{L}_0^{\ddagger(k_x+1)}) + \hat{J}_0^{\ddagger(k_x+1),\sigma} & \overline{\hat{J}_1^{\ddagger(k_x+1),\sigma}} & \hat{J}_1^{\ddagger(k_x+1),\sigma} \\ \hat{J}_1^{\ddagger(k_x+1),\sigma} & (c^{(0)}A^{\ddagger} - \hat{L}_1^{\ddagger(k_x+1)}) + \hat{J}_0^{\ddagger(k_x+1),\sigma} & \overline{\hat{J}_1^{\ddagger(k_x+1),\sigma}} \\ \overline{\hat{J}_1^{\ddagger(k_x+1),\sigma}} & \hat{J}_1^{\ddagger(k_x+1),\sigma} & (c^{(0)}A^{\ddagger} - \hat{L}_{-1}^{\ddagger(k_x+1)}) + \hat{J}_0^{\ddagger(k_x+1),\sigma} \end{bmatrix} \tag{F.6}$$

Appendix G

DESIGN CHOICES FOR NOWNS

G.1 Streamwise diffusion terms

Here we demonstrate for the 2D validation case discussed in Section 3.3.1 that although streamwise diffusion effects have a minimal impact on the linear calculation (Figure G.1a), the impact is more pronounced in the nonlinear case (Figure G.1b). We see that prior to the second neutral stability point, the calculations with and without the streamwise diffusion terms yield similar amplitudes, but that downstream of this point, the amplitudes of the calculation including the streamwise viscous terms has much lower amplitudes (particularly for the higher harmonics in the nonlinear case).

G.2 Inclusion of the streamwise pressure gradient

Unlike the NPSE approach, the NOWNS approach has no minimum step size requirement for the march to be numerically stable, but it is still necessary to neglect the streamwise pressure gradient for the zero-frequency modes. If the streamwise pressure gradient for these modes is retained, the NOWNS march remains stable but becomes inaccurate, as demonstrated in Figure G.2. We plot the u-velocity amplitudes with and without $\partial_x p_0$ in Figure G.2a, where we see that we have reasonable agreement for $m \neq 0$, but disagreement for $m = 0$. In Figure G.2b we plot the profile of the v_0, and we notice that the profile predicted by NOWNS when $\partial_x p_0$ is included is substantially different from the profiles predicted by NPSE and DNS.

If we neglect $\partial_x p_0$, but include the streamwise diffusion terms $\partial_{xx} q_0$, then we must project the MFD and we find that we have good agreement between the DNS and NOWNS calculations. Therefore, we can conclude that the recursion parameters we are using for the zero-frequency modes are valid. However, as discussed above, the calculation remains stable but becomes inaccurate when we include $\partial_x p_0$. Although our march remains stable, there including $\partial_x p_0$ leads to inaccuracies in the march for unknown reasons.

In Figure G.3a, we plot the u-velocity amplitudes computed by NOWNS with and without the pressure gradient for the zero-frequency modes. Mode (1,0) is tracked reasonably accurately, but the other modes are not. In particularly, the (1,2),

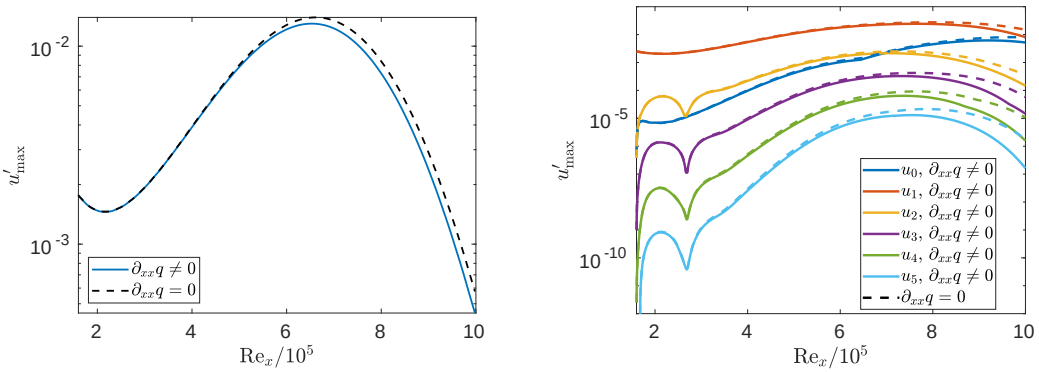

(a) Linear calculation (b) Nonlinear calculation

Figure G.1: u-velocity amplitudes with and without streamwise diffusion terms for the 2D evolution of the TS wave.

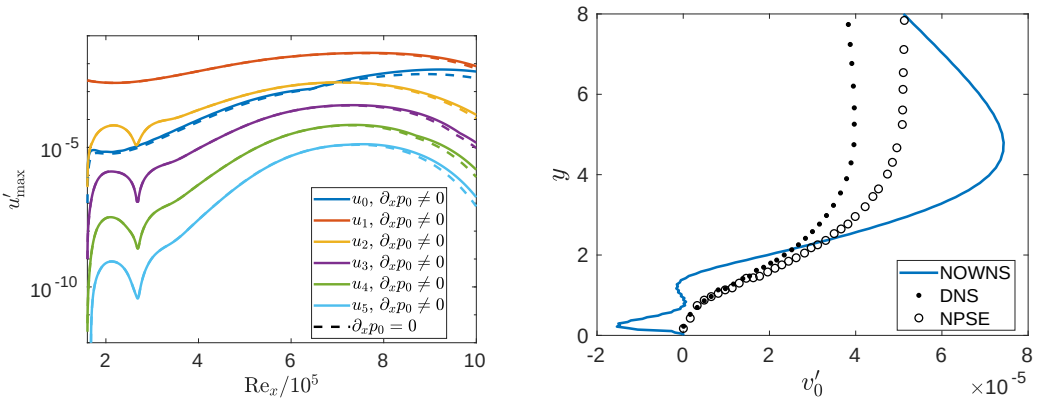

(a) u-velocity amplitudes (b) v-velocity profile

Figure G.2: 2D validation case with and without streamwise pressure gradient for zero-frequency modes.

(1,1), and (0,1) modes and the MFD have higher amplitudes than they should. In Figure G.3b, we see that we have better qualitative agreement in the early stages of the march between the NOWNNS and DNS calculations when the streamwise pressure gradient terms are include for the zero-frequency modes. However, we have worse quantitative agreement in the later stages of the march, which in turn causes the larger amplitudes of the (1,2), (1,1) and (0,1) modes observed in Figure G.3a.

G.3 Comparison of nonlinear solution procedures

We have discussed three procedures for solving the nonlinear system of equations: (i) Newton's method, (ii) a quasi-Newton method that includes part of the nonlinear Jacobian, and (iii) a quasi-Newton method that excludes the Jacobian of the nonlinear

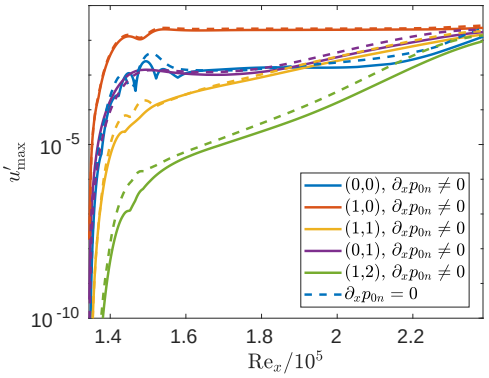

(a) u-velocity amplitudes

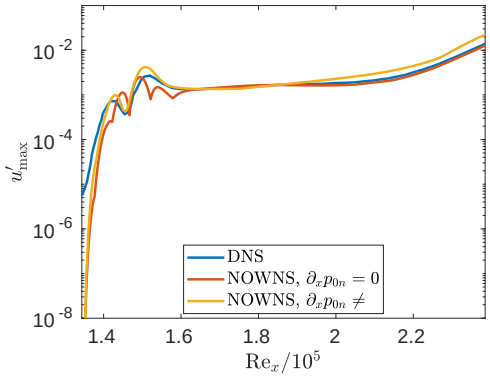

(b) u-velocity amplitudes for MFD

Figure G.3: K-type transition case with and without streamwise pressure gradient for zero-frequency modes.

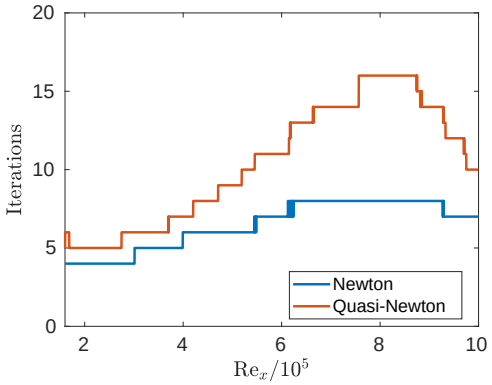

(a) Comparison of Newton's method and the quasi-Newton method for the 2D validation case

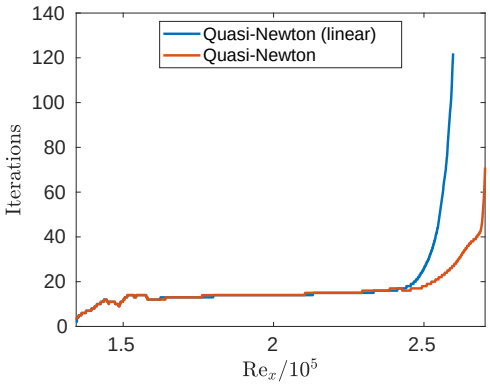

(b) Comparison of the linear and nonlinear quasi-Newton methods for K-type transition

Figure G.4: Comparison of solution procedures for the nonlinear system of equations.

term. We plot the iterations to converge as a function of streamwise station in Figure G.4. For the 2D validation case, we compare the iterations to convergence for the quasi-Newton method and Newton's method in Figure G.4a, which shows that Newton's method converges in fewer iterations. In Figure G.4b, we make the same comparison for linear and nonlinear quasi-Newton methods for K-type transition. We see that farther downstream, where the nonlinearity is stronger, the nonlinear quasi-Newton method converges in fewer iterations than the linear version. However, for sufficiently strong nonlinearities, it is necessary to use Newton's method.

G.4 Linearization about the baseflow vs. the corrected mean flow

Whereas in linear stability analysis, the mean flow is determined only by the baseflow, $\bar{\boldsymbol{q}}$, in the nonlinear case the disturbances interact to excite the MFD, $\boldsymbol{q}'_{00}$, which yields the corrected mean flow, $\bar{\boldsymbol{q}}+\boldsymbol{q}'_{00}$. In linear OWNS, we linearize the projection operators about the baseflow, while in nonlinear OWNS, we can choose to instead linearize about the corrected mean flow.

G.4.1 Equations linearized about the corrected mean flow

Consider nonlinear equations of the form

$$\mathcal{N}(\boldsymbol{q}) = 0. \tag{G.1}$$

To linearize about the base flow, we take $\boldsymbol{q} = \bar{\boldsymbol{q}} + \boldsymbol{q}'$ and assume that the base flow satisfies the governing equations, so that $\mathcal{N}(\bar{\boldsymbol{q}}) = 0$ and

$$\mathcal{N}(\bar{\boldsymbol{q}} + \boldsymbol{q}') = \mathcal{N}(\bar{\boldsymbol{q}}) + L(\bar{\boldsymbol{q}})\boldsymbol{q}' + F(\bar{\boldsymbol{q}}, \boldsymbol{q}') = L(\bar{\boldsymbol{q}})\boldsymbol{q}' + \boldsymbol{F}(\bar{\boldsymbol{q}}, \boldsymbol{q}'),$$

where $L(\bar{\boldsymbol{q}})\boldsymbol{q}'$ and $\boldsymbol{F}(\bar{\boldsymbol{q}}, \boldsymbol{q}')$ are the linear and nonlinear terms, respectively. This yields

$$L(\bar{\boldsymbol{q}})\boldsymbol{q}' + \boldsymbol{F}(\bar{\boldsymbol{q}}, \boldsymbol{q}') = 0. \tag{G.2}$$

If we linearize about the corrected mean flow, then we define $\tilde{\boldsymbol{q}}' = \boldsymbol{q}' - \hat{\boldsymbol{q}}_{00}$ so that

$$\begin{aligned}\mathcal{N}(\bar{\boldsymbol{q}} + \hat{\boldsymbol{q}}_{00} + \tilde{\boldsymbol{q}}') &= \mathcal{N}(\bar{\boldsymbol{q}} + \hat{\boldsymbol{q}}_{00}) + L(\bar{\boldsymbol{q}} + \hat{\boldsymbol{q}}_{00})\tilde{\boldsymbol{q}}' + \boldsymbol{F}(\bar{\boldsymbol{q}} + \hat{\boldsymbol{q}}_{00}, \tilde{\boldsymbol{q}}') \\ &= \mathcal{N}(\bar{\boldsymbol{q}}) + L(\bar{\boldsymbol{q}})\hat{\boldsymbol{q}}_{00} + \boldsymbol{F}(\bar{\boldsymbol{q}}, \hat{\boldsymbol{q}}_{00}) + L(\bar{\boldsymbol{q}} + \hat{\boldsymbol{q}}_{00})\tilde{\boldsymbol{q}}' + \boldsymbol{F}(\bar{\boldsymbol{q}} + \hat{\boldsymbol{q}}_{00}, \tilde{\boldsymbol{q}}'),\end{aligned}$$

yielding

$$L(\bar{\boldsymbol{q}})\hat{\boldsymbol{q}}_{00} + \boldsymbol{F}(\bar{\boldsymbol{q}}, \hat{\boldsymbol{q}}_{00}) + L(\bar{\boldsymbol{q}} + \hat{\boldsymbol{q}}_{00})\tilde{\boldsymbol{q}}' + \boldsymbol{F}(\bar{\boldsymbol{q}} + \hat{\boldsymbol{q}}_{00}, \tilde{\boldsymbol{q}}') = 0. \tag{G.3}$$

In the current form, we must update the LU decomposition after each Newton iteration, so we decrease the computational cost by linearizing about a fixed corrected mean flow. We take the MFD from the previous streamwise station and label it $\boldsymbol{q}_c$. Then we take $\tilde{\boldsymbol{q}}' = \boldsymbol{q}' - \boldsymbol{q}_c$ to obtain

$$L(\bar{\boldsymbol{q}})\boldsymbol{q}_c + \boldsymbol{F}(\bar{\boldsymbol{q}}, \boldsymbol{q}_c) + L(\bar{\boldsymbol{q}} + \boldsymbol{q}_c)\tilde{\boldsymbol{q}}' + \boldsymbol{F}(\bar{\boldsymbol{q}} + \boldsymbol{q}_c, \tilde{\boldsymbol{q}}') = 0. \tag{G.4}$$

If $\boldsymbol{q}_c = \hat{\boldsymbol{q}}_{00}$, then we recover (G.3).

We consider three approaches:

1. Solve (G.3) by updating $\hat{\boldsymbol{q}}_{00}$ after each Newton iteration, or

2. Take $\boldsymbol{q}_c$ equal to the MFD from the previous station and then solve (G.4). Update $\boldsymbol{q}_c$ by taking $\boldsymbol{q}_c = \tilde{q}_{00} + \boldsymbol{q}_c$ each time the Newton solver converges. We say that the solver has converged when $\|\tilde{\boldsymbol{q}}_{00}\|$ is sufficiently small.

3. Take $\boldsymbol{q}_c$ equal to the MFD from the previous station and then solve (G.4). Do not update $\boldsymbol{q}_c$ unless $A(\bar{\boldsymbol{q}} + \boldsymbol{q}_c)$ and $A(\bar{\boldsymbol{q}} + \boldsymbol{q}_c + \tilde{\boldsymbol{q}}_{00})$ have characteristics with different signs.

For the sake of computational efficiency, we take the third approach. This ensures that the signs of our characteristics are consistent with those of the corrected mean flow, without an increase in computational cost relative to linearizing about the base flow.

G.4.1.1 Results for K-type transition

For the K-type transition case of Section 3.4.4, we perform the NOWNS calculation again, but we instead linearize about the corrected mean flow. In Figure G.5, we compare the amplitudes computed by the two approaches to NOWNS and we see that in the early stages of the march, when the amplitudes are small, the two calculations are nearly identical, but that they begin to differ slightly as the disturbance amplitudes increase. The differences are small, but are most notable for the MFD, $\boldsymbol{q}'_{00}$, and the vortex mode, q'_{01}, after $\mathrm{Re}_x = 2.5 \times 10^5$, which corresponds to an MFD amplitude of roughly 3% of U_∞. The two NOWNS marches continue to yield similar results until the end of the calculation at $\mathrm{Re}_x = 2.74 \times 10^5$, where the MFD amplitude is 11% of U_∞. Since linearizing about the corrected mean flow has a negligible impact on the solution, we recommend linearizing about the base flow for the sake of simplicity.

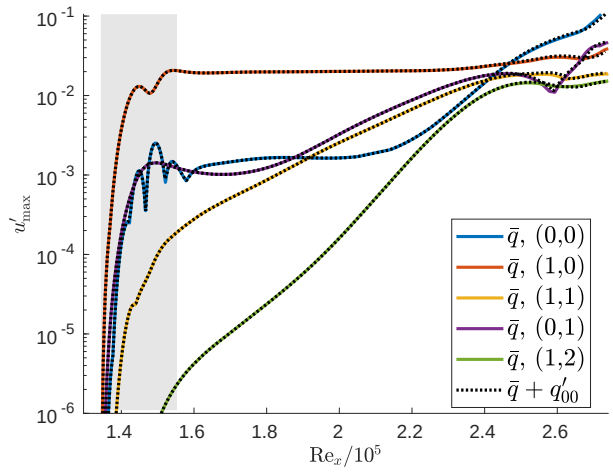

Figure G.5: Amplitude of u' v.s. streamwise coordinate, Re_x, for fundamental breakdown. Compare linearizing NOWNS about $\bar{\boldsymbol{q}}$ vs. $\bar{\boldsymbol{q}} + \boldsymbol{q}'_{00}$.

Appendix H

HEURISTIC RECURSION PARAMETER SETS

This thesis requires recursion parameter sets for the following low- and high-speed boundary-layer flows. We use the heuristic recursion parameters for high-speed boundary-layer flows from Kamal (2023), and the heuristic recursion parameters for low-speed boundary-layer flows from Rigas et al. (2017a), which we present below.

H.1 Recursion parameters for non-zero frequencies

The recursion parameters are chosen based on the eigenvalues of the Euler equations linearized about a uniform flow, as described in Towne and Colonius (2015). The eigenvalues are

$$i\alpha_c = \frac{ik}{\bar{M}_x}, \quad i\alpha_{a_1}(z) = ik\frac{-\bar{M}_x + \mu(z)}{1-\bar{M}_x^2}, \quad i\alpha_{a_2}(z) = ik\frac{-\bar{M}_x - \mu(z)}{1-\bar{M}_x^2},$$

where $\bar{M}_x = \bar{u}/\bar{c}$ is the local streamwise Mach number, $k = \omega/\bar{c}$ is the streamwise wave number, z is a composite wave-number (for the transverse directions), and the function $\mu(z)$ is given by

$$\mu(z) = \sqrt{1-(1-\bar{M}_x^2)z^2}.$$

For subsonic boundary layer flows, we use the same recursion parameters as in (Rigas et al., 2017a), which differ slightly from those developed originally in (Towne and Colonius, 2015), so we will briefly explain the new choice of recursion parameters.

The present choice of recursion parameters are separated into the following groups: (i) vortical modes, which replace convective modes, (ii) fast and slow stream evanescent acoustic modes, and (iii) fast and slow stream propagating acoustic modes, where fast stream modes are associated with the free-stream streamwise Mach number, while slow stream modes are associated with a small Mach number (inside the boundary layer). The recursion parameters for the vortical modes of the present study match closely the parameters for convective modes in (Towne and Colonius, 2015), while the recursion parameters for the propagating acoustic modes are distributed the same way in both the present study and in (Towne and Colonius, 2015). The parameters for the evanescent acoustic modes are distributed in a slightly different way, so we focus our discussion on these parameters.

To distribute the parameters for the evanescent acoustic modes, we define

$$\eta_c = \frac{k}{1 - \bar{M}_x}, \quad \eta_m = 1.5\frac{L_y}{\Delta y},$$

where L_y is the (dimensionless) extent of the domain in the wall-normal direction, while Δy is the (uniform) wall-normal grid-spacing. These define the spacing parameter

$$\eta^{(h)} = \eta_m + \frac{h}{N_e - 1}\left(\eta_c + 0.1\frac{\eta_m - \eta_c}{N_e - 1} - \eta_m\right), \quad h = 0, \ldots, N_e - 1,$$

which in turn defines

$$\mu^{(h)} = \mu(\eta^{(h)}), \quad h = 0, \ldots, N_e - 1.$$

This contrasts with the choice

$$\mu^{(h)} = \mu_{\max}\frac{h}{2N_e}, \quad h = 0, \ldots, 2N_e - 1,$$

used in Towne and Colonius (2015), where $\mu_{\max} = \mu(z_{\max})$. Here, $z_{\max}$ represents the maximum transverse wave number supported by the semi-discrete Euler equations (wave numbers larger than $z_{\max}$ need not be considered because they are not supported by the semi-discrete equations). The present approach considers a range of z near $z_{\max}$ (distributed according to $\eta^{(h)}$) which is then used to define $\mu^{(h)}$, while the approach presented in Towne and Colonius (2015) considers only one z to get $\mu_{\max}$, which is then used to define $\mu^{(h)}$ spaced linearly over $[0, \mu_{\max}]$. The present approach is advantageous because $\mu(z)$ is nonlinear in z.

The recursion parameter sets for a subsonic boundary layer flow are summarized in Table H.1. The fast-stream values are denoted k_1 and $\bar{M}_{x,1}$, while the slow-stream values are denoted k_2 and $\bar{M}_{x,2}$. The acoustic modes must be computed for both the fast- and slow-stream values.

H.2 Zero-frequency modes

The recursion parameter sets for non-zero frequency modes match those used in Sleeman et al. (2024b). They depend on ω through the streamwise wave number $k = \omega/\bar{c}$, and when $k = 0$, the recursion parameters associated with the vortical and propagating acoustic waves go to zero, leaving only the evanscent acoustic waves, as shown in Table H.2.

Type	Spacing	$\beta_+^{(j)}$	$\beta_-^{(j)}$
Vortical	$b^{(h)} = \frac{k_1}{\bar{M}_{x,1}} + \frac{h}{N_\omega}\left(\frac{k_2}{\bar{M}_{x,2}} - \frac{k_1}{\bar{M}_{x,1}}\right)$ $h = 0, \ldots, N_\omega - 1$	$(1+i)b^{(j)}$	$\frac{-2k_2\bar{M}_2}{1-\bar{M}_2^2} - b^{(j)}$
Evanescent acoustic	$\mu^{(h)} = \sqrt{k^2 - (1-\bar{M}_x^2)(\eta^{(h)})^2}$ $h = 0, \ldots, N_e - 1$	$\frac{-\bar{M}_x k + \mu^{(j)}}{1-\bar{M}_x^2}$	$\frac{-\bar{M}_x k - \mu^{(j)}}{1-\bar{M}_x^2}$
Propagating acoustic	$\theta^{(h)} = \frac{h}{N_p}\pi/2$ $h = 0, \ldots, 2N_p - 1$	$k\frac{-\bar{M}_x + \cos\theta^{(2j)}}{1-\bar{M}_x^2}$	$k\frac{-\bar{M}_x - \cos\theta^{(2j+1)}}{1-\bar{M}_x^2}$

Table H.1: Recursion parameter sets for subsonic boundary layer flows.

Type	Spacing	$\beta_+^{(j)}$	$\beta_-^{(j)}$
Evanescent acoustic	$\mu^{(h)} = \sqrt{-(1-\bar{M}_x^2)(\eta^{(h)})^2}$ $h = 0, \ldots, N_e - 1$	$\frac{\mu^{(j)}}{1-\bar{M}_x^2}$	$\frac{-\mu^{(j)}}{1-\bar{M}_x^2}$

Table H.2: Recursion parameter sets for subsonic boundary layer flows for zero-frequency modes.

Appendix I

LABELING EIGENVALUES ACCORDING TO BRIGGS' CRITERION

To evaluate $\mathcal{J}(\cdot)$ and $\mathcal{J}^{(R)}(\cdot)$, we must know whether an eigenvalue is upstream- or downstream-going, which we can do using Briggs' criterion (see definition 2.2.3). By proposition 2.2.4, $M(s)$ has N_+ downstream- and N_- upstream-going eigenvalues so that taking $\eta \to \infty$ yields N_+ eigenvalues with $\mathcal{I}(\alpha) > 0$ and N_- eigenvalues with $\mathcal{I}(\alpha) < 0$. In principle, we can choose a large value of η such that there N_+ eigenvalues with $\mathcal{I}(\alpha) > 0$ and N_- eigenvalues with $\mathcal{I}(\alpha) < 0$, and then slowly decrease η to zero while tracking the eigenvalues (since they are a continuous function of η) to assign a label of upstream- or downstream-going. However, for problems of interest, the sign of $\mathcal{I}(\alpha)$ remains the same for most eigenvalues as η increases, as shown in Figure I.1a. For this configuration, the sign of $\mathcal{I}(\alpha)$ changes for only one eigenvalue, as shown in Figure I.1b. Since the sign of $\mathcal{I}(\alpha)$ does not change as η increases for most eigenvalues, we choose the smallest $\eta > 0$ such that there N_+ eigenvalues with $\mathcal{I}(\alpha) > 0$ and call it η_{opt} (see algorithm 3). Then we match each eigenvalue associated with η_{opt} to the closest eigenvalue associated with $\eta = 0$, where we measure distance as $|\alpha(\eta_{\text{opt}} - i\omega) - \alpha(-i\omega)|$ (see algorithm 4). There is no guarantee that this algorithm will always correctly label the eigenvalues, but we have found this to work well in-practice. Moreover, if an eigenvalue is labeled incorrectly, then the OWNS march will not be well-posed and will fail. Therefore, any failure in labeling the eigenvalues will be easy to identify.

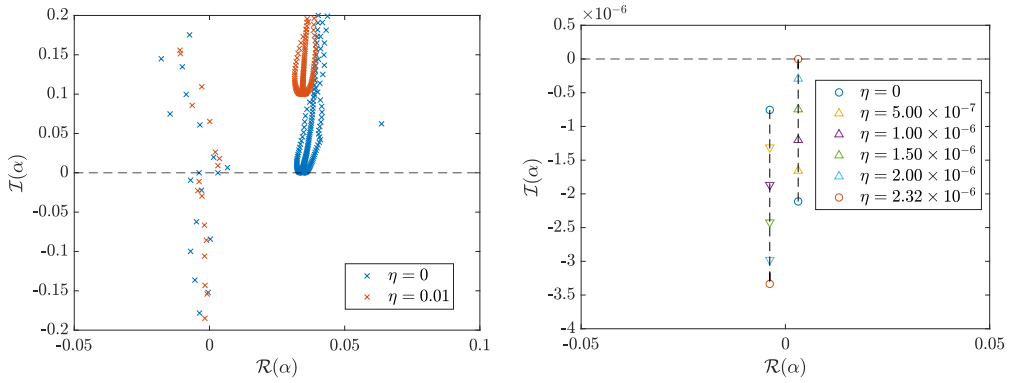

(a) (b)

Figure I.1: Spectrum of TS wave at $\mathrm{Re}_x = 1.6 \times 10^5$ for different values of η.

Algorithm 3 Bisection search for smallest η such that there are N_+ eigenvalues with $\mathcal{I}(\alpha) > 0$ and N_- eigenvalues with $\mathcal{I}(\alpha) < 0$

Input: (real) frequency ω
$\eta_{\max} \leftarrow 1$, $\eta_{\min} \leftarrow 0$
while $\eta_{\max} - \eta_{\min} > \eta_{\max} \times 10^{-3}$ **do**
  $\eta \leftarrow (\eta_{\min} + \eta_{\max})/2$
  $\boldsymbol{\alpha} \leftarrow$ eigenvalues of $M(\eta - i\omega)$
  $\tilde{N}_+ \leftarrow$ number of α such that $\mathcal{I}(\alpha_i) > 0$ for $i = 1, \ldots, N$
  $\tilde{N}_- \leftarrow$ number of α such that $\mathcal{I}(\alpha_i) < 0$ for $i = 1, \ldots, N$
  if $\tilde{N}_+ = N_+$ and $\tilde{N}_- = N_-$ **then**
    $\eta_{\max} \leftarrow \eta$
  else
    $\eta_{\min} \leftarrow \eta$
  end if
end while
$\mathrm{eta}_{\mathrm{opt}} \leftarrow \eta$
return η_{opt}

Algorithm 4 Apply Briggs' criterion to label eigenvalues

Given a (real) frequency ω, compute η_{opt} using algorithm 3
$\boldsymbol{\alpha}_{\text{opt}} \leftarrow$ eigenvalues of $M(\eta_{\text{opt}} - i\omega)$
$\boldsymbol{\alpha}_{\text{zero}} \leftarrow$ eigenvalues of $M(-i\omega)$
$\tilde{N}_{+}^{\text{zero}} \leftarrow$ number of α_{zero} such that $\mathcal{I}(\alpha_{\text{zero},i}) > 0$ for $i = 1, \ldots, N$
$\tilde{N}_{-}^{\text{zero}} \leftarrow$ number of α_{zero} such that $\mathcal{I}(\alpha_{\text{zero},i}) < 0$ for $i = 1, \ldots, N$
$\tilde{N}_{+}^{\text{opt}} \leftarrow$ number of α_{opt} such that $\mathcal{I}(\alpha_{\text{opt},i}) > 0$ for $i = 1, \ldots, N$
$\tilde{N}_{-}^{\text{opt}} \leftarrow$ number of α_{opt} such that $\mathcal{I}(\alpha_{\text{opt},i}) < 0$ for $i = 1, \ldots, N$
$N_{\text{flip}} \leftarrow |\tilde{N}_{+}^{\text{zero}} - \tilde{N}_{+}^{\text{opt}}|$
$N_{\text{count}} \leftarrow 0$, $i \leftarrow 0$, $\boldsymbol{\alpha}_{+} \leftarrow \{\}$, $\boldsymbol{\alpha}_{-} \leftarrow \{\}$
while $N_{\text{count}} < N_{\text{flip}}$ **do**
    $i \leftarrow i + 1$
    $j \leftarrow \arg\min_{j=1,\ldots,N} |\alpha_{\text{zero},i} - \alpha_{\text{opt},j}|$.
    if $\text{sign}(\mathcal{I}(\alpha_{\text{zero},i})) \neq \text{sign}(\mathcal{I}(\alpha_{\text{opt},j}))$ **then**
        $N_{\text{count}} \leftarrow N_{\text{count}} + 1$
        if $\text{sign}(\mathcal{I}(\alpha_{\text{zero},i})) > 0$ **then**
            $\boldsymbol{\alpha}_{-} \leftarrow$ append $\alpha_{\text{zero},i}$
        else
            $\boldsymbol{\alpha}_{+} \leftarrow$ append $\alpha_{\text{zero},i}$
        end if
    else
        if $\text{sign}(\mathcal{I}(\alpha_{\text{zero},i})) > 0$ **then**
            $\boldsymbol{\alpha}_{+} \leftarrow$ append $\alpha_{\text{zero},i}$
        else
            $\boldsymbol{\alpha}_{-} \leftarrow$ append $\alpha_{\text{zero},i}$
        end if
    end if
end while

Appendix J

TRANSIENT GROWTH IN LOW-SPEED BOUNDARY-LAYER FLOWS

OWNS can be used to find optimal (worst-case) disturbances, as done by Rigas et al. (2017b) and Towne et al. (2022). We also note that Monokrousos et al. (2010) have investigated optimal disturbances for 3D low-speed boundary-layer flows using time-stepping methods, while Tempelmann et al. (2010) have used PSE to investigate optimal disturbances for incompressible boundary-layer flows, and Tempelmann et al. (2012) did the same for compressible boundary-layer flows. We follow the procedure introduced by Rigas et al. (2017b), adapted to a low-speed boundary-layer flow, where we use the kinetic energy

$$\|\boldsymbol{q}\|_K^2 = \boldsymbol{q}^H W K \boldsymbol{q} \approx \int_0^y [\bar{\rho} u'^2 + \bar{\rho} v'^2 + \bar{\rho} w'^2] dy, \tag{J.1}$$

to measure the size of our disturbances. Then we can seek, for example, the inlet boundary condition that leads to the largest kinetic energy at the domain outlet:

$$\mathcal{J}(\boldsymbol{q}_{\text{in}}, \mathrm{q}_{\text{out}}) \equiv \frac{\|\boldsymbol{q}_{\text{out}}\|_K^2}{\|\boldsymbol{q}_{\text{in}}\|_K^2}. \tag{J.2}$$

We introduce the inner product

$$\langle \boldsymbol{\psi}_\pm, \boldsymbol{\phi}_\pm \rangle = \int_x \boldsymbol{\psi}_\pm^H W \boldsymbol{\phi}_\pm dx \approx \int_x \int_y \boldsymbol{\psi}_\pm^H \boldsymbol{\phi}_\pm dy dx, \tag{J.3}$$

and note that our solution must satisfy the forward problem

$$\frac{\partial \boldsymbol{\phi}_\pm}{\partial x} = PM\boldsymbol{\phi}_\pm, \quad T^{-1}\boldsymbol{\phi}_\pm(x_{\text{in}}) = \boldsymbol{q}_{\text{in}}, \tag{J.4}$$

which allows us to introduce the Lagrangian

$$\mathcal{L}(\boldsymbol{\phi}_{\pm,\text{in}}, \boldsymbol{\phi}_{\pm,\text{out}}, \boldsymbol{\phi}_\pm, \boldsymbol{\psi}_\pm) = \mathcal{J}(T^{-1}\boldsymbol{\phi}_{\pm,\text{in}}, T^{-1}\boldsymbol{\phi}_{\pm,\text{out}}) - \langle \boldsymbol{\psi}_\pm, \frac{\partial \boldsymbol{\phi}_\pm}{\partial x} - PM\boldsymbol{\phi}_\pm \rangle. \tag{J.5}$$

Integration-by-parts yields

$$\begin{aligned}\langle \boldsymbol{\psi}_\pm, \frac{\partial \boldsymbol{\phi}_\pm}{\partial x} - PM\boldsymbol{\phi}_\pm \rangle &= \int_x \boldsymbol{\psi}_\pm^H W \frac{\partial \boldsymbol{\phi}_\pm}{\partial x} dx - \int_x \boldsymbol{\psi}_\pm^H WPM\boldsymbol{\phi}_\pm dx \\ &= -\int_x \frac{\boldsymbol{\psi}_\pm^H}{\partial x} W\boldsymbol{\phi}_\pm dx - \int_x (M^H P^H \boldsymbol{\psi}_\pm)^H W\boldsymbol{\phi}_\pm dx \\ &+ \boldsymbol{\psi}_{\pm,\text{out}}^H W\boldsymbol{\phi}_{\pm,\text{out}} - \boldsymbol{\psi}_{\pm,\text{in}}^H W\boldsymbol{\phi}_{\pm,\text{in}} \\ &= -\langle \frac{\partial \boldsymbol{\psi}_\pm}{\partial x} + M^H P^H \boldsymbol{\psi}_\pm, \boldsymbol{\phi}_\pm \rangle + \boldsymbol{\psi}_{\pm,\text{out}}^H W\boldsymbol{\phi}_{\pm,\text{out}} - \boldsymbol{\psi}_{\pm,\text{in}}^H W\boldsymbol{\phi}_{\pm,\text{in}},\end{aligned}$$

so that

$$\begin{aligned}\mathcal{L}(\boldsymbol{\phi}_{\pm,\text{in}}, \boldsymbol{\phi}_{\pm,\text{out}}, \boldsymbol{\phi}_\pm, \boldsymbol{\psi}_\pm) = \mathcal{J}(T^{-1}\boldsymbol{\phi}_{\pm,\text{in}}, T^{-1}\boldsymbol{\phi}_{\pm,\text{out}}) + \langle \frac{\partial \boldsymbol{\psi}_\pm}{\partial x} + M^H P^H \boldsymbol{\psi}_\pm, \boldsymbol{\phi}_\pm \rangle \\ - \boldsymbol{\psi}_{\pm,\text{out}}^H W\boldsymbol{\phi}_{\pm,\text{out}} + \boldsymbol{\psi}_{\pm,\text{in}}^H W\boldsymbol{\phi}_{\pm,\text{in}}.\end{aligned}$$

Variations with respect to each variable must be zero, yielding the following constraints:

$$\langle \nabla_{\boldsymbol{\psi}}, \delta\boldsymbol{\phi} \rangle = 0 \Rightarrow \frac{\partial \boldsymbol{\phi}_\pm}{\partial x} - PM\boldsymbol{\phi}_\pm = 0, \tag{J.6a}$$

$$\langle \nabla_{\boldsymbol{\phi}}, \delta\boldsymbol{\psi} \rangle = 0 \Rightarrow \frac{\partial \boldsymbol{\phi}_\pm}{\partial x} + M^H P^H \boldsymbol{\phi}_\pm = 0, \tag{J.6b}$$

$$\langle \nabla_{\boldsymbol{\phi}_{\text{out}}}, \delta\boldsymbol{\phi}_{\text{out}} \rangle = 0 \Rightarrow \boldsymbol{\psi}_{\pm,\text{out}} = T^{-H} WKT^{-1} \boldsymbol{\phi}_{\pm,\text{out}} \tag{J.6c}$$

$$\langle \nabla_{\boldsymbol{\phi}_{\text{in}}}, \delta\boldsymbol{\phi}_{\text{in}} \rangle = 0 \Rightarrow \boldsymbol{\phi}_{\pm,\text{in}} = (T^{-H} WKT^{-1})^{-1} \boldsymbol{\psi}_{\pm,\text{in}}. \tag{J.6d}$$

The solution procedure is summarized as follows:

1. Solve the direct equation (J.6a).
2. Solve for the adjoint outlet boundary condition (J.6c), rescaled to unit norm.
3. Solve the adjoint equation (J.6b).
4. Solve for the inlet boundary condition (J.6d), rescaled to unit norm.

J.1 Preliminary results

The Tollmien-Schlichting (TS) wave is the only unstable mode in low-speed boundary-layer flows. Therefore, it is the optimal modal inlet boundary condition. Moreover, given a sufficiently long streamwise distance over which the TS wave is unstable, we expect any other disturbance to eventually turn into a TS wave, since any components that are colinear with the TS wave will be amplified. However, since the linearized Navier-Stokes operator is non-normal, there should exist an inlet boundary condition

that causes non-modal (transient) growth, which leads to more growth than the TS wave on its own.

We verify that our results agree with expectation for 2D disturbances to the Blasius profile at $Ma = 0.1$ with disturbance frequency $F = 50 \times 10^{-6}$. The TS wave is unstable over $Re_x \in [3.75 \times 10^5, 1.43 \times 10^5]$, and so we seek the optimal inlet boundary condition over this streamwise domain with $y \in [0, 150]$, $N_x = 6000$ and $N_y = 200$. Figure J.1 plots the norms associated with the optimal, random, and TS wave boundary conditions, showing that the optimal solution experiences transient growth, before turning into a TS wave and evolving like a TS wave. Similarly, the random inlet boundary condition also turns into a TS wave, but more slowly than the optimal. To assess how similar a disturbance is to a TS wave, we measure it using the inner product

$$\text{TS Score of } \boldsymbol{q} \equiv \frac{\boldsymbol{q}^{\boldsymbol{H}} W \boldsymbol{q}_{\text{TS}}}{\|\boldsymbol{q}\|_K \|\boldsymbol{q}_{\text{TS}}\|_K}, \tag{J.7}$$

which is zero if $\boldsymbol{q}$ is orthogonal to the TS wave, and 1 if it is the TS wave. We see that the optimal inlet boundary condition becomes a TS wave much more quickly than the random inlet boundary condition. Figure J.2 compares the optimal inlet boundary condition to the TS wave. We see that the optimal inlet condition has a large amplitude u-velocity disturbance near the surface of the plate, while both the u- v-velocity disturbances are smaller farther from the wall. We repeat this analysis for a range of frequencies, and plot the gain as a function of F in Figure J.3, where we see that both the optimal and TS gains decrease with increasing F at roughly the same rate. Figure J.4 plots $G_{\text{optim}} - G_{\text{TS}}$ and shows that the transient growth decreases with increasing F.

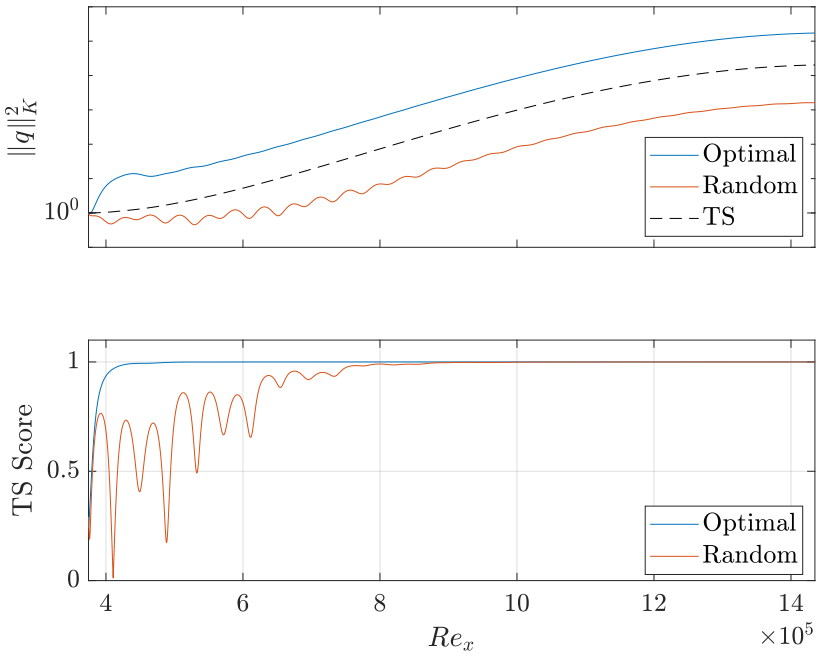

Figure J.1: Norm of optimal inlet boundary condition, compared to random and TS wave inlet boundary conditions for $F = 50 \times 10^{-6}$, between branches I and II.

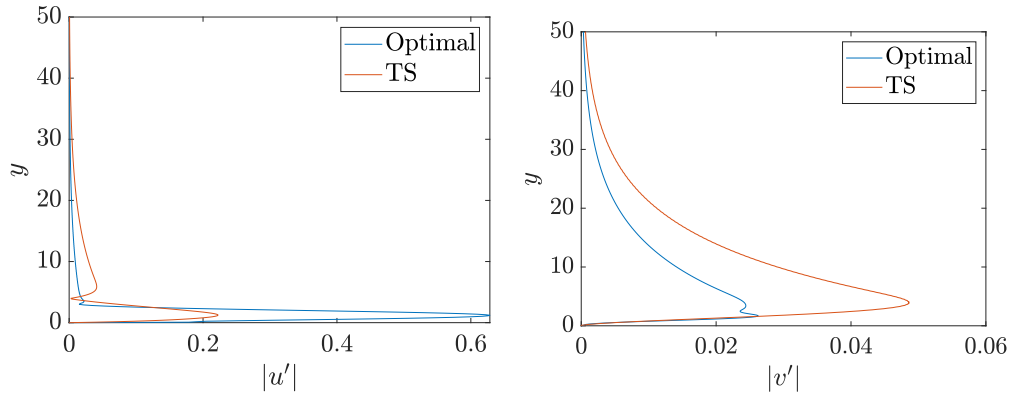

Figure J.2: Optimal inlet boundary condition for $F = 50 \times 10^{-6}$, compared to TS wave.

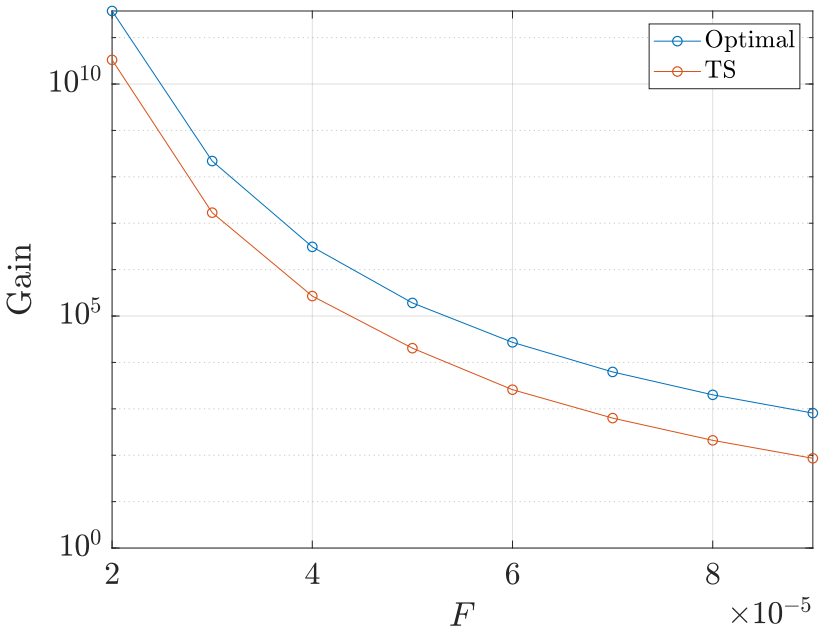

Figure J.3: Optimal vs. TS gain for a range of frequencies.

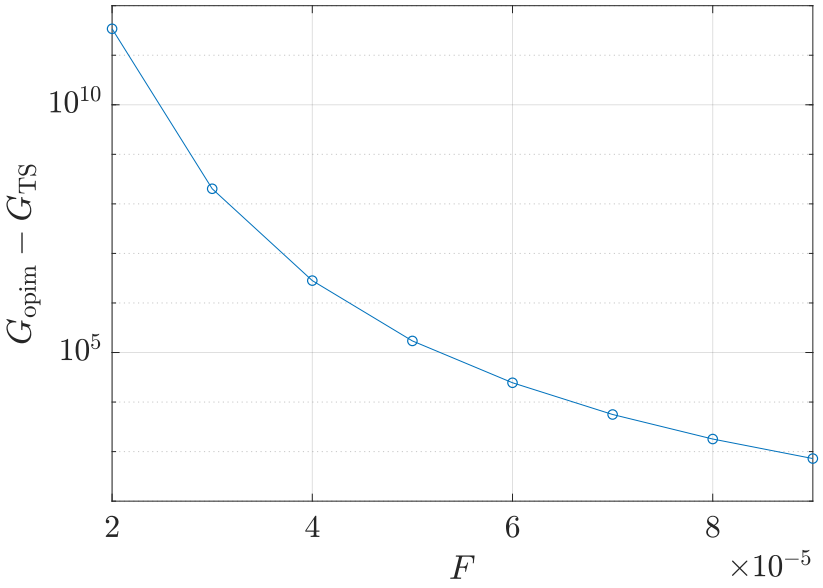

Figure J.4: Difference in optimal and TS gains for a range of frequencies.